University of Oslo

High-spatial-resolution electron density measurements using needle Langmuir probe system on different space platforms

by

Huy M. Hoang

Dissertation for the degree of

Philosophiae Doctor

Faculty of Mathematics and Natural Sciences

Department of Physics

September 2019

Series of dissertations submitted to the
Faculty of Mathematics and Natural Sciences, University of Oslo
No. 2183

ISSN 1501-7710

Cover: Hanne Baadsgaard Utigard.
Print production: Reprosentralen, University of Oslo.

Acknowledgements

This work has been carried out during the period from March 2015 to June 2018 as a part of the 4DSpace Strategic Research Initiative at the University of Oslo. During that period, I have been lucky to work with many passionate and talented people. Just some lines to express my gratefulness to important ones who influenced me the most.

I would like to express my sincere gratitude to my main supervisor Ketil Røed for all things he has done for me. Thank you for your all the valuable insight, discussions and support. I would like to thank my co-supervisor Philipp D. Häflige for introducing me to the research group as well as valuable discussions on ASIC development of our current measurement electronics.

I would also like to thank Tore André Bekkeng and Arne Pedersen, who both have guided me into the world of space instrumentation. Many thanks to Lasse B. N. Clausen, Jøran I. Moen, Wojciech J. Miloch and Andres Spicher for fruitful discussions and also support throughout last three and half years. Jøran, thank you for your effort in obtaining the financial support for this work. Special thanks also to Lasse and Jøran for your guidance in the thesis writing process. Espen Trondsen and Bjørn Lybekk, your help and assistance have been greatly appreciated. Further thanks to Halvor Strøm, David M. Bang-Hauge, Erlend Bårdsen and Stein S. Nielsen at ELAB for the support of PCB production and for sharing your practical experiences in electronics. I have also been fortunate to study and work with many brilliant students in the 4DSpace group and the electronics group of the Department of Physics.

Finally, I am very grateful for all the unconditional support and encouragement I have received from family during the PhD studies. I would also like to acknowledge the Norwegian Research Council, ESA PRODEX programme, Nano Network, Norwegian Space Center for financial support of projects and test campaigns I have been involved in.

Abstract

University of Oslo (UiO) has a desire to explore multi-scale physical processes giving rise to ionospheric scintillations, which implies the need for sub-meter spatial resolution of plasma measurements. One of the most common methods of plasma diagnostics is the Langmuir probe. Traditionally, by sweeping a bias voltage of an exposed Langmuir probe in a plasma, a current-voltage curve is obtained from which the plasma parameters can be derived. However, sweeping takes time and makes this approach unsuited for high spatial resolution measurements on fast moving space platforms. The multi-needle Langmuir probe (m-NLP) technique was developed by UiO to address this issue. A key feature of the m-NLP instrument is its ability to determine the electron density at very high spatial resolution without the need to know the plasma potential or electron temperature.

Since its first flight on board the Investigation of Cusp Irregularity 2 (ICI-2) sounding rocket from Svalbard in December 2008, the m-NLP instrument has been deployed on a variety of space platforms, e.g., the NorSat-1 microsatellite and the QB50 CubeSats. Furthermore, the instrument has been on board the Andøya Space Center (ASC) small-sized payloads, which was released from a NASA sounding rocket being launched from ASC in January 2019. The major advantages of unprecedented high spatial resolution plasma measurements, low mass and low power have made the m-NLP instrument attractive for small spacecraft applications. However, all in-situ measurements in space plasmas are challenged with spacecraft-plasma interaction effects, e.g., spacecraft charging and wakes. My research project was to identify and evaluate the most severe issues that need to be accounted for in further development of the UiO m-NLP instrument including the data analysis. I decided to investigate the following:

- Performances of the m-NLP instrument on the above-mentioned space platforms.
- Spacecraft charging, probe contamination and probe design issues.

– Evaluate and assess data analysis techniques for the m-NLP instrument.

In order to support the investigations, I have accessed data from a variety of missions including NorSat-1, QB50, ICI-2 and MICA. In addition, I have developed tests in the plasma laboratory at European Space Research and Technology Center (ESTEC). The main results from these investigations are:

– I demonstrate that the m-NLP system is capable of continuously resolving small-scale plasma structures as well as monitoring the platform potential on NorSat-1. For the QB50 satellites, a miniaturized thermionic electron emitter has been previously developed and included along with the multiple needle probes to alleviate spacecraft charging effects. It has also been demonstrated that the m-NLP system developed for QB50 has been successfully verified in the plasma chamber. Laboratory and in-situ data have validated operations of the electron emitter.

– Since the volume of the ASC payload (hockey puck shape with 100 mm in diameter and 45 mm in height) is very small, it is vulnerable to deploy the m-NLP system on board the ASC payload due to the risk of inter-probe sheath coupling. A possible solution to this issue is to deploy a single fixed-bias needle probe with high bias. The analysis using the ICI-2 data shows that, if the spacecraft is not charged to more negative potential than -2 V, electron density can be estimated within 10 % of the m-NLP calculated electron density, which is believed to be immune to the spacecraft charging.

– A needle probe as small as the m-NLP probes (typically 0.51 mm in diameter and 25 mm in length) is hardly affected by surface contamination as it is operating in the electron saturation region.

– Two data analysis techniques, i.e., linear and non-linear fits, for the m-NLP instrument have been studied using the ICI-2 data. The two approaches of estimating the electron density have advantages and disadvantages with respect to the current m-NLP implementation, and both can be applied to derive the plasma parameters.

– At present, the m-NLP probe is manufactured using only one guard/bootstrap. Thus, the probe edge near the bootstrapped part could potentially collect less electrons while the other open-ended edge could collect more electrons than the

rest of the probe. This would undesirably cause the electron current collection to deviate from the orbital-motion-limited (OML) theory. In order to mitigate the edge effect, the m-NLP probes are recommended to be made longer.

List of papers

Papers included in the dissertation

Paper 1: H. Hoang, L. B. N. Clausen, K. Røed, T. A. Bekkeng, E. Trondsen, B. Lybekk, H. Strøm, D. M. Bang-Hauge, A. Pedersen, A. Spicher and J. I. Moen (2018), The Multi-Needle Langmuir Probe System on Board NorSat-1, *Space Science Reviews*, *214*(75), doi: 10.1007/s11214-018-0509-2.

Paper 2: H. Hoang, K. Røed, T. A. Bekkeng, J. I. Moen, L. B. N. Clausen, E. Trondsen, B. Lybekk, H. Strøm, D. M. Bang-Hauge, A. Pedersen, C. D. A. Nokes, C. Cupido, I. R. Mann, M. Ariel, D. Portnoy, E. Sagi, The Multi-needle Langmuir Probe Instrument for QB50 Mission: Case Studies of Ex-Alta 1 and Hoopoe Satellites, *Space Science Reviews*, *215*(2), doi: 10.1007/s11214-019-0586-x.

H. Hoang, K. Røed, T. A. Bekkeng, E. Trondsen, L. B. N. Clausen,
W. J. Miloch and J. I. Moen (2017), High-spatial-resolution electron density measurement by Langmuir probe for multi-point observations using tiny spacecraft, *Measurement Science and Technology*, *28*(11), doi: 10.1088/1361-6501/aa87e1.

H. Hoang, K. Røed, T. A. Bekkeng, J. I. Moen, A. Spicher, L. B. N. Clausen, W. J. Miloch, E. Trondsen and A. Pedersen (2018), A study of data analysis techniques for the multi-needle Langmuir probe, *Measurement Science and Technology*, *29*(6), doi: 10.1088/1361-6501/aab948.

Papers not included in the dissertation

Paper 5: M. F. Ivarsen, H. Hoang, L. Yang, E. Trondsen, L. B. N. Clausen, A. Spicher, B. Lybekk, and J. I. Moen (2019), Multi-needle Langmuir probe operation and acute

probe current susceptibility to spacecraft potential, *IEEE Transactions on Plasma Science*, *47*(8), pp. 3816-3823, doi: 10.1109/TPS.2019.2906377.

Paper 6: C. Scharlemann, B. Seifert, R. Schnitzer, R. Kralofsky, M. Taraba, T. Dorn, T. Turetschek, H. Fauland, R. Plötzeneder, R. Stockinger, M. Schmid, T. Riel, A. Sinn, G. Janisch, F. Deisl, D. Kohl, B. Lybekk, H. Hoang, E. Trondsen (2018), PEGASUS-a review of in-orbit operation and obtained results, *69th International Astronautical Congress*, Bremen, Germany, 1 - 5 October.

Nomenclature

A_e	Electron collection area
A_i	Ion collection area
AC	Alternating Current
AIS	Automatic Identification System
ASC	Andøya Space Center
ASIC	Application Specific Integrated Circuit
C_p	Probe contamination capacitance
CAD	Computer Aided Design
Cal Poly	California Polytechnic State University
CLARA	Compact Lightweight Absolute Radiometer
DC	Direct Current
DMSP	Defense Meteorological Satellite Program
e	Electron charge
ESR	EISCAT Svalbard Radar
ECOMA	Existence and Charge state Of Meteoric dust grains in the middle Atmosphere
EISCAT	European Incoherent SCATter Scientific Association
ESA	European Space Agency
ESF	Equatorial Spread F
ESTEC	European Space Research and Technology Center
EUV	Extreme Ultra-Violet
FGM	Digital FluxGate Magnetometer
FIPEX	Flux-Φ-Probe Experiment
FP7	European Union's Seventh Framework Programme for Research
FPGA	Field Programmable Gate Array
GCI	Grand Challenge Initiative
GDI	Gradient Drift Instability
GNSS	Global Navigation Satellite System
GPS	Global Positioning System

GTR	Generalized Rayleigh-Taylor
HF	High Frequency
$\boldsymbol{I_e}$	Electron current
$\boldsymbol{I_i}$	Ion current
$\boldsymbol{I_{ph}}$	Photoelectron current
$\boldsymbol{I_s}$	Secondary emission current
$\boldsymbol{I_{total}}$	Total current
ICI	Investigation of Cusp Irregularities
INMS	Ion-Neutral Mass Spectrometer
ISS	International Space Station
I-V	Current-Voltage
IRI	International Reference Ionosphere
ISR	Incoherent Scatter Radar
$\boldsymbol{k_B}$	Boltzmann's constant
LEO	Low Earth Orbit
LEP-ESA	Low Energy Particle - ElectroStatic Analyzer
LT	Local Time
$\boldsymbol{m_e}$	Electron mass
$\boldsymbol{m_i}$	Ion mass
m-NLP	multi-Needle Langmuir Probe
MCU	Micro-Controller Unit
MICA	Magnetosphere Ionosphere Coupling in the Alfvén
MTEE	Miniaturized Thermionic Electron Emitter
$\boldsymbol{N_e}$	Electron density
$\boldsymbol{N_{e0}}$	Electron density of bulk plasma
$\boldsymbol{N_i}$	Ion density
NASA	National Aeronautics and Space Administration
NLP	Needle Langmuir Probe
NSC	Norwegian Space Center
OBC	On Board Computer
OML	Orbital Motion Limited
PCB	Printed Circuit Board
PMOD/WRC	Physikalisch-Meteorologisches Observatorium Davos/World Radiation Center
PhD	Philosophiae Doctor
P-POD	Poly-PicoSatellite Orbital Deployer

PRODEX	PROgramme de Développement d'Expériences scientifiques
q_i	Ion charge
r	Langmuir probe radius
R_p	Probe contamination resistance
R_{ps}	Probe sheath resistance
RPA	Retarding Potential Analyzer
RWP	Radio Wave Propagation
S	Slope of electron retardation region
S_{crit}	Spacecraft-to-probe surface area ratio
SPICE	Simulation Program with Integrated Circuit Emphasis
SPIS	Spacecraft Plasma Interaction Software
SuperDARN	Super Dual Auroral Radar Network
STM	Surface Thermal Monitor
T_e	Electron temperature
T_i	Ion temperature
TDMA	Time-division multiple access
TEC	Total Electron Content
TI	Texas Instruments
UART	Universal Asynchronous Receiver-Transmitter
UiO	University of Oslo
UT	Universal Time
UTIAS-SFL	University of Toronto, Institute for Aerospace Studies
UV	Ultra-Violet
V	Probe bias with respect to the plasma potential
V_b	Probe bias
v_{drift}	Drift velocity
V_f	Floating potential
V_p	Plasma potential
1U	1-Unit
2U	2-Unit
ϵ_0	Free-space permittivity
λ_D	Debye length

Contents

Chapter 1

Introduction

Due to solar extreme ultraviolet (EUV) radiation the upper terrestrial atmosphere is partly ionized. This part of the atmosphere is called the ionosphere and is, due to energy input from even higher altitudes, often structured across a multitude of spatial scales [e.g., Kintner and Seyler, 1985]. Fueled by this energy input, various plasma instability processes create inhomogeneous magnetic field-aligned density structures ranging from scales of tens of kilometers to meters [Basu et al., 1990], and in general these are most severe at high and low latitudes [e.g., Basu and Basu, 1981, Basu et al., 1988, 1998]. As these irregularities may interfere with and disturb all commercially used radio wave frequency bands, it would be of high value to be able to forecast the presence of severe events causing radio wave disturbances. This is of particular importance for the Global Navigation Satellite System (GNSS). In order to forecast, it is necessary to understand dynamics of the instability processes, the drivers as well as the plasma irregularity development and decay.

Moen et al. studied the effectiveness of gradient drift instability (GDI) by ground based measurements and concluded that high resolution in-situ measurements would be crucial to study the multi-scale processes involved in generating high-frequency (HF) backscatter instability targets [Moen et al., 2002]. The Investigation of Cusp Irregularities (ICI) sounding rocket program was initiated to explore the plasma instability processes, their mesoscale drivers and the resulting nature of plasma irregularities growth and decay in the auroral/polar ionosphere [e.g., Moen et al., 2013, and references therein]. It was suggested that electron density at kHz sampling rates would be necessary in such plasma

instability studies to achieve meter scale resolution, and the University of Oslo multi-needle Langmuir probe (m-NLP) instrument was invented for this purpose [Bekkeng et al., 2010, Jacobsen et al., 2010].

Since the initial work by Mott-Smith and Langmuir in 1920s [Mott-Smith and Langmuir, 1926], Langmuir probes have been widely used as diagnostic instruments for both laboratory and space plasma [Boggess et al., 1959, Brace, 1998, Brace et al., 1973, Chapkunov et al., 1976]. Traditionally, by sweeping a bias voltage of a Langmuir probe exposed in a plasma and measuring the collected current, a current-voltage (I-V) curve is obtained from which the plasma parameters can be derived. However, sweeping takes time and makes this approach unsuited for high spatial resolution measurements on fast moving space platforms. The m-NLP design uses several needle probes biased at different fixed voltages within the electron saturation region such that the currents to these probes can be sampled at a much higher rate, resulting in high-resolution plasma density observations. A key feature of the m-NLP technique is its ability to determine the electron density without the need to know the plasma potential or electron temperature. Under certain conditions, the m-NLP is even capable of monitoring the spacecraft potential and its variations as described in Bekkeng et al. [2013, 2017].

Since its first flight on board the Investigation of Cusp Irregularity 2 (ICI-2) sounding rocket from Svalbard in December 2008, the m-NLP instrument has been deployed on a variety of space platforms, e.g., the first Norwegian scientific satellite NorSat-1 and eleven Cubesats of the European QB50 constellation [Bekkeng et al., 2017, Hoang et al., 2018]. Furthermore, the instrument has been on board the Andøya Space Center (ASC) daughter payloads, which was released from a NASA sounding rocket being launched from ASC in January 2019. This experiment is expected to bring important lessons for the ICI-5 sounding rocket, on which a similar but better designed experiment is carried out. The major advantages of unprecedented high spatial resolution plasma measurements, low mass and low power have made the m-NLP instrument attractive to small spacecraft applications. However, all in-situ measurements in space plasmas are challenged with spacecraft-plasma interaction effects, e.g., spacecraft charging and wakes. My given research project was to identify and evaluate the most severe issues that need to be accounted for in further development of the UiO m-NLP instrument including the data analysis. I decided to investigate the following:

- Performances of the m-NLP instrument on the above-mentioned space platforms.
- Spacecraft charging, probe contamination and probe design issues.
- Evaluate and assess data analysis techniques for the m-NLP instrument.

In order to support the investigations, I have accessed data from a variety of missions including NorSat-1, QB50, ICI-2 as well as Magnetosphere Ionosphere Coupling in the Alfvén (MICA). In addition, I have developed tests in the plasma laboratory at European Space Research and Technology Center (ESTEC). This thesis is organized as follows. Chapter 2 introduces the environment in which the measurements were obtained as well as theoretical background of Langmuir probe measurements. Chapter 3 presents probe implementations and practical considerations for the probe deployment on spacecraft. The multiple space platforms where the experiments took place are generally described in Chapter 4. Chapter 5 consists of summaries and discussions of the four main papers as well as ideas of future works.

Chapter 2

Background

2.1 The ionosphere

The ionized part of the Earth's atmosphere is known as the ionosphere, which is a complex and dynamic region extending from 80 km to 1000 km [Rich and Basu, 1985, Schunk and Nagy, 2000]. This region is composed of mainly neutrals, free electrons and positive ions, which are produced by photoionization and energetic particle precipitation. While the photons, which causes the photoionization process, come from the Sun, energetic particles can come from cosmic rays, the Sun, the magnetosphere or from the ionosphere itself [Luhmann, 1995]. Once produced, the charged particles are affected by processes including chemical reactions, diffusion, plasma instabilities, and transport due to electric and magnetic fields.

Historically, the ionosphere is divided into three regions: D (below 90 km), E (between 90 and 130 km) and F (above 130 km). The dominant ion species of the D layer are NO^+ and O_2^+. These predominant ions can recombine with electrons, but at low altitudes electrons can attach themselves to neutrals to form negative ions. The main ionizing sources of this layer are solar ultraviolet (UV) radiation of 121.6 nm wavelength, solar X-rays in the range < 1 nm, solar protons with energies of 1 – 100 MeV and possibly solar electrons of energy > 10 keV. The E layer is usually noticeable since there is a local peak of the electron density around 110 km. The ions in this layer are O_2^+ and NO^+ which are produced by UV radiation in the 100 – 150 nm range and solar X-rays in the 1 – 10 nm range. The F region is the major region of the Earth's ionosphere. The region is regarded as most important from a radio communication and navigation systems viewpoint. Under certain solar-terrestrial conditions, the F region is split into

TABLE 2.1: Summary of the ionosphere layers.

Layer	Altitude [km]	Ionizing sources	Predominant ions
D	60 –90	UV radiation ($<$ 121.6 nm), solar X-rays ($<$ 1 nm), solar protons (1 – 100 MeV) and possibly solar electrons ($>$ 10 keV)	NO^+ and O_2^+
E	90 – 130	UV radiation (100 – 150 nm) and solar X-rays (1 – 10 nm)	NO^+ and O_2^+
F1	130 – 200	EUV radiation (5 – 102.7 nm)	O^+
F2	200 – 400	EUV radiation (5 – 102.7 nm)	O^+
Top-side F	$>$ 400	EUV radiation (5 – 102.7 nm)	O^+ and H^+

F1 and F2. A few hours after sunset, the F1 and F2 regions merge into one. The F layers are mainly composed of O^+. The main source of ionization in the F region is the extreme ultraviolet (EUV) radiation in the wavelength range from 5 to 102.7 nm. The height of F1 varies with solar activity, season and geomagnetic activity. The F2 layer is present all day under all solar-terrestrial conditions, but decreases in density at night. The top-side F electron density decreases with altitude and the layer primarily consists of O^+ and H^+ [Anderson et al., 1999]. Table 2.1 provides a summary of the altitude range, primary ionizing sources and predominant ion(s) for the ionosphere layers.

2.1.1 International Reference Ionosphere (IRI))

International Reference Ionosphere (IRI) is the international standard empirical model for the terrestrial ionosphere since 1999 [Bilitza et al., 2017, 2014]. While being unable to give us details of ionospheric dynamics, the IRI model provides average parameters such as electron density, electron and ion temperature, and the molecular composition in the range from 50 km to 2000 km altitude for a given location, time and date. Major data sources of the IRI model are worldwide networks of ionosondes, powerful incoherent scatter radars, the ISIS and Alouette topside sounders, and in-situ instruments flown on many satellites and rockets. Since ionosondes are an essential data source for the IRI model, the IRI model is known to be less accurate at high and low latitudes, where the ionosonde coverage is lower compared to mid-latitudes [e.g., Bilitza and Reinisch, 2008].

Figure 2.1 shows the electron density profile of the ionosphere above Svalbard at daytime (12:00 LT) and nighttime (24:00 LT) in solar minimum (July 1996) and solar maximum periods (July 2001) estimated by the IRI model. As can be seen, the electron densities

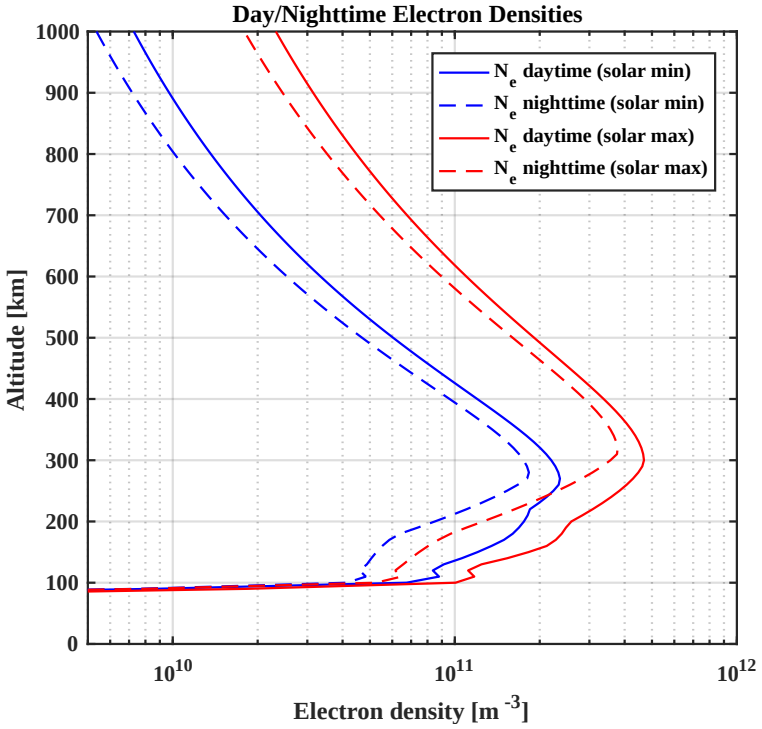

FIGURE 2.1: Typical high-latitude daytime and nighttime electron density profiles estimated by the IRI model.

peak at around 300 km altitude in the F region. The ionospheric plasma becomes more tenuous as the altitude increases from 300 km. The densities in the solar max period are about three to four times higher than those in the solar minimum.

Figure 2.2 shows the IRI model profile of neutral, ion and electron temperatures with the same location, date and time as Figure 2.1. It is seen that the temperatures at solar maximum are slightly higher than those at solar minimum. While the neutral temperatures during daytime and nighttime level off at an altitude of around 200 km, the electron temperatures increase significantly from about 400 K at 100 km to more than 2000 K at 300 km altitude. Regarding the ion temperatures, after a steep increase from 100 km to 150 km altitude, they gradually raise to more than 3000 K at 1000 km altitude.

2.1.2 Plasma structuring

Generally, ionospheric plasma structuring is poorly understood. At high latitudes the general consensus seems to be that as regions of high-plasma density, so-called polar cap patches, which are created near the dayside cusp region, drift across the polar cap

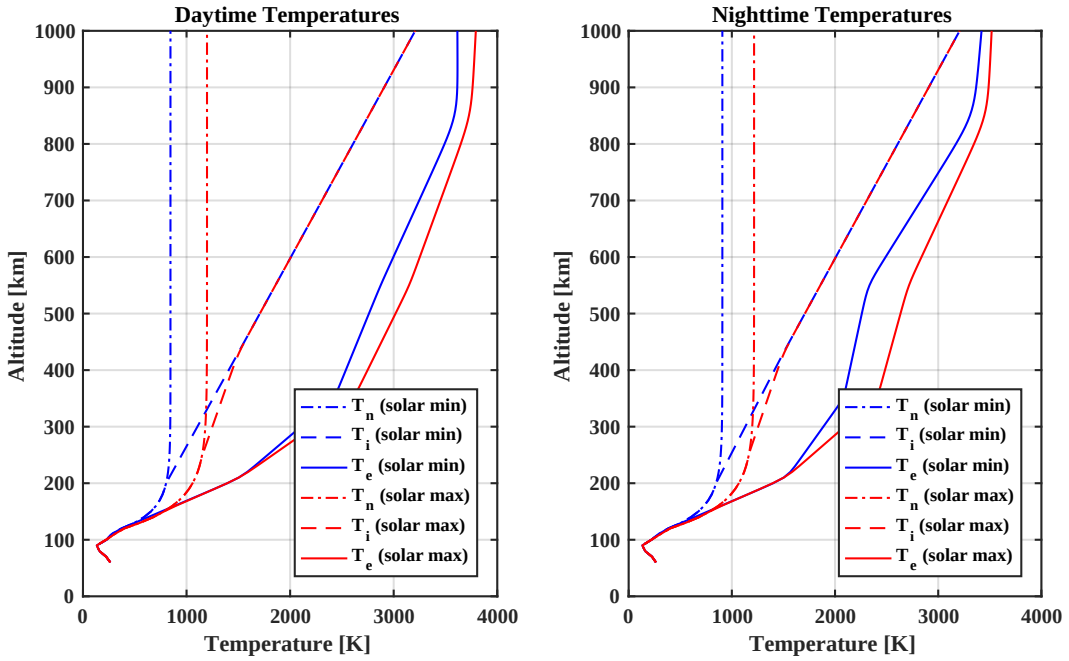

FIGURE 2.2: Typical high-latitude daytime and nighttime temperature profiles for neutrals, ions and electrons estimated by the IRI model.

driven by ionospheric convection [Buchau et al., 1983, McEwen and Harris, 1996, Moen et al., 2007, 2015, Oksavik et al., 2010, Zhang et al., 2015], their trailing edges provide favorable conditions for the growth of a macroscopic plasma instability called the gradient drift instability (GDI) [Simon, 1963, Tsunoda, 1988]. As this instability breaks up the drifting plasma density gradient associated with the polar cap patch [Basu et al., 1990, Gondarenko and Guzdar, 2004b, Weber et al., 1984], it creates plasma density structures on a variety of spatial scales ranging from kilometers down to meters [Gondarenko and Guzdar, 2004a, 2006]. These plasma density structures can then, if they are large in amplitude, introduce scintillations onto trans-ionospheric radio signals [e.g., Rino, 1979]. Contrast this knowledge with a large statistical study that finds no evidence for enhanced scintillation levels inside the polar cap at Global Navigation Satellite Systems (GNSS) frequencies, even when there is clear evidence of polar cap patches as shown in Clausen et al. [2016]. In the European Arctic sector, enhanced GNSS scintillation levels are attributed to high TEC levels in the auroral oval, at day and night [Jin et al., 2014, 2015, 2016].

Our knowledge about plasma structuring in the equatorial region is slightly better. Equatorial spread F (ESF) [Woodman and La Hoz, 1976] is now understood to be a consequence of the generalized Rayleigh-Taylor (GTR) instability acting on the edges of rising

"bubbles" of low plasma density. Most of the large-scale ionospheric plasma models for ESF deal with fluid-like or hybrid approaches, for which the dynamics of the ionospheric plasma or some of its species are treated as a continuum describing macroscopic (bulk) properties of the plasma species [e.g., Huba et al., 2008]. Such an approach has recently been successful in describing plasma dynamics and formation of ESF in the low-latitude ionosphere; in fact, with initial parameters from radars, these models can now predict the general evolution of ESF [Hysell et al., 2015]. However, these models omit kinetic effects linking the results to the smallest scales that can only be constrained by measurements at meter-scale resolution. There are still important open questions regarding the link across scale sizes, e.g., by what mechanism energy cascades from larger (10–100 kilometer) to smaller (10's of meters) scales and what initiates the instability [Woodman, 2009]. It is also unclear whether meter-scale irregularities are really just drifting passively with the background plasma as has been commonly assumed [Hysell et al., 2009]. Furthermore, we lack a comprehensive understanding of the day-to-day variability in the ESF occurrence. Also, the average spatial distribution of the small-scale density irregularities associated with this phenomenon is until now largely unknown [Rodrigues et al., 2009].

Essentially all our knowledge about ionospheric plasma density structures with scale sizes of a few tens to hundreds of meters was derived from indirect measurements. It was shown, for example, that electromagnetic signals received on the ground frequently contains fluctuations in amplitude and phase, so-called scintillations [Hey et al., 1946]. An example of dynamics of phase scintillations can be seen from Figure 2.3. These are imposed on the signal as the wave travels through an ionosphere that contained plasma density irregularities. These irregularities would locally alter the refractive index and, therefore, cause minute differences in the travel time for selected parts of the wave front, combining to cause sometimes significant signal distortions. It was hypothesized that plasma density structures at scale sizes around the Fresnel scale, i.e., a few hundred meters for typical frequencies used for GNSS, are most effective in causing signal scintillations. Thus, in order to better understand plasma structuring and instability drivers, in-situ high spatial resolution measurements are desirably needed.

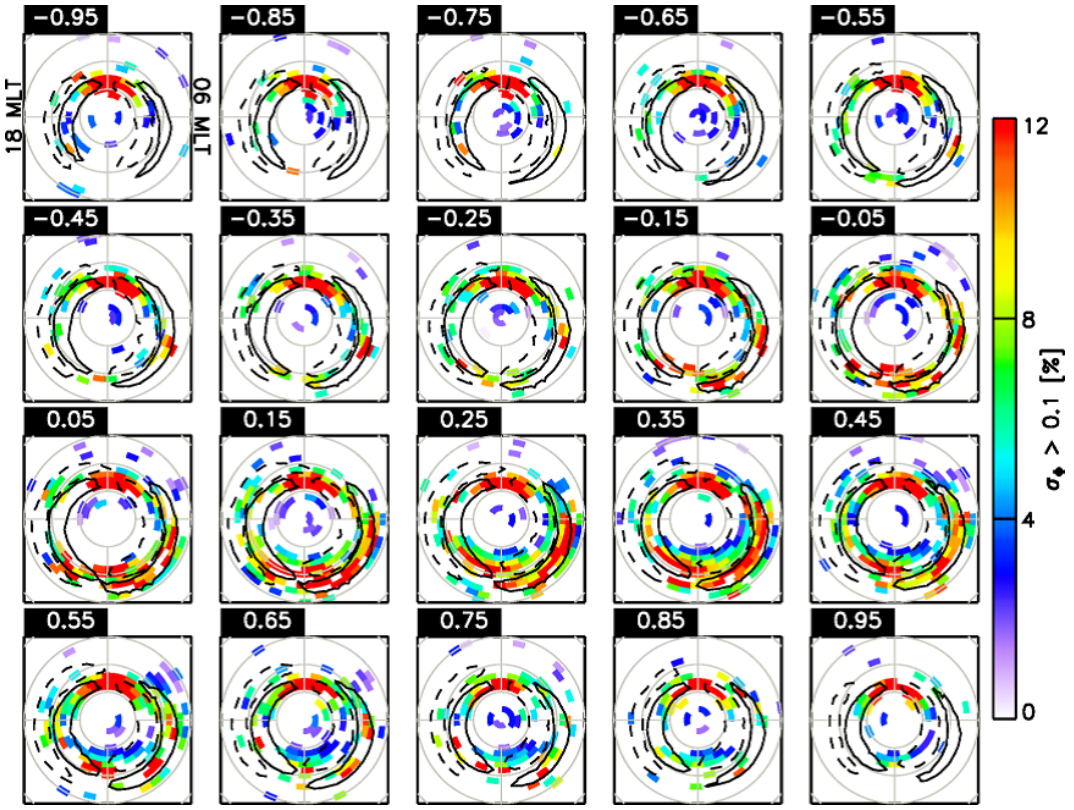

FIGURE 2.3: Dynamics of phase scintillations of Global Positioning System (GPS) signals inside the northern polar region during an average cycle of geomagnetic activity. The banana-shaped contours give the location of the upward (solid black lines) and downward (dashed back lines) region 1 and 2 field-aligned currents. Figure adopted from Clausen et al. [2016].

2.2 Langmuir probe theory

While the previous section introduces the ionospheric plasma and the plasma structuring, this section gives some basic aspects of Langmuir probe theory and how to use a Langmuir probe to measure characteristic parameters of the plasma.

2.2.1 Probe characteristic

DC sheath

A plasma is characterized by its quasi-neutrality, which means that the number of ions and electrons are nearly equal. When a positive electrode is immersed in a plasma, electrons are attracted and shield the electric field between the electrode and the plasma from the bulk plasma. By contrast, a negative electrode is surrounded by positive ions that shield the major portion of the plasma from the disturbing field caused by the electrode. This shielding region is referred to as the sheath. Figure 2.4 shows density and potential profiles of non-neutral regions, i.e., sheath and presheath, adjacent to a wall that is biased positively with respect to the potential of the bulk plasma assumed at zero. The presheath region is where the quasi-neutrality is still preserved, and the sheath region is where the neutrality does not exist, e.g., the electron density is higher than the ion density [Scheiner et al., 2015]. In the sheath region, the ion density decreases exponentially with increasing electric potential according to the Boltzmann relation $N_i = N_{e0}e^{eV/k_BT_i}$, where N_{e0} is the electron density of the bulk plasma, k_B is the Boltzmann constant, T_i is the ion temperature and V is the potential difference between the wall and the plasma. The electron density also decreases since the electron velocity increases closer to the wall. The electron and ion densities 'cancel out' at the sheath edge. The potential drops significantly from the wall potential in the sheath region. The sheath thickness is in order of the Debye length, which is given by

$$\lambda_D = \sqrt{\frac{\varepsilon_0 k_B T_e}{N_e e^2}}, \tag{2.1}$$

where ε_0 is the free-space permittivity, T_e is the electron temperature, N_e is the electron density and e is the electron charge. The Debye length is independent of the wall potential, but the sheath thickness will expand as the wall potential increases.

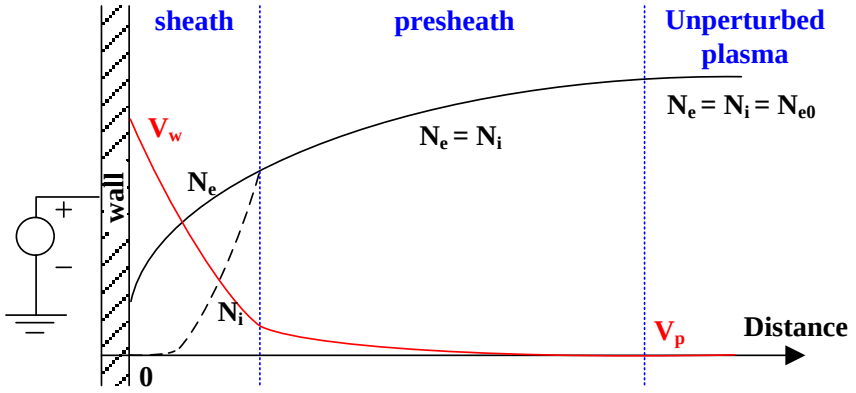

FIGURE 2.4: Density and potential profiles of non-neutral regions adjacent to a wall that is biased positively relative to the plasma potential. The sheath thickness is in order of the Debye scaling length.

I-V characteristic curve

The Langmuir probe principle is based on sweeping the bias voltage of an electrode exposed to a plasma and measuring the collected currents from the electrode. A representative I-V characteristic curve is shown in Figure 2.5, where three operational regions of electron saturation, electron retardation and ion saturation are separated by the plasma potential and the floating potential. Towards negative voltages, where all the electrons are repelled, is the ion saturation region. Note that the ion current has been significantly exaggerated for clarity in the figure. The plasma floating potential, V_f, is the equilibrium potential attained by a conductor immersed in a plasma, such that the total current of electrons and ions to the conducting surface sums to zero. In the electron retardation region, the ion current is negligible, and the electrons are partially repelled by the negative potential $V_b - V_p$, where V_b is the electrode (i.e., probe) bias and V_p is the plasma potential at which no fields/sheath exist between the probe surface and the surrounding plasma. If the particles in the plasma have the Maxwellian velocity distribution, this part of the curve is exponential. The plasma potential is normally of the order of $\frac{5k_BT_e}{e}$ [Chen, 2003]. As V_b reaches V_p, all of the random thermal flux of electrons is collected. In the electron saturation region where all ions are repelled, the electron current grows only slowly because of the expansion of the sheath as the probe bias increases. From the I-V curve, the plasma parameters N_e, T_e, V_p can be determined. The plasma parameter determination by analyzing the I-V curve is described with more detail in Subsection 2.2.4.

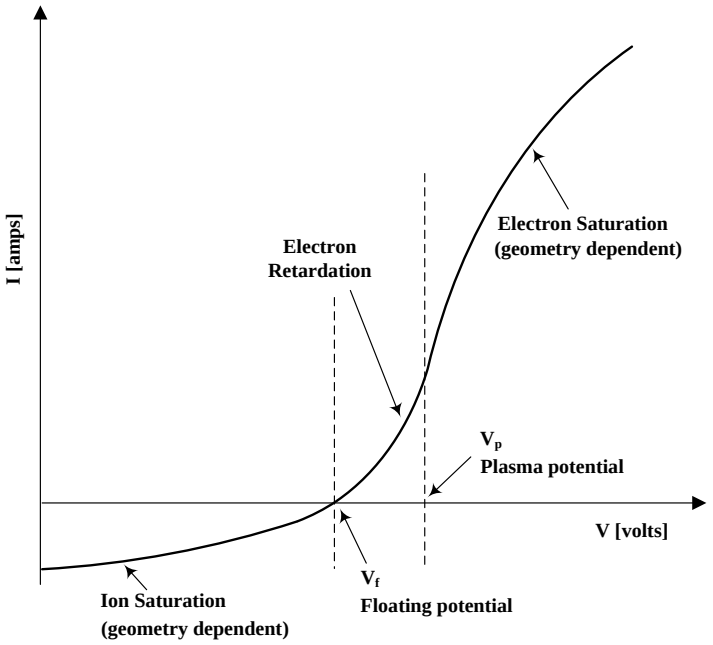

FIGURE 2.5: Representative I-V curve for a Langmuir probe. Note that the ion current has been significantly exaggerated for clarity of the figure.

2.2.2 Probe current collection

The current to and from a Langmuir probe can be expressed as follows:

$$I_{\text{total}} = I_e + I_i + I_{ph} + I_s, \tag{2.2}$$

where I_{total} is the total current, I_e is the electron current, I_i is the ion current, I_{ph} is the photoelectron current and I_s is the secondary emission current. In order to make the analysis simpler, the photoelectron and secondary emission currents can be ignored. If a plasma has the Maxwellian velocity distribution, the thermal average velocity of species j can be expressed by

$$v_j = \sqrt{\frac{2k_B T_j}{m_j}}, \tag{2.3}$$

where T_j is the species temperature and m_j is the species mass. For a plasma in the F region with a species temperature of 1000 K, the electron thermal velocity is about 174 km/s and the O^+ ion thermal velocity is roughly 1 km/s. While the electron thermal velocity is much higher than the spacecraft velocity, i.e., 1 km/s for sounding rockets and 8 km/s for LEO satellites, the velocity of the predominant ion in the ionosphere F

region is comparable or smaller. This situation is generally referred to as mesothermal plasma and mainly affects the ion saturation region [Barjatya et al., 2009].

The electron current to a Langmuir probe can be described using the orbital-motion-limited (OML) theory, which is also known as the thick sheath theory, proposed by Mott-Smith and Langmuir [Mott-Smith and Langmuir, 1926]. The theory deals with collisionless electron and ion trajectories surrounding an electric probe with its radius much smaller than the Debye length, assuming the plasma outside the sheath to be perfectly neutral. In general, the electron current collected by a Langmuir probe in a non-drifting, collisionless and unmagnetized plasma as described by the OML theory is:

$$I_e = C I_{e0} \left(1 + \frac{eV}{k_B T_e}\right)^{\beta} \qquad \text{if } V > 0 \tag{2.4}$$

$$I_e = I_{e0} \exp\left(\frac{eV}{k_B T_e}\right) \qquad \text{if } V \leq 0, \tag{2.5}$$

where $C = 2/\sqrt{\pi}$ for a cylindrical geometry and $C = 1$ for planar and spherical geometries of the probe. $I_{e0} = N_e A_e e \sqrt{\frac{k_B T_e}{2\pi m_e}}$ is the electron thermal current to the probe at the plasma potential and A_e is the electron collection area, V is the probe bias with respective to the plasma potential. The parameter β is equal to 0, 0.5 and 1 for a planar, cylindrical and spherical probe, respectively. Further the OML current expression of a cylindrical probe requires $eV/k_B T_e > 2$ [Mott-Smith and Langmuir, 1926].

While the electron current is regarded as non-drifting since the electron thermal velocity is much higher than the probe velocity (as it is mounted on a spacecraft), the ion current has to be modeled using the collection theory with superimposed drift [e.g., Bekkeng, 2017, Suresh, 2011, and references therein]. The ion collection currents for planar, cylindrical and spherical probes are expressed as the following:

$$I_i = A_i N_i q_i v_{\text{drift}} \qquad \text{for a planar probe} \tag{2.6}$$

$$I_i = A_i N_i q_i v_{\text{drift}} \sqrt{1 + \frac{2q_i V}{m_i v_{\text{drift}}^2} + \frac{k_B T_i}{m_i v_{\text{drift}}^2}} \qquad \text{for a cylindrical probe} \tag{2.7}$$

$$I_i = A_i N_i q_i v_{\text{drift}} \left(1 + \frac{2q_i V}{m_i v_{\text{drift}}^2} + \frac{k_B T_i}{m_i v_{\text{drift}}^2}\right) \qquad \text{for a spherical probe,} \tag{2.8}$$

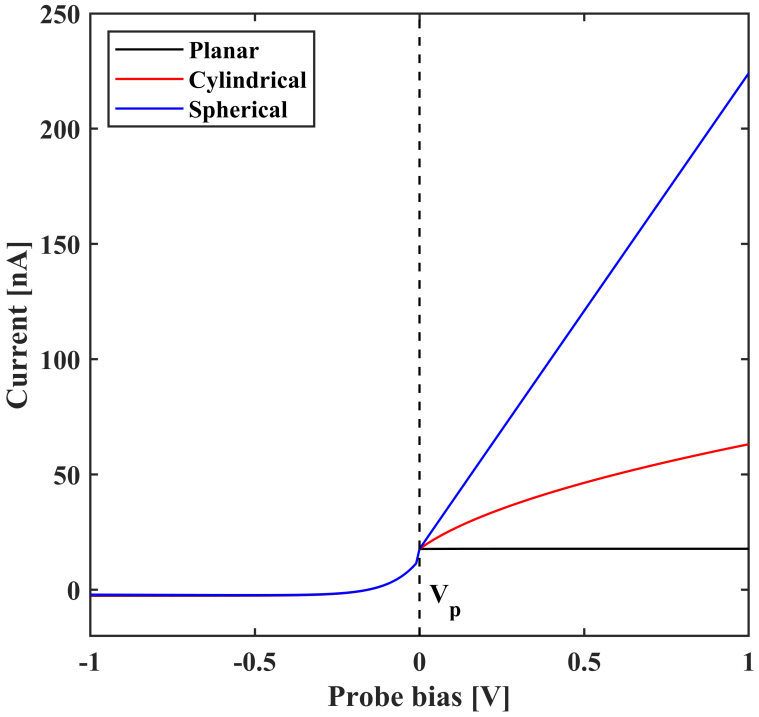

FIGURE 2.6: I-V curves for different Langmuir probe geometries in a plasma $N_e = N_i = 10^{11}$ m^{-3}, $T_e = T_i = 1000$ K and ion drift velocity is 8 km/s. The probe bias is relative to the plasma potential V_p. The planar and spherical probes have the same collection area as the cylindrical one with a length 25 mm and a diameter of 0.51 mm.

where A_i is the ram ion collection area, q_i is the ion charge, T_i is the ion temperature (which is approximated to the electron temperature for the quasi-neutral plasma) and v_{drift} is the drift velocity. Typical I-V curves for the three different Langmuir probe geometries in a plasma environment with $N_e = N_i = 10^{11}$ m^{-3}, $T_e = T_i = 1000$ K and the ion drift velocity is about 8 km/s are shown in Figure 2.6. The probe is biased with respect to the plasma potential V_p indicated at the black dashed line. The planar and spherical probes have the same collection area as the cylindrical one with a length 25 mm and a diameter of 0.51 mm.

2.2.3 Laframboise's numerical method

In the case of a collisionless OML sheath, the species collection current characteristics of cylindrical and spherical probes have simple analytical forms in the sheath limit [Mott-Smith and Langmuir, 1926]. The theory was then extended by Bernstein and Rabinowitz

TABLE 2.2: Laframboise's calculations for attracted Maxwellian-species current to cylindrical Langmuir probe ($T_i/T_e = 1$) [Laframboise, 1966].

		r/λ_D													
		0	1	1.5	2	2.5	3	4	5	10	20	30	40	50	100
$\pm\frac{eV}{k_BT_e}$	0	1	1	1	1	1	1	1	1	1	1	1	1	1	1
	0.1	1.0804								1.0803					
	0.3	1.2101							1.21	1.208	1.205			1.198	1.194
	0.6	1.3721							1.371	1.362	1.348			1.327	1.314
	1	1.556						1.554	1.549	1.523	1.486			1.439	1.409
	1.5	1.7551					1.754	1.747	1.735	1.677	1.605			1.523	1.478
	2	1.932					1.928	1.913	1.893	1.798	1.689			1.576	1.518
	3	2.2417			2.2417	2.237	2.226	2.192	2.151	1.98	1.801			1.638	1.561
	5	2.7555			2.75	2.731	2.701	2.626	2.544	2.22	1.94			1.703	1.599
	7.5	3.2846			3.266	3.227	3.174	3.05	2.92	2.442	2.06			1.756	1.628
	10	3.7388		3.735	3.703	3.645	3.567	3.402	3.231	2.622	2.157			1.798	1.65
	15	4.5114		4.493	4.439	4.342	4.235	3.99	3.749	2.919	2.319	2.082		1.868	1.686
	20	5.1695	5.1695	5.141	5.06	4.936	4.789	4.489	4.183	3.166	2.455	2.177	2.025	1.929	1.719
	25	5.7526	5.7525	5.711	5.607	5.462	5.291	4.926	4.565	3.384	2.576	2.262	2.092	1.983	1.747

who considered the full Poisson equation [Bernstein and Rabinowitz, 1959]. It was further refined by Laframboise who extended the calculation to Maxwellian distribution of attracted particles [Laframboise, 1966].

Laframboise has obtained complete numerical results for collected Maxwellian-species current of both spherical and cylindrical probes at arbitrary values of r/λ_D as respectively shown in Table 2.2 and Table 2.3. The normalized collected Maxwellian species current to the Langmuir probes is presented as a function of $\frac{eV}{k_BT_e}$ and r/λ_D. Third-order-analytic fits [Chiaretta, 2011] to the Laframboise's cylindrical and spherical probe currents for several values of r/λ_D are shown in Figure 2.7. At $r/\lambda_D = 0$, where the probe radius to the Debye length ratio is negligible, the computed currents are approaching the OML currents. For the cylindrical probe, the computed currents are not much different given $r/\lambda_D \leq 2$, whereas there is up to about 34% difference between the ideal OML ratio where $r/\lambda_D = 0$ and $r/\lambda_D = 2$ for the spherical probe. Thus, to have a valid operation within the OML regime, the spherical probe dimension is required to be much smaller than the Debye length more strictly as compared to the cylindrical one.

TABLE 2.3: Laframboise's calculations for attracted Maxwellian-species current to spherical Langmuir probe ($T_i/T_e = 1$) [Laframboise, 1966].

		r/λ_D													
		0.0	0.2	0.3	0.5	1	2	3	5	7.5	10	15	20	50	100
$\pm\frac{eV}{k_BT_e}$	0	1	1	1	1	1	1	1	1	1	1	1	1	1	1
	0.1	1.1				1.0999			1.099		1.098		1.097	1.095	1.094
	0.3	1.3				1.299		1.293	1.288		1.28		1.269	1.255	1.246
	0.6	1.6				1.595	1.584	1.572	1.552		1.518		1.481	1.433	1.402
	1	2				1.987	1.955	1.922	1.869		1.783		1.694	1.592	1.534
	1.5	2.5			2.493	2.469	2.399	2.329	2.219		2.05		1.887	1.719	1.632
	2	3			2.987	2.945	2.824	2.709	2.529		2.266		2.03	1.803	1.694
	3	4			3.97	3.878	3.632	3.406	3.068		2.609		2.235	1.91	1.762
	5	6			5.917	5.687	5.126	4.64	3.957		3.119		2.516	2.037	1.833
	7.5	8.5			8.324	7.871	6.847	6.007	4.887	4.094	3.62		2.779	2.148	1.891
	10	11			10.704	9.99	8.46	7.258	5.71	4.658	4.05		3.002	2.241	1.938
	15	16			15.403	14.085	11.482	9.542	7.167	5.645	4.796		3.383	2.397	2.022
	20	21			20.031	18.041	14.314	11.636	8.473	6.518	5.453	4.318	3.716	2.532	2.097
	25	26	25.763	25.462	24.607	21.895	17.018	13.603	9.676	7.318	6.053	4.719	4.018	2.658	2.166

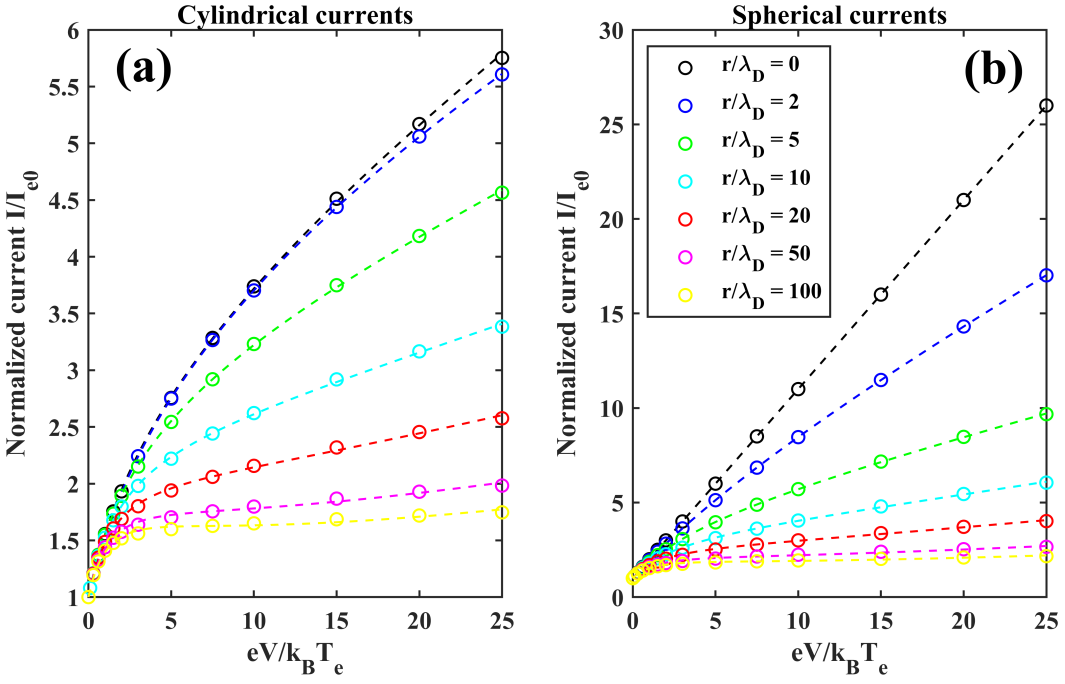

FIGURE 2.7: Analytic fits to computed Langmuir probe currents by Laframboise. (a) Cylindrical probe currents. (b) Spherical probe currents.

2.2.4 Plasma parameter extraction

Derivation of main plasma parameters

The electron temperature is determined in the electron retardation region. Taking the logarithm of Eq. 2.5 we obtain:

$$\log(I_e) = \frac{eV}{k_B T_e} + \log\left(N_e A_e e\sqrt{\frac{k_B T_e}{2\pi m_e}}\right). \tag{2.9}$$

The electron temperature is thus obtained from the slope of the retardation region S as:

$$T_e = \frac{e}{k_B S}. \tag{2.10}$$

At the plasma potential ($V = 0$), for a cylindrical probe, the electron and ion densities can be calculated from Eq. 2.4 and Eq. 2.7, respectively, as following:

$$N_e = \frac{\pi I_e\Big|_{V=0}}{eA_e}\sqrt{\frac{m_e}{2k_B T_e}} \qquad \text{and} \tag{2.11}$$

$$N_i = \frac{I_i\Big|_{V=0}}{eA_i v_{\text{drift}}}. \tag{2.12}$$

The ion density calculation assumes the drift velocity is sufficiently large compared to the ion thermal velocity, which is satisfied for the case of LEO spacecraft.

Data analysis methods

There are two main methods for determining the main plasma parameters including the electron density, ion density, the electron temperature and the plasma potential by analyzing the I-V characteristics of a Langmuir probe, i.e., a conventional graphical method and an analytical fitting method [e.g. Barjatya et al., 2009, Lebreton et al., 2006]. The two methods presented below are illustrated using measurement data, that is collected by a cylindrical Langmuir probe with 25 mm length and 0.51 mm diameter in the ESTEC plasma chamber. This chamber is 1 m in diameter and 2 m in length, with a plasma source generating argon ions accelerated to approximately 8 km/s towards

the probe. Figure 2.8(a) shows the obtained I-V curve, which is filtered before applying the analysis methods. All of the voltage values shown in the analysis are relative to the chamber ground.

A. The conventional graphical method consists of following steps:

1. Derive an approximation line for the ion saturation region as shown in Figure 2.8(b).
2. Subtract the ion saturation current from I_{total} to get I_e as shown in Figure 2.8(c).
3. Determine V_f at location where $I_{\text{total}} = 0$. V_f is found at about -0.85 V.
4. V_p can be determined by taking the first derivative of I_e as shown in Figure 2.8(d). The maxima location gives the V_p approximation of -0.7 V.
5. Locate the electron retardation region, estimate its slope S to calculate T_e as shown in Figure 2.8(e). Using Eq. 2.10, T_e is estimated to be about 410 K.
6. Compute the electron density using Eq. 2.11 and the ion density using Eq. 2.12 gives about $N_e = 3 \times 10^{11}$ m^{-3} and $N_i = 8.3 \times 10^{10}$ m^{-3}, respectively.

B. The analytical fitting method consists of following steps:

1. Perform steps (1−4) as the conventional graphical method to determine the floating potential and plasma potential. The ion density is then also estimated using step (6).
2. Fit the total current in the electron retardation region as expressed in Eq. 2.13 to the measured current for determining T_e, which is estimated at roughly 330 K using the fitting method. V_b in Eq. 2.13 is the probe bias.

$$I_{\text{total}} = -A_i N_i e v_{\text{drift}} + N_e A_e e \sqrt{\frac{k_B T_e}{2\pi m_e}} \exp\left(\frac{e\,(V_b - V_p)}{k_B T_e}\right) \tag{2.13}$$

3. With the knowledge of V_p and T_e, fit the electron current expressed by Eq. 2.4 to the measured current in the electron saturation region for determining N_e and β parameter, which are estimated to be about 3.3×10^{11} m^{-3} and 0.57, respectively.

As can be seen, the two analysis methods produce comparable values of the plasma parameters. However, the calculated ion density is about four times lower than the electron density. The ion collection area is determined assuming that only ram ions are collected. Even though this assumption could introduce errors regarding the collection area, this is not enough to result in significant difference between the ion and the electron density estimation. Thus it is believed that the plasma inside the chamber at the time of the measurement was not quasi-neutral. Moreover, ideally the β parameter according to OML theory should be 0.5. However, in practice under certain conditions this β parameter could fluctuate due to that the maximum radius of the probe for the OML validity varies with eV/k_BT_e and the ion to electron temperature [Sanmartin and Estes, 1999]. This issue is discussed in more detail in Paper IV.

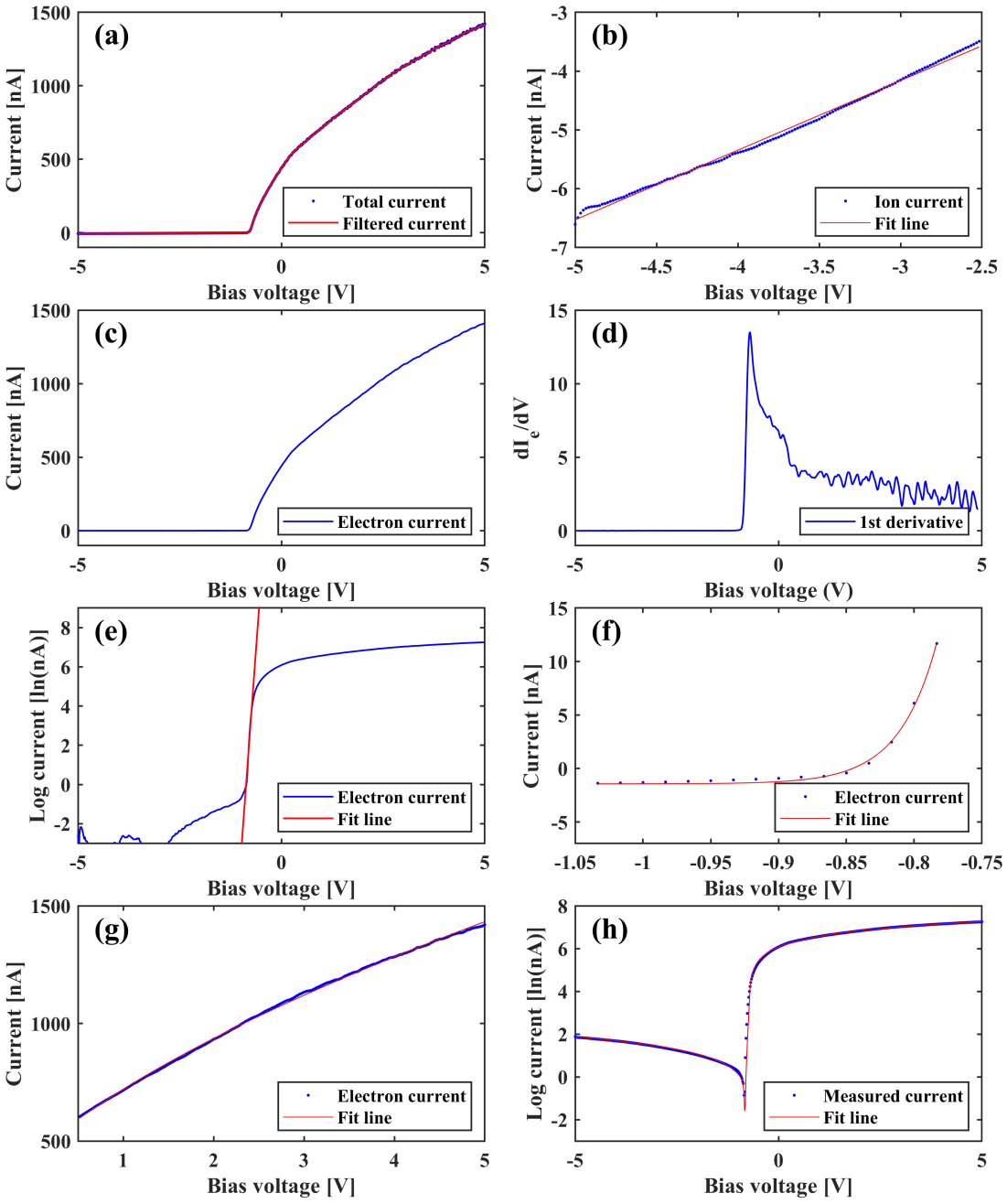

FIGURE 2.8: Plasma parameter extraction from data obtained by immersing a cylindrical Langmuir probe with 25 mm length and 0.51 mm diameter in a plasma chamber at ESTEC. (a) Measured current and filtered current. (b) Fit line to the ion saturation region. (c) Electron current. (d) First derivative of the electron current with respect to the bias voltage. (e) Linear fit to the retardation region presented in the logarithmic scale. (f) Non-linear fit to the retardation region in linear scale. (g) Fit line to the electron saturation region. (h) Measured and modeled I-V curves.

Chapter 3

Langmuir probe implementations and practical considerations for deployment on spacecraft

3.1 Langmuir probe implementations

There are different techniques for a Langmuir probe measurement. In this section, conventional techniques and the multi-needle Langmuir probe (m-NLP) technique, which was invented to characterize ionospheric plasma with a high-spatial resolution for plasma instability studies, are described.

3.1.1 Conventional techniques

Traditionally, both swept-bias and fixed-bias Langmuir probes are used as plasma diagnostics. The swept-bias technique sweeps through a range of voltages to obtain the I-V characteristic curve as shown in Figure 2.5, from which the plasma parameters including the electron density, electron temperature, ion density and plasma potential can be derived. However, sweeping takes time, typically on the order of $0.1 - 1$ second. For a LEO spacecraft, the sweeping time corresponds to the spatial resolution of 800 m – 8 km. Increasing the sweeping frequency requires much high data transmission rate as well as significantly large on board data storage capacity. Thus, this approach is considered to be unsuited for high spatial resolution measurements, i.e., plasma structure studies.

For the fixed-bias technique, a single fixed DC voltage is applied to a probe so that the probe works in the electron saturation region. While, the technique has an advantage as it supports high resolution measurements of the electron density, it is mostly used to measure relative changes in the density, and not the absolute value [Bekkeng, 2017]. The technique is also susceptible to changes in the floating potential of the reference platform where the probe is mounted. However, under certain conditions, the technique can possibly be used in small-sized spacecraft to estimate the absolute electron density with an acceptable accuracy as described in Paper III.

3.1.2 Multi-needle Langmuir probe technique

The m-NLP technique is described in detail in Bekkeng et al. [2010], Jacobsen et al. [2010]. The technique uses several cylindrical probes (commonly 0.51 mm diameter, 25 mm length) biased at different fixed voltages within the electron saturation region such that the currents to these probes can be sampled at a much higher rate, resulting in high-resolution plasma density observations. From Eq. 2.4, the electron saturation current of a cylindrical probe with a radius much smaller than the Debye shielding distance is in OML theory given as:

$$I_c = N_e A_e e \frac{2}{\sqrt{\pi}} \sqrt{\frac{k_B T_e}{2\pi m_e}} \sqrt{1 + \frac{eV}{k_B T_e}}, \tag{3.1}$$

where V is the probe bias potential, V_b, with respect to the plasma potential. It is noted that the equation used above is valid under the assumption of a non-drifting, collisionless and non-magnetized plasma. At our altitudes of interest ranging from above 90 km, all three assumptions are typically fulfilled [Jacobsen et al., 2010] since (i) the thermal speed of the electrons is much larger than the speed of the spacecraft relative to the plasma; (ii) the mean free path of the electrons is far greater than both the probe radius and the scale length of the electric potential distribution around the probe; and (iii) the Larmor radius is much larger than the probe radius. The current collection expression is a function of the applied bias potential relative to the plasma potential. The probe bias is relative to a common electrical ground, which is connected to the conductive parts of the satellite surface so the signal ground is the same as the floating potential of the payload platform.

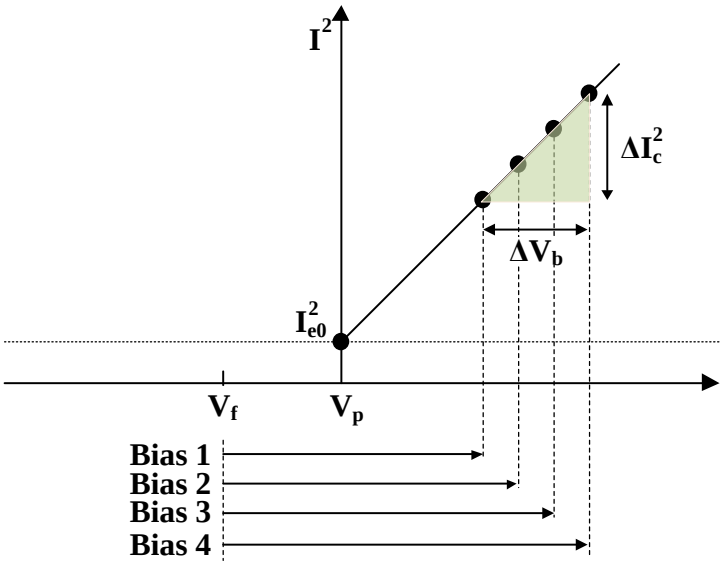

FIGURE 3.1: m-NLP measurement principle. Figure adapted from Bekkeng [2017].

The measurement method of the m-NLP system handles at least two probes biased at two different voltages above the plasma potential to determine the electron density as

$$N_e = \frac{1}{KA}\sqrt{\frac{\Delta\left(I_c^2\right)}{\Delta V_b}}, \tag{3.2}$$

where K is a constant given by $\frac{e^{3/2}}{\pi}\sqrt{\frac{2}{m_e}}$, $\Delta\left(I_c^2\right)$ is a difference in the square of collected currents and ΔV_b is a difference in the probe biases [Jacobsen et al., 2010]. A key feature of the m-NLP technique is its ability to determine the electron density without the need to know the plasma potential or electron temperature. Under certain conditions, the m-NLP is capable of monitoring the spacecraft potential and its variations as described in Bekkeng et al. [2013, 2017]. The m-NLP measurement principle is shown in Figure 3.1, where the $\Delta\left(I_c^2\right) - \Delta V_b$ slope is extrapolated down to the square of the electron thermal current $(I_{e0})^2$, from which the spacecraft charging potential can be determined.

3.2 Probe fabrication

The electron saturation current expression for a cylindrical probe given by the OML theory considers the ideal case of an infinitively long probe. Since it is not possible to make such a probe in reality, guard electrodes/bootstraps, which are biased at the

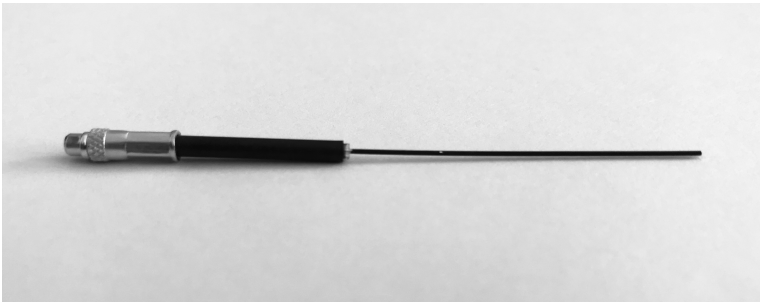

FIGURE 3.2: A typical needle probe with 25 mm length and 0.51 mm diameter, the bootstrap with 15 mm length and 2.2 mm diameter.

same potential as the probe itself, are commonly placed around the probe with a finite length. The aim is to make the electric potential structure around the probe as uniform as possible. At present, the needle Langmuir probe is manufactured using only one guard/bootstrap. Thus, the probe edge near the bootstrapped part could potentially collect less electrons while the other open-ended edge could collect more electrons than rest of the probe. This would undesirably cause the electron current collection to deviate from the OML theory. In order to mitigate the edge effect, it is desired that the m-NLP probes are longer as described in Paper IV. As we would like to make the m-NLP probes with their radius much smaller than the Debye length, which ranges from a few mm to tens of mm in the ionosphere, the probes have not been made thicker than 0.255 mm radius (or 0.51 mm diameter). Since the probe radius is significantly small, it is challenging to make such a good probe with a uniform electric potential surrounding it. An example of the probe fabrication is shown in Figure 3.2. However, Laframboise's numerical analysis as shown in Figure 2.7 indicates that the needle probe diameter could potentially be lager, i.e., $r/\lambda_D \sim 0.5$ while the expected probe collected current is still very close to the OML current. Thus, an improved probe fabrication has been planned for future space campaigns, e.g., increasing the probe radius and having two guards with negligible distances between the guards and the probe.

The deviation in the collected current can also arise from a variation in the work function of the probe surface. The variability in the surface behavior would cause local differences in the probe to plasma potential over the probe surface. The work function patchiness can be addressed by a probe coating. The coating can be, e.g., gold, rhenium, molybdenum, titanium nitride or carbon such as Aerodag or Aquadag. In most of our campaigns, the probe and bootstrap has been coated by Aerodag G to provide a uniform material work function.

3.3 Probe surface contamination

A well-known problem associated with DC Langmuir probe deployment is the probe surface contamination [Oyama, 1976]. This contamination occurs when the probe surface absorbs impurities, mainly water vapor. When sweeping up and down the bias of a contaminated probe in a plasma, one would obtain the I-V curve such that the swept upward path is different from the swept downward one. This phenomenon is called hysteresis, and because of it the plasma parameters, i.e., electron density and electron temperature, cannot be accurately estimated. Probe surface contamination is usually countered by deploying in-flight probe cleaning techniques such as internal heating or electron/ion bombardment. However, implementing these in-flight cleaning techniques is not always expedient. Another approach is to keep the cleaned probe in a sealed container prior to flight, and then release it in space. Unfortunately, during flight the probe can still be re-contaminated by water, which has a high dielectric constant (~ 80) and mainly contributes to temporal variations as if desorbed from the surface of the probe. While the contamination effect is possibly visible in swept-bias Langmuir probes in terms of the hysteresis in the I-V curve, the effect might exist even in fixed-bias Langmuir probes where it is not directly measurable [Piel et al., 2001, Steigies and Barjatya, 2012].

A contamination layer formed on the probe surface can be modeled by a capacitor C_p and a resistor R_p connected in parallel [Oyama, 1976, Steigies and Barjatya, 2012]. When a probe bias V_b is applied to the probe with respect to a reference electrode, i.e., a spacecraft platform, the probe current flows through the probe, the contamination layer, the sheath, the plasma and closes at the reference electrode. The effective voltage of the probe after passing through the contamination layer can be expressed as

$$V_{\text{eff}} = \frac{V_b R_{ps}}{R_p + R_{ps}}, \tag{3.3}$$

where V_{eff} is the effective voltage of the probe and R_{ps} is the probe sheath resistance. When the probe is clean, $R_p = 0$ so $V_{\text{eff}} = V_b$. As the probe is contaminated, R_p increases depending on the contamination level, making the effective voltage smaller than the applied probe bias.

The work by Oyama et al. [2012] experimentally confirmed that if the probe bias is swept fast enough, i.e., at several Hz, the hysteresis can be removed and accurate plasma

parameters can be derived from the obtained I-V curve. We carried out the sweep test with our fabricated cylindrical probe (25 mm length and 0.51 mm diameter). The obtained I-V curves with different sweep frequencies are shown in Figure 3.3. As can be seen, the hysteresis exists when the probe bias is swept at a low frequency of 0.01 Hz. The hysteresis is reduced but still visible when the bias sweeping frequency increases to 0.1 Hz. As the sweeping frequency increases to 1 Hz and above, the hysteresis disappears. Figure 3.3 indicates that the contamination can have a negative impact on the small-sized probe, i.e., our needle probe, in the electron retardation region but does not affect the probe if it operates well into the electron saturation region. Moreover, the electron saturation currents for different sweeping frequencies are almost similar. This agrees with our simulation analysis presented in Paper I. From the I-V curves without the hysteresis, we derive the electron density of about 1.6×10^{11} m^{-3} and the electron temperature of 1500 K.

3.4 Boom system

One of the main design challenges of the m-NLP instrument aboard a spacecraft is getting the probe tips into an area of undisturbed space plasma. As the spacecraft moves along its trajectory, it creates a 'plasma wake' in the opposite direction of travel. Because this 'plasma wake' is poorly understood and hard to predict, the probe tips are desired to be placed on long protruding booms, in an effort to place the tips as far out into the undisturbed plasma as possible. The boom system has to be deployable due to the limited dimension and volume of the spacecraft.

Figure 3.4 shows an example of a boom system design for the NorSat-1 satellite. The NorSat-1 m-NLP probe tips are placed on long deployable booms, whose overall length is limited by the length of the spacecraft itself. Two identical Langmuir probe cassettes are included on NorSat-1, each housing two probes. The cassettes have a total length of 400 mm, base width of 25 mm and height of 23 mm. The booms have a length of 370 mm, including the probes, and are held down by a uniquely designed mechanism. Through spring preloads, the booms are forced to stay stowed. Using a space-qualified shape-memory-alloy pin-puller from TiNi Aerospace Inc., the preloaded spring mechanism can be released in orbit via a command, allowing it to perform a half-turn, and consequently pushing both booms out with a large enough force to reach their fully deployed positions.

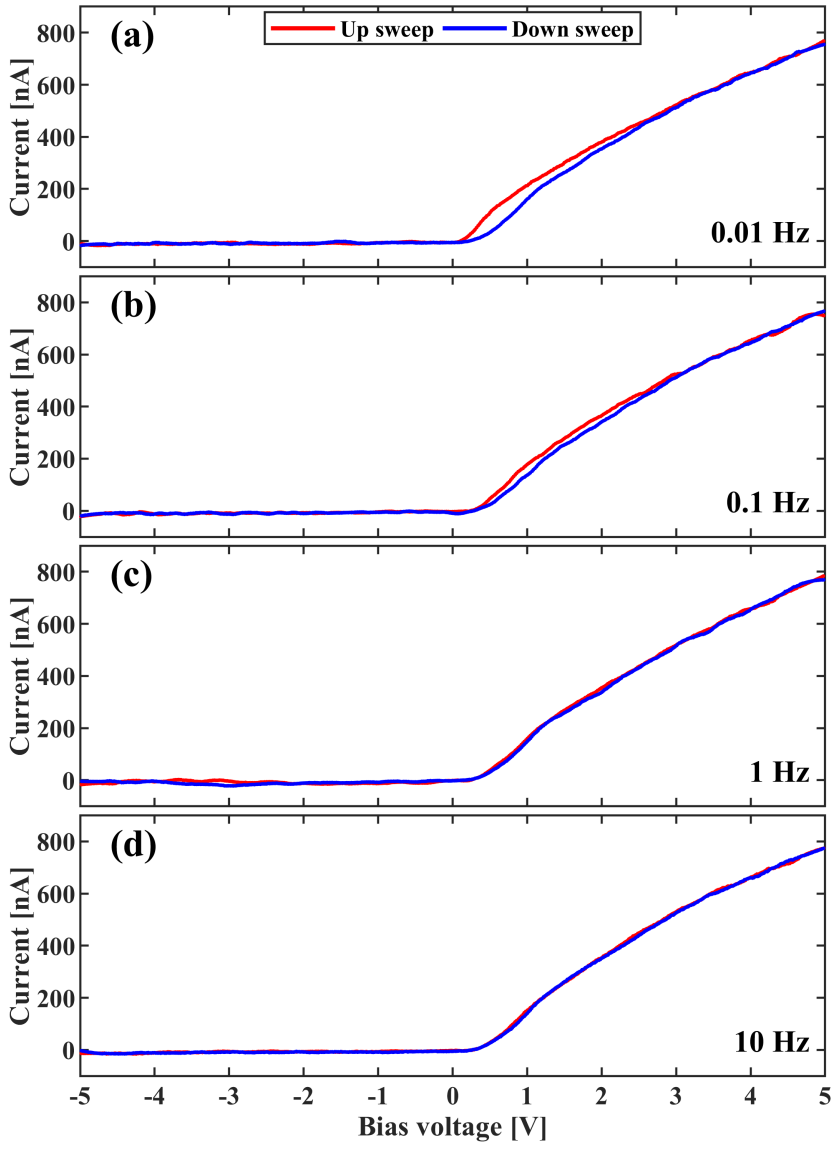

FIGURE 3.3: Sweep frequency dependence of the I-V curve hysteresis. (a) 0.01 Hz. (b) 0.1 Hz. (c) 1 Hz. (d) 10 Hz.

Once fully deployed, each of the booms would lock in place via a locking pin. While Figure 3.4(a) shows the boom system in stowed position, the boom system in deployed position is illustrated in Figure 3.4(b). The payload booms and probes after deployment are given a minimum clearance to the spacecraft platform or other payload equipment of about 15 cm.

3.5 Spacecraft charging and its effect on Langmuir probe measurements

The m-NLP probes by default are positively biased with respect to the spacecraft floating potential, in order to draw electron currents from the ambient plasma that are then used to determine the electron density. Current continuity thus requires a return ion current through conductive surfaces of the spacecraft bus that are connected to the power ground (reference electrode). Since the ion current is much smaller than the electron current due to its significantly lower mobility, either the spacecraft conductive surface area is expected to be sufficiently large to neutralize the charge caused by electrons collected through the probes or the spacecraft platform would be charged to highly negative potential values. If the spacecraft-to-probe-surface-area ratio is not higher than a critical value estimated by Amemiya and Fuchs [1991], the Langmuir probe measurement could be affected by the spacecraft charging. The critical value of the surface area is given as:

$$S_{\text{crit}} = \sqrt{\frac{\epsilon m_i}{2\pi m_e}}, \tag{3.4}$$

where S_{crit} is the critical value of the surface area and ϵ is the base of natural logarithm. In the ionospheric F region where O^+ is the dominant ion population, the critical ratio is about 115. While this condition can easily be met in sounding rocket applications, it is hard to achieve this condition for tiny spacecraft, like CubeSats and the ASC small-sized payloads. Particularly, as many of the QB50 satellite skin parts are not metallic, their conductive surfaces are very limited. For example, the total conductive surface area of Ex-Alta 1, an QB50 satellite, is at most 120 cm^2, which leads to the surface area ratio of just about 40. The small surface area ratio would not only cause the spacecraft to charge to highly negative potentials, possibly making the m-NLP probes unable to operate in the desired electron saturation region, but also expand the sheath

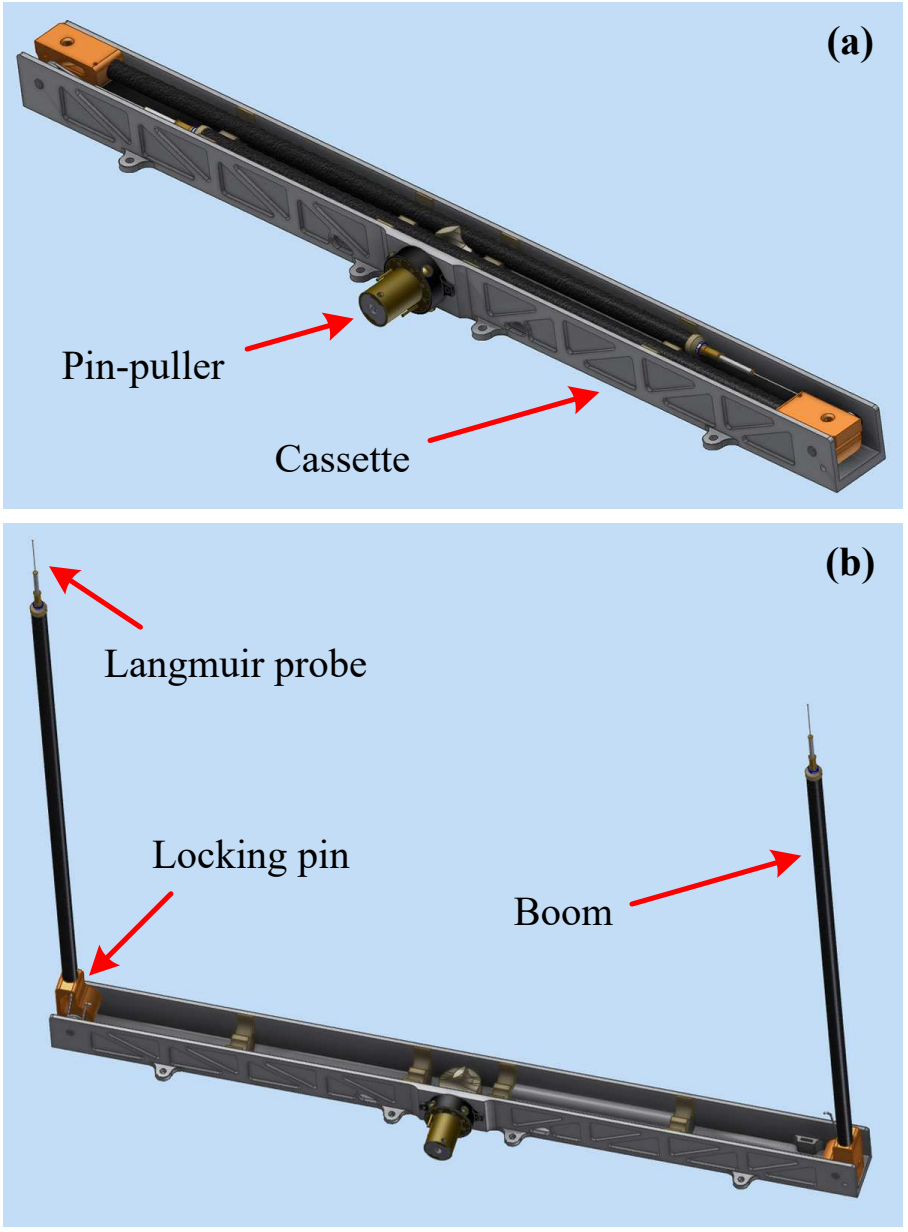

FIGURE 3.4: CAD drawing of NorSat-1 boom system design. The cassette has a total length of 400 mm, base width of 25 mm and height of 23 mm. The boom length including the probe is 370 mm. (a) Stowed position (b) Deployed position.

surrounding the spacecraft. For tiny spacecraft, the sheath expansion can modify the current collection of the Langmuir probes since the distances between the probes and the spacecraft platform are limited.

To address the limited surface area issue on tiny spacecraft, many charging mitigation solutions have been introduced such as electron-emitting film and electron emitters, a.k.a., electron gun. The work in Iwata et al. [2012] has shown that the developed 5 mm square film could emit a current from 10 to 100 μA for 4 hours. In the literature there are also reports of several electron guns, which are small in size and capable of emitting beam currents up to mA. However, none of those guns satisfy the targeted power consumption requirement of 100 mW for the QB50 CubeSats as well as the ASC payload. Therefore, a miniaturized thermionic electron emitter has been developed by the University of Oslo. The design details and test results are demonstrated in Bekkeng [2017], Hoang et al. [2017]. At 1.2V filament voltage, the beam current reaches up to 54 μA, 147 μA and 210 μA for the acceleration voltages 38 V, 76 V and 114 V, respectively, and the electron emitter power consumption is about 100 mW, which meets the low power consumption demand mentioned above. More detail can be found in Paper III.

Chapter 4

Experiments

4.1 NorSat-1 microsatellite

With one of the aims to open a new era in ionospheric research, the first Norwegian scientific satellite NorSat-1 was launched from Baikonur, Kazakhstan on July 14th, 2017. NorSat-1 is a multi-payload micro-satellite ($\sim$16 kg, 23 cm $\times$ 39 cm $\times$ 44 cm) that was commissioned by the Norwegian Space Center (NSC) and built by the University of Toronto, Institute for Aerospace Studies (UTIAS-SFL). A schematic drawing of the NorSat-1 satellite is shown in Figure 4.1, where X, Y and Z coordinates represent the satellite body coordinate system. The satellite was launched into a polar orbit at approximately 600 km altitude where it is expected to operate for at least three years. While its main objective is to monitor maritime traffic in Norwegian waters using a Automatic Identification System (AIS) receiver made by Kongsberg Seatex, NorSat-1 also carries two scientific instruments: (1) a Compact Lightweight Absolute Radiometer (CLARA) made by Physikalisch-Meteorologisches Observatorium Davos/World Radiation Center (PMOD/WRC) [Walter et al., 2017], intended to observe total solar irradiation and variations over time; and (2) the multi-needle Langmuir probe (m-NLP). The mission is operated from Vardø and Longyearbyen ground stations in Norway.

The m-NLP on board the NorSat-1 satellite gives us an ideal opportunity to study the high-latitude and low-latitude ionospheric plasma. With its sampling rate of up to 1 kHz, the m-NLP instrument aboard the NorSat-1 satellite provides an unprecedented opportunity to investigate plasma density structures down to a few meters at LEO. Science objectives of the NorSat-1 satellite using the m-NLP instrument are:

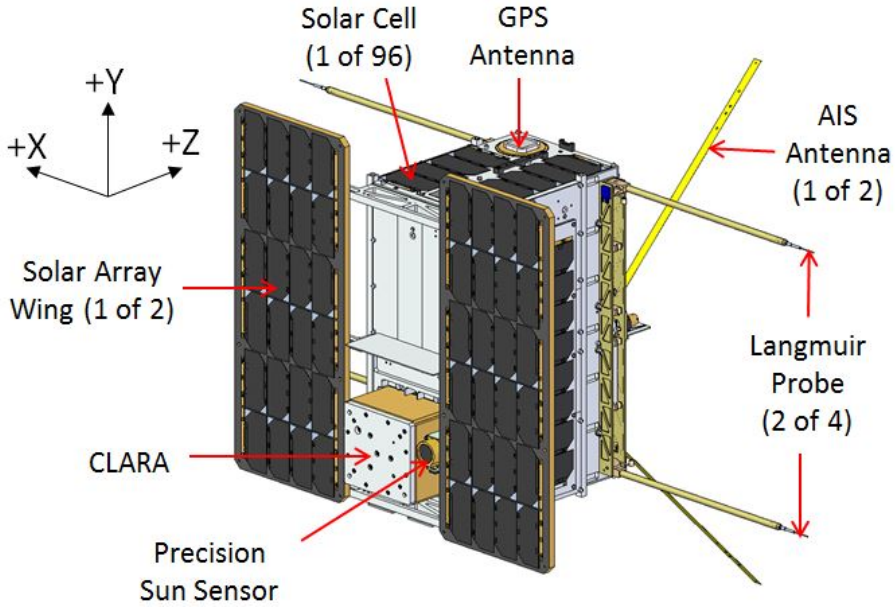

FIGURE 4.1: Schematic drawing of the NorSat-1 satellite. X, Y and Z coordinates represents a satellite body coordinate system. The m-NLP probes are mounted on booms that are deployed after its launch. The NorSat-1 is weighted approximately 16 kg and has dimensions of 23 cm×39 cm×44 cm. Image credit: UTIAS-SFL.

– Primary objective:

  - Identify and quantify the mechanisms that cause the generation of small-scale ionospheric plasma density structures.

– Secondary objectives:

  - Map the global spatial characteristics of meter-scale plasma structures in the ionosphere and their dependence on meso- and large-scale ionospheric drivers.
  - Provide physical understanding of ionospheric structuring mechanisms as the foundation for scintillation forecasts.
  - Understand spacecraft/ionosphere interaction and its impact on in situ plasma density measurements

The m-NLP measurement data will be combined with data from the Super Dual Auroral Radar Network (SuperDARN) and the Defense Meteorological Satellite Program (DMSP) satellites to get the 'big picture' context of the ambient plasma. Over the following years, the satellite will cross the equatorial and polar regions twice every 90 minutes, providing a wealth of data that will help us better understand the mechanisms

that dissipate energy input at larger scales by creating small-scale plasma density structures within the ionosphere. Within the scope of the dissertation, only first results from the m-NLP instrument commissioning phase are discussed (Paper I).

4.2 QB50 picosatellite constellation

QB50 is a project within the European Union's Seventh Framework Programme for Research (FP7) that aimed at launching a constellation of 50 CubeSats into the lower thermosphere at approximately 380 km altitude [Muylaert et al., 2009]. The region to be investigated is a poorly understood because it is difficult to reach experimentally. One of the main purposes of the QB50 project is to achieve sustained and affordable access to space for small scale research space missions and planetary exploration. The QB50 satellites are expected to operate for three to twelve months before burning up during re-entry. All QB50 satellites can carry their own instruments, but most of the satellites additionally accommodate a set of common science instruments to accomplish atmospheric research in the lower thermosphere. There are three different types of scientific instruments, each of which is part of the common instrument set. The Ion-Neutral Mass Spectrometer (INMS) is part of set 1. The Flux-Φ-Probe Experiment (FIPEX) is part of set 2 and the multi-needle Langmuir probe (m-NLP) science unit is part of set 3. A surface thermal monitor (STM) is installed in all satellites.

The idea with QB50 was to deploy several spacecraft like pearls on a string, which would be ideal for instability studies because the satellites would revisit instability regions allowing us to study growth and decay of structures, as was demonstrated during the commissioning of the Swarm mission [Goodwin et al., 2015, Spicher et al., 2015]. In addition to providing plasma density measurements, the main drivers for UiO to get involved with the QB50 mission are:

- Demonstrate that the m-NLP system can provide high resolution electron density measurements onboard CubeSats.
- Explore the temporal evolution of F-region plasma irregularities in the polar caps and in the equatorial region.

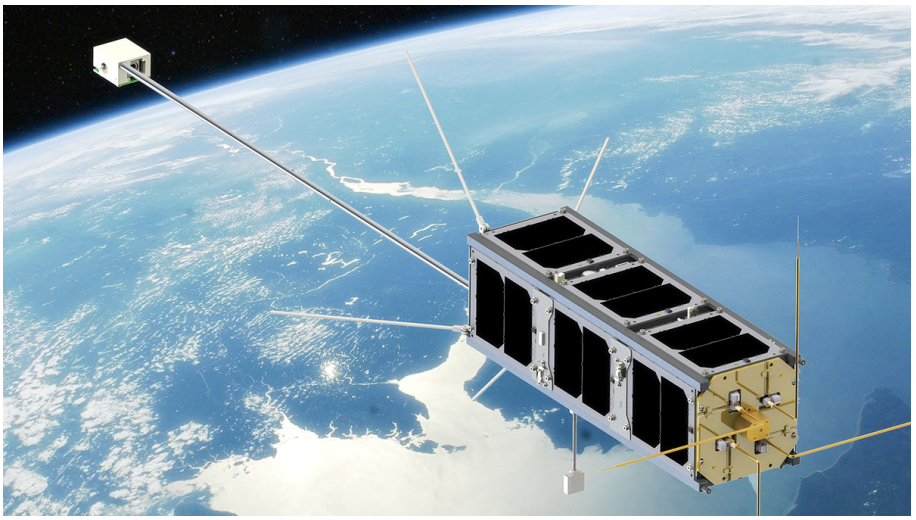

FIGURE 4.2: QB50 Ex Alta-1. (Image credit: University of Alberta)

Even though the m-NLP instrument is originally aimed at providing high resolution data, there is a practical limitation of 2 MBit/day of generated data that is the main limiting factor for how the instrument operates. Nominal sample rate is about 10 Hz, but higher data rates can be obtained in selected parts of the orbit. The m-NLP science unit has four needle Langmuir probes and has been adapted to be deployed on the QB50 satellites by: (i) lowering the power consumption, (ii) introducing onboard data processing (due to telemetry constraints), and (iii) developing an electron emitter to control the spacecraft potential [Bekkeng et al., 2017]. In addition, since the spacecraft conductive surface area of CubeSats is much smaller than that of sounding rockets, the probe diameter has been reduced from 0.51 mm for the sounding rocket version to 0.29 mm, to alleviate effects of spacecraft charging. Each of the m-NLP probes is 25 mm in length and has the bootstrapped section of 1.19 mm in diameter and 15 mm in length. The m-NLP system on a fleet of CubeSats is expected to be the most cost effective approach to monitor the dynamics of the problem regions and hence be valuable to regional or global forecast services.

Within the scope of the dissertation, preliminary in-orbit data from two QB50 satellites, Ex-Alta 1 and Hoopoe are reported (Paper II). Ex-Alta 1 and Hoopoe are 3U and 2U Cubesats developed by Alberta University, Alberta, Canada, and Space Laboratory of the Herzliya Science Center, Israel, respectively. They were both launched on May 18, 2017 from the International Space Station (ISS). Due to the low bandwidth and limited power on the two satellites, the m-NLP instrument has been in operation only a few times since its launch into orbit. Figure 4.2 illustrates a rendering model of Ex-Alta 1

satellite, carrying the m-NLP instrument in front (ram side). The science unit extends 36 mm, including the connector, downwards into the QB50 CubeSat structure, from the bottom side of the science unit top plate. In addition to the m-NLP science unit, the Ex-Alta 1 satellite carries a digital fluxgate magnetometer (FGM) [Miles et al., 2013, 2016], which is used for high frequency measurements of the Earth's magnetic field. The magnetometer is encased in a box mounted on a long boom behind the satellite.

4.3 ASC small-sized payload

Figure 4.3 shows a new payload module concept developed by Andøya Space Center (ASC) to enable multi-point measurements [Lindahl, 2015]. The module is a so-called daughter payload in the shape of a hockey puck. Since the payload module has been designed to be stackable and scalable, a cloud of these payloads can be released from either a mother sounding rocket or satellite to measure temporal variations and spatial gradient of the plasma parameters. While the daughter payload version shown in Figure 4.3 is designed for sounding rocket applications, for satellite applications a few adaptations need to be made, e.g., solar panels are included for longer operations.

The bottom left of Figure 4.3 shows a mechanical design of the daughter payload, which has a diameter of 100 mm, height of 45 mm and mass of around 350 g. The daughter payload accommodates an instrumentation section, which runs either the m-NLP or single needle Langmuir probe (NLP) system to characterize the ambient plasma with high sampling rate up to 1 kHz. The instrument system design has heritage from our sounding rocket and satellite versions of the instrumentation system.

Within the scope of the thesis, only a study of the deployment feasibility of the ASC daughter payloads is reported (Paper III). However, at the time of writing this thesis, we have completed the fabrication of the Langmuir probe-based instrumentation section of the daughter payload with a new electronics design. For the first experimental demonstration for the multi-point electron measurement, a deployment mechanism has been developed to deploy six daughter payloads from a sounding rocket. The six payloads are placed on a carousel deck named 4DSpace experiment deck as shown in Figure 4.4(b). The 4DSpace deck has a height of 228.6 mm and a weight of about 20 kg excluding the daughters. At an altitude of about 70 km, the carousel is activated to rotate and

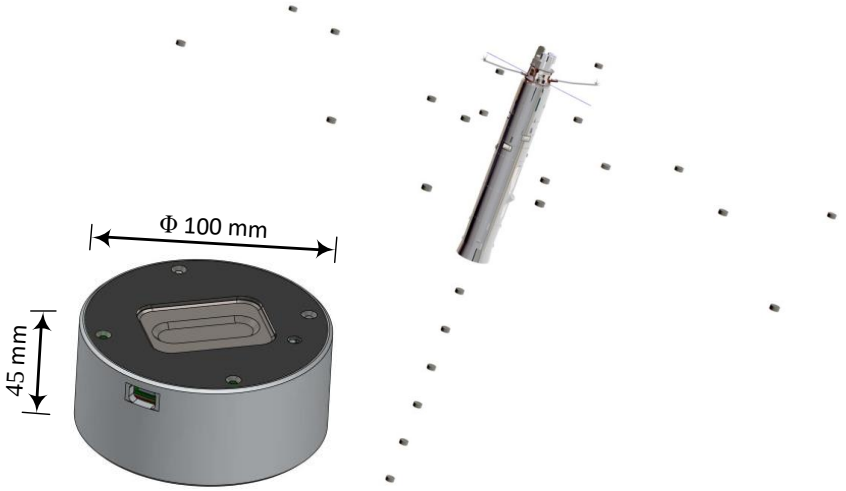

FIGURE 4.3: Cloud of ASC daughter payloads released from a sounding rocket for multi-point measurements. Image credit: Andøya Space Center.

release pairs of the daughter payloads as shown in Figure 4.4(a). The minimum release time is about 4 s. The rocket is spinning at around 4 revolutions per second. Due to the centrifugal force exerted on the daughters, they are launched on an escape vector orthogonal to the rocket trajectory at a velocity of roughly 4.4 m/s. The link capacity of the first demonstration is limited to 125 kps. The communication section on the mother rocket employs the time-division multiple access (TDMA) scheme to receive data from the six daughters. The daughters was expected to be in communication range from the mother up to about 1200 – 2000 m separation. The 4DSpace experiment deck has been integrated to a NASA sounding rocket, which is an essential part of Grand Challenge Initiative (GCI), a large-scale international collaboration targeting advancement in our understanding of cusp region space physics. The rocket was launched from ASC in January 2019 with an apogee of about 150 km. This experiment will be followed by a similar but better designed experiment carried on the ICI-5 sounding rocket, which is aimed for December 2019.

4.4 Sounding rockets

The sounding rocket experiments within the scope of this thesis are ICI-2 and MICA missions (Paper III and Paper IV). The ICI sounding rocket program was initiated to explore plasma instability processes, their mesoscale drivers and the resulting nature of plasma irregularities growth and decay in the auroral/polar ionosphere (e.g., Moen

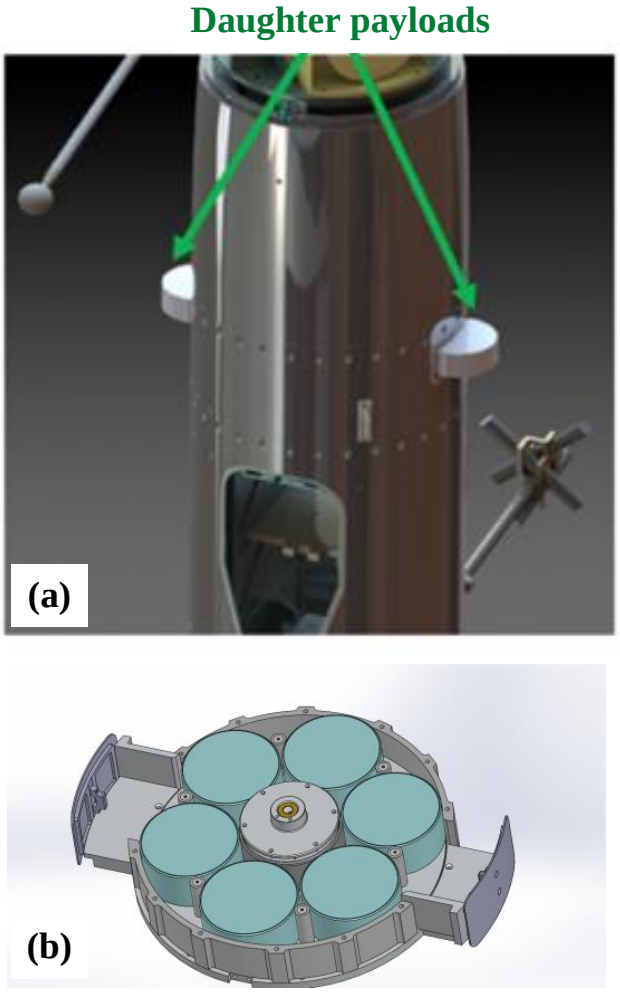

FIGURE 4.4: Release mechanism for the daughter payloads on board sounding rockets. (a) The daughters are released in pair. (b) Carousel deck named 4DSpace experiment deck, which houses the six daughter payloads. Image credit: Andøya Space Center.

et al. [2013] and references therein). The main objective for the ICI-2 rocket mission was to carry out the first in-situ measurements of the decameter backscatter targets in the cusp ionosphere, and to test the GDI and its drivers [Lorentzen et al., 2010, Moen et al., 2012, Oksavik et al., 2010]. The rocket was launched from Ny-Ålesund, Svalbard on 5 December 2008. Figure 4.5 shows the ICI-2 payload, which also accommodates an instrumentation package including the m-NLP system, a fixed-bias spherical probe, E-field double probes, two AC and DC magnetometers, a low energy particle experiment (LEP-ESA) and a sounding rocket attitude determination system. Figure 4.6 shows the rocket vehicle, which has two stages carrying the payload with 356 mm diameter, 2915 mm long. While the second stage motor and the payload are always connected, the 1st stage motor is separated from the second stage after running out of fuel.

The MICA sounding rocket was launched from Poker Flat, Alaska on 18 February 2012. In addition to the m-NLP system, the instrumentation package aboard MICA includes other instruments such as magnetometer, GPS TEC receiver, petite ion probes (PIP), low energy electron spectrometer, E-field and plasma wave instrument. The aims of the mission are to investigate the role of active ionospheric feedback in the development of large amplitude and small scale electromagnetic waves and density depletions in the low altitude ($<$ 400 km), downward current, auroral ionosphere. Further detail about the MICA mission can be found in, e.g., Fisher et al. [2016], Lynch et al. [2015].

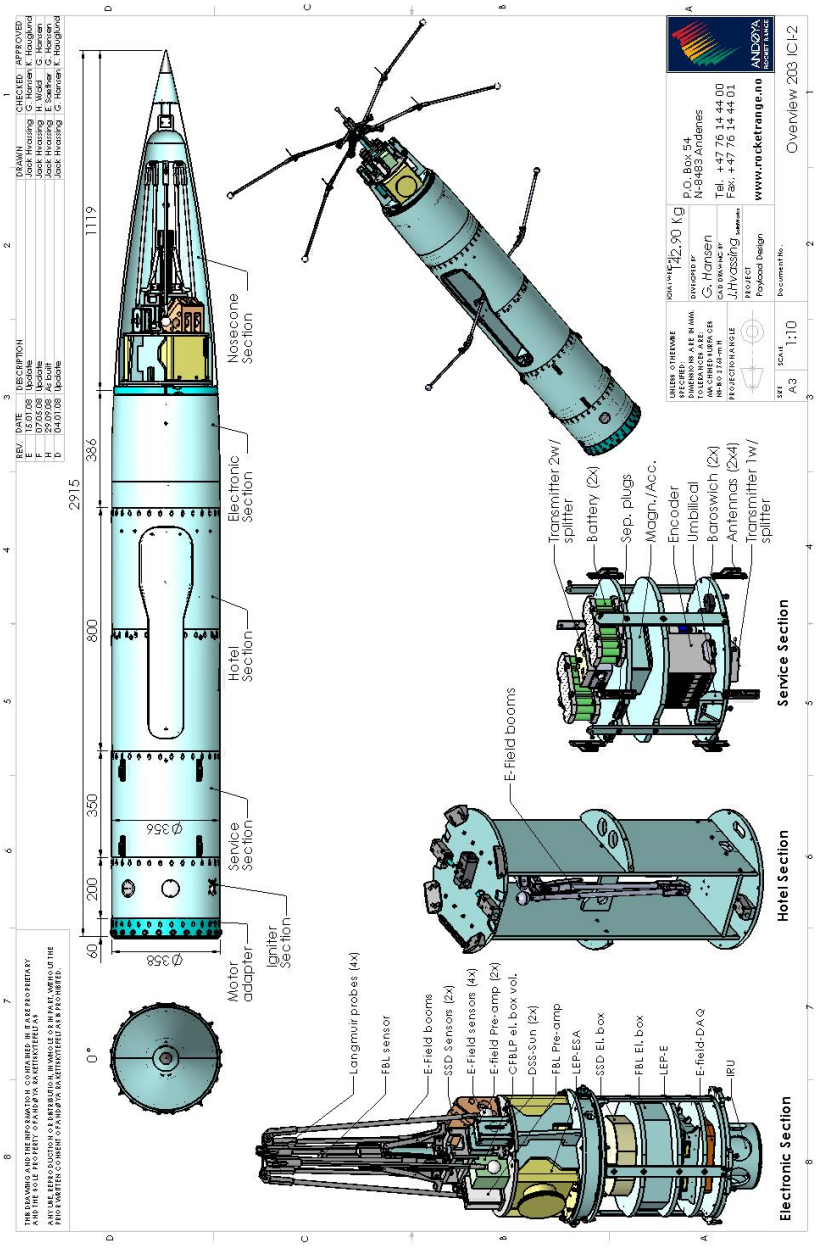

FIGURE 4.5: ICI-2 payload. Image credit: Andøya Space Center.

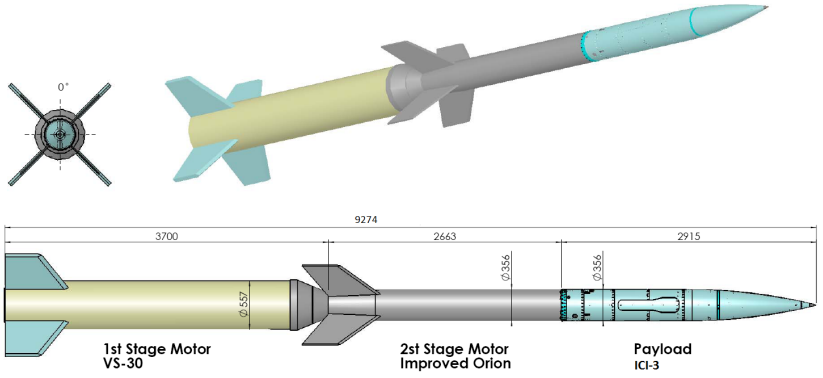

FIGURE 4.6: ICI-2 rocket vehicle. Image credit: Andøya Space Center.

Chapter 5

Summary, discussion and future work

5.1 Summary of results

Paper I:

H. Hoang, L. B. N. Clausen, K. Røed, T. A. Bekkeng, E. Trondsen, B. Lybekk, H. Strøm, D. M. Bang-Hauge, A. Pedersen, A. Spicher and J. I. Moen (2018), The Multi-Needle Langmuir Probe System on Board NorSat-1. *Space Science Reviews*, *214*(75), doi: 10.1007/s11214-018-0509-2.

The first paper presents the m-NLP system developed for the NorSat-1 microsatellite together with some initial results. The m-NLP instrument has four Langmuir probes with 25 mm length and 0.5 mm diameter. The boom system has been designed and deployed when the satellite reaches the orbit, giving a minimum clearance between the probes and the spacecraft platform and other payload equipment of about 15 cm. The probe instrument is capable of measuring the plasma density and spacecraft potential at up to 1kHz sampling rate, thus offering an unprecedented opportunity to continuously resolve ionospheric plasma density structures down to a few meters in LEO. Data collected during the sweep mode show that plasma parameters calculated from the obtained I-V curves are within the expected range, assuming that the ambient plasma is homogeneous over the sweep period. Data in the normal mode, where the m-NLP probes are biased at 3 V, 4 V,

5 V and 6 V, and sampled at 400 Hz, recorded on August 30th, 2017 are reported. The estimated electron density in the auroral zone fluctuated around 5×10^{10} m^{-3} and the NorSat-1 potential varies from -3.5 V to -2.5 V during the measurement period. Just after the satellite left the auroral region and entered the eclipse, all probe currents dropped significantly and recovered shortly thereafter. A possible reason for this behavior could be the sudden lack of emission of photoelectrons due to the absence of sunlight. Further statistical study of this phenomenon is reported in Ivarsen et al. [2018]. The small-scale ionospheric plasma density structures are also observed. These structures lie at the heart of the scientific investigation made possible by the m-NLP onboard NorSat-1. The electron density measured along the NorSat-1 satellite's orbit was compared with that derived from the IRI-2016 model. While there are still some discrepancies, the comparison results indicate quite good agreement between those two approaches. The IRI model is believed to underestimate the electron density in the polar cap/auroral region. Even though the m-NLP instrument has the highest sampling rate of 1 kHz on the NorSat-1 satellite, we used 400 Hz during the first stage of the commissioning phase. Over the coming years, NorSat-1 will cross the equatorial and polar regions twice every 90 minutes, providing a wealth of data that will help to better understand the mechanisms that dissipate energy input from larger spatial scales by creating small-scale plasma density structures within the ionosphere.

Paper II:

H. Hoang, K. Røed, T. A. Bekkeng, J. I. Moen, L. B. N. Clausen, E. Trondsen, B. Lybekk, H. Strøm, D. M. Bang-Hauge and A. Pedersen (2018). The multi-needle Langmuir probe instrument for QB50 mission: Case studies of Ex-Alta 1 and Hoopoe satellites. *Submitted to Space Science Reviews.*

The second paper presents the m-NLP instrument development for the QB50 picosatellites. The m-NLP science unit has been mounted on board eleven QB50 satellites to characterize the ambient plasma. While the instrument has been deployed on many sounding rockets, QB50 and NorSat-1 satellites offer opportunities for the first time to continuously monitor the plasma density in LEO. Due to the limited conductive surface area of the QB50 satellites, the electron emitter has been

included in the m-NLP science unit, that also accommodates four needle Langmuir probe with small diameter of 0.29 mm and length of 25 mm. The full system has been verified in the ESTEC plasma chamber. Mounted on a 2U CubeSat, running the electron emitter at 1.22 V (it was intended to be at 1.20 V but the actual measurement indicates the filament voltage to be 1.22 V) filament voltage helped 'reduce' the CubeSat charging from about −4 V (without the electron emitter) to −3 V when the science unit operated in the swept-bias mode. It is also shown that the CubeSat potential started to be affected by the sweeping probes as long as the biases were higher than 1 V. Although the QB50 mission's scientific goals have not been reached yet and some uncertainties still remain, there are some optimistic in-orbit preliminary results from two QB50 satellites, Ex-Alta 1 and Hoopoe, which could be helpful for the system improvement in future campaigns. Particularly, the electron emitter as part of the m-NLP science unit has demonstrated its capability in the plasma chamber and in orbit to mitigate spacecraft charging effects.

H. Hoang, K. Røed, T. A. Bekkeng, E. Trondsen, L. B. N. Clausen, W. J. Miloch and J. I. Moen (2017). High-spatial-resolution electron density measurement by Langmuir probe for multi-point observations using tiny spacecraft. *Measurement Science and Technology*, *28*(11), doi: 10.1088/1361-6501/aa87e1.

Bekkeng has shown that the m-NLP experiments on many sounding rockets were, to a very large extent, immune to spacecraft charging [Bekkeng, 2017]. However, the measurement capability of the m-NLP system comes at the expense of multiple probe placement, making it not trivial to be deployed in multi-point measurements using such small spacecraft as the ASC daughter payloads where available payload space, power consumption and data link capacity can be even more limited. For example, the space constraint in the daughter payloads would likely give rise to the inter-probe interference due to coupling of the probe sheaths. While the fixed-bias Langmuir probe is mostly used for relative measurements of the electron density, in the third paper, we show that the fixed-bias probe, under some certain conditions, can be used to estimate the absolute ambient plasma density with acceptable errors if the probe bias is set high enough, e.g., 10 V. It should

however be noted that the collected electron current will increase with increasing bias potentials. It will lead to a more negative platform floating potential as a result of keeping the current balance. Generally the probe bias should be selected based on multiple factors such as power consumption, ratio between probe surface area and total conductive area on spacecraft, and expansion of the Debye sheath. The experimental results in the plasma chamber and space with the data from the ICI-2 sounding rocket have demonstrated that the electron density estimation deviation is just around 10 %, compared to the m-NLP system, for a single needle probe biased at 10 V and the spacecraft floating potential of around -2 V. The deviation would be much lower if the platform floating potential is controlled at small negative values. Moreover, detailed analyses on two challenging issues when deploying the DC Langmuir probe on a tiny spacecraft, which are the limited spacecraft conductive area and probe surface contamination, are also presented in the paper. It is shown that small needle probes used in our campaigns not only have small radius compared to Debye lengths in typical ionospheric plasma, making the collected currents approach to the OML currents, but they are also hardly affected by the contamination due to water vapor impurities as they are operating well in the electron saturation region. The single probe technique compared to the m-NLP method still has some disadvantages, i.e., lack of a method to verify probe linearity, and hence the quality check of the data collection, and the platform potential determination capability. However, the presented method can help avoid the inter-probe interference issue, in addition to great advantages of significantly reduced cost, complexity, power consumption, available space, and demanded data-link capacity. Those all are very important factors for multi-point observation applications.

H. Hoang, K. Røed, T. A. Bekkeng, J. I. Moen, A. Spicher, L. B. N. Clausen, W. J. Miloch, E. Trondsen and A. Pedersen (2018). A study of data analysis techniques for the multi-needle Langmuir probe. *Measurement Science and Technology*, *29*(6), doi: 10.1088/1361-6501/aab948.

In the fourth paper, we evaluate and assess two data analysis techniques for the

m-NLP instrument. The first technique uses the linear fitting technique that we commonly use, while the second uses the non-linear fitting technique. It is shown that both techniques have advantages and disadvantages. The linear fitting technique assuming the β value of 0.5 is simple and computationally efficient, and can easily be applied for onboard electron density and spacecraft charging determination, especially for a limited down-link capacity. Since the β parameter might vary, this approach could however result in erroneous electron density estimation of about 20% and 45% if the β parameter is equal to 0.55 and 0.6, respectively, for the case of $eV/k_BT_e = 40$. For the linear fitting technique verification, we have compared the calculated results with other instruments including incoherent scatter radar measurements as well as in-situ instruments. The results are in a satisfactory agreement so far. However, in order to further improve the analysis technique, the probes are required to be longer and cleaned prior to the launch. The non-linear least squares fit can be a good alternative to the linear fit technique since it does not have the above assumption of β. However, the number of data points are limited within the current m-NLP implementation. The non-linear technique accuracy strongly depends on how good the bound constraints and initial estimates of variables are selected. Inaccurate guesses would result in non-negligible erroneous estimate as well. In reality, the measurement data often have some degree of error or random noise within it. Thus, attempting to make the model conform too closely to the limited data set could possibly introduce errors in the model. In order to improve the reliability of this data analysis technique, more deployed probes are needed in future campaigns. Higher bias voltages are additionally required to ensure that all probes operate in the expected electron saturation region. In many space missions, we have observed that the floating potential of rocket payloads and satellites operating in the ionosphere at high geomagnetic latitudes could reach -2.5 V or even more negative, hence the selected biases should be at least 3 V or higher.

5.2 Discussion

The dissertation aims at assessing the m-NLP instrument performance in terms of electron density and spacecraft potential measurements on a variety of space platforms, most of which mainly operate in the high-latitude ionosphere region. Paper I shows that the m-NLP system has demonstrated its capability to continuously resolve small-scale plasma structures as well as to monitor the platform potential on NorSat-1. The discrepancies between the probe measurements are observed in the in-orbit validation of the m-NLP instrument as shown in Figure 7 of Paper I. Since the boom deployment current for only one cassette accommodating Probe 1 and 2 was probably recorded, it is suspected that Probe 3 and 4 of the m-NLP instrument on board NorSat-1 have not been deployed properly (private discussion with Arne Pedersen). Work is still underway to clarify the issue. Besides, we found that the m-NLP system operation is significantly affected by solar cell arrays on board NorSat-1 [Hoang, 2018, Ivarsen et al., 2019]. As a consequence, measurement data in dayside, where the solar power system is active, for many periods should be taken with caution. Coming out of an eclipse, due to the quantity of massive electrons collected by the solar arrays, the spacecraft would charge to a very negative potential causing a significant drop in the probe currents. As the satellite continues traveling along its orbit, the spacecraft potential neutralization process by ions would take place but at a much longer time due to the relatively lower mobility of ions. We suspect that, for some orbits, the spacecraft charging due to the eclipse exit would affect the m-NLP instrument even in the cusp region, in addition to that caused by electron precipitation.

For spacecraft with a smaller surface area ratio such as the QB50 satellites, the miniaturized thermionic electron emitter has been developed and included along with the multiple needle probes. The system has been successfully verified in the plasma chamber as described in Paper II. Without running the electron emitter, the CubeSat floating potential was at most -4 V when the probes were all biased at 10 V. As the probes are operating in the electron saturation region, the electron density and floating potential determination are independent from the spacecraft potential, however, it should be kept in mind that the highly negative potential

leads to sheath expansion, possibly affecting the current collections on the needle probes since they are just about 15 cm away from the platform. As a consequence, the instrument could underestimate the ambient electron density. Running the electron emitter at 1.22V filament voltage helped 'reduce' the CubeSat charging level to −3 V. With higher filament voltages, the CubeSat potential is expected to be even 'lower'. It is noted that the situation where the probes are all biased at 10 V is an extreme case. The CubeSat potential could be less negative for the m-NLP probes biased at smaller positive voltages. Since the spacecraft attitude data are not available yet, it is not trivial to understand what happened to the m-NLP system as there are anomalies in the collected currents. It remains unclear whether or not the probe deployments were successful. There are some remarks to be made about this campaign. First, with their really small diameter, the m-NLP probes are delicate and vulnerable to any vibration or shock during the delivery and launch process, which could possibly affect the probe surface uniformity. Second, while the great advantage of the m-NLP instrument is the ability to resolve plasma density with high resolution, due to the relatively low down-link capacity of the QB50 mission, the m-NLP sampling rate has been set at a very low level. Last but not least, in order to interpret the m-NLP data, accurate spacecraft attitude information is needed and this has not been achieved yet in the mission. Moving forward, spacecraft bus and boom design changes should be considered for the optimal m-NLP science unit deployment. Although the electron emitter is included in the unit, increasing the minimum conductive surface area of the spacecraft to be on the order of 200 – 300 cm^2 is recommended in order to effectively operate the electron emitter, which balances the electron current collected by the m-NLP probes. In addition, the boom system design can be adjusted so that the m-NLP probes are similarly oriented with respect to the magnetic field in order to mitigate likely impacts of a bi-Maxwellian plasma. Furthermore, the limited data amount does not permit whether the solar power systems on board the QB50 satellites have negative impacts on the probe performance.

Even though the total conductive area of the ASC daughter payload is comparable to that of the QB50 CubeSats, its volume is much smaller. Thus it is vulnerable to deploy the m-NLP system on board the ASC payload due to the risk of inter-probe

sheath coupling. A possible solution to this issue presented in Paper III is using a single needle probe with high bias. This could give an absolute electron density estimate within 10 % of the calculated density by the m-NLP instrument, which is believed to be immune to the spacecraft charging, if the spacecraft is not charged to a more negative potential than -2 V. The needle probe as small as the m-NLP probes (typically 0.51 mm in diameter and 25 mm in length) is hardly affected by the contamination due to water vapor impurities as it is operating in the electron saturation region.

Additionally, two data analysis techniques, i.e., linear and non-linear fits, for the m-NLP instrument have been studied using data from the ICI-2 sounding rocket. The two approaches of estimating the electron density have advantages and disadvantages with respect to the current m-NLP implementation, and both can be applied to derive the plasma parameters as discussed in Paper IV. The m-NLP probes are recommended to be longer and cleaned prior to launch to improve the instrument performance. As can be seen from Figure 7 of Paper IV and Figure 3.3 in this thesis, as long as the needle probes operate in the expected electron saturation region, contamination impacts on the probes performance are negligible. This agrees with our simulation analysis in Paper I. Cleaning the probes could, however, help reduce the necessary voltage of the probe bias over the plasma potential in order for them not to be affected by the contamination. The probe cleaning would be helpful, for example, in a case where a single probe is biased at a small fixed voltage for relative density measurements on a tiny space platform without using the electron emitter. Making the probes longer can also improve the probe performance; however, the spacecraft-to-probe-surface-area ratio should be taken into account, especially for the small space platforms.

5.3 Future work

The following are some of research areas I would like to continue in the future.

Multi-point electron density measurements with the ASC daughter payloads

The multi-point electron density measurements using the ASC daughter payloads would be able to provide more insights about plasma dynamics, i.e., the separation of temporal and spatial variations in electron density, which cannot be achieved with the measurement at a single location. Since the electron density measurement on such small payloads is very challenging, more efforts needs to be put into, e.g., spacecraft charging mitigation solutions, and the probe and boom system design.

The 4DSpace experiment deck has been integrated to a NASA sounding rocket, which was launched from Andøya Space Center on January, 2019. Experiences gained from the experiment will be precious for the next campaign of ICI-5, planned for December, 2019.

Multi-instrument measurements of the spacecraft potential fluctuations
For a more consistent determination of the spacecraft floating potential, multi-instrument measurements are needed. On the series of the ICI sounding rockets, the spacecraft floating potential fluctuations can be estimated using an electric field double-probe instrument (E-field instrument) in addition to the m-NLP instrument. The electric field instrument was deployed to measure low frequency and quasi-static electric field associated with the production of sub-meter scale HF radar backscatter-related irregularities in high latitude upper atmosphere of the Earth [Spicher et al., 2016]. The instrument is comprised of two identical pairs of spherical sensors with conducting surface attached at the end of two orthogonal booms radially deployed from the spinning rockets. In addition to the voltage difference signals measured between two probes in each pair, potential signals of the single probe sensors with respect to the rocket payload potential are examined.

First results indicate a good agreement between the two different instruments in estimating the payload charging issue as shown in Figure 5.1, where the payload potential of ICI-3, which was launched from Ny-Ålesund, Svalbard on December 3rd, 2011 is given. The floating potential fluctuations measured by the electric field instrument (two single probes SP1 and SP2 are used) are normalized to the m-NLP. When summing up the data from the two single probes of the electric field instrument, the measured electric fields between them and the rocket body

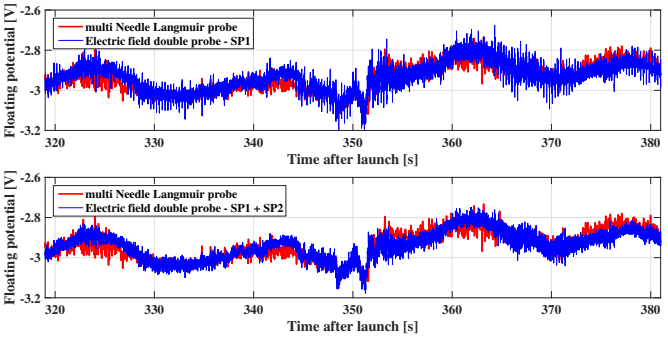

FIGURE 5.1: Payload floating potential of ICI-3 as a function of time. Floating potential fluctuations measured by electric field instrument are normalized to the m-NLP to have absolute payload potentials. SP1 and SP2 are single-probe channel of probe 1 and probe 2.

are canceled reducing the 'spikes' in the calculated floating potential compared to the floating potential estimated by the single probe SP1.

Moreover, it is interesting that the voltage differences between the probes of the E-field instrument and the rocket payload, i.e., SP1, SP2, are just about 50 mV. That means the electric field probes and the rocket payload came to very similar floating potentials. As the floating potentials are estimated to be roughly -3 V as shown in Figure 5.1, it might be that the relatively large negative floating potentials are caused by heated electron population in the cusp region. Works are in progress to study the issue.

Probe fabrication

As previously mentioned, in order to mitigate edge effects, the m-NLP probes are planed to be made longer and/or two guards/bootstrapped sections are inserted at the two ends of each probe. The probe diameter is considered to be chosen bigger so as to facilitate the probe fabrication with the two ended bootstrapped supports. Such probes can be deployed for sounding rocket applications. However, for tiny spacecraft, increasing the probe dimensions would significantly reduce the spacecraft to probe surface area ratio, thus degrading the measurement performance. More efforts need to be put into, e.g. spacecraft charging mitigation solutions. A feasible option is to include the electron emitter.

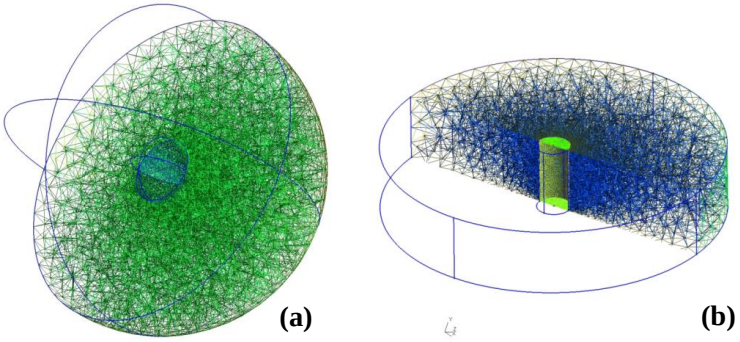

FIGURE 5.2: Unstructured meshes of conductive sphere (a) and cylinder (b) used in SPIS.

Probe to plasma coupling modeling

There is an approach of Particle-In-Cell (PIC) which also provides a tool to compute the distribution of the current collected by a spherical or cylindrical probe. While Laframboise's method considers the phase space as a continuum, the PIC approach discretizes the phase space by representing the charge distribution as discrete particles. One of the most popular tools with the PIC approach for plasma simulations is the Spacecraft Plasma Interaction System (SPIS) software, which has been developed under European Space Agency (ESA) contract with a consortium including ONERA/DESP, Artenum and University Paris VII since 2002. The SPIS open-source code models the plasma particles as macro particles, instead of the level of individual electrons and ions which would require much computation power [Hilgers et al., 2008, Roussel et al., 2008].

Our first modeling trial is to simulate ideal cases of spherical and cylindrical Langmuir probe modeling using SPIS. Unstructured meshes of conductive sphere and cylinder are shown in Figure 5.2(a) and (b), respectively. The results show that the current collections are closely matched to the OML currents. Work is in progress to model the probes with more complicated structures as well as the coupling between the probes, the spacecraft and the plasma. This would give a better understanding of how the probe current collections are affected by plasma wakes and spacecraft sheath expansion.

Electron energy distribution measurement

It is possible to improve the connection between the E-field probes and their local

plasmas by a positive current bias to the probes (private discussion with Arne Pedersen), as demonstrated by Fahleson et al. [1974]. This will shift the potentials of the probes closer to the plasma potential and reduce the sheath resistance values, which in turn gives a better coupling between the probes and their local plasma potentials. The positive bias currents to the probes are supposed to be monitored in order not to drive the rocket payload potential more negative, because these currents would allow a larger share of the more energetic part of the electron population to come to the rocket payload. Model calculations are required for determining good bias current values.

We let each probe of one probe pair of the E-field instrument have the same fixed bias current. The other pair can start with no bias current to the two probes and then increase the bias current to these probes to detect whether a negative shift in the rocket payload potential measured by the m-NLP instrument (probably due to heated electron population). The measurements of the probe to rocket payload potentials of the latter two probes will provide the form of the electron current versus the potentials of the E-field probes, which will contain information about the electron energy distribution. The electric field will be measured in parallel with the bias current sweep.

Bibliography

Amemiya, H. and Fuchs, G. (1991). Range of application for asymmetric double probes. *Japanese Journal of Applied Physics*, 30(12R):3531.

Anderson, D., Fuller-Rowell, T., and (U.S.), S. E. C. (1999). *The ionosphere*. Space environment topics. Space Environment Center.

Barjatya, A., Swenson, C. M., Thompson, D. C., and Jr., K. H. W. (2009). Invited article: Data analysis of the floating potential measurement unit aboard the international space station. *Review of Scientific Instruments*, 80(4):041301.

Basu, S. and Basu, S. (1981). Equatorial scintillations-a review. *Journal of Atmospheric and Terrestrial Physics*, 43(5):473 – 489. Equatorial Aeronomy - I.

Basu, S., Basu, S., MacKenzie, E., Coley, W. R., Sharber, J. R., and Hoegy, W. R. (1990). Plasma structuring by the gradient drift instability at high latitudes and comparison with velocity shear driven processes. *Journal of Geophysical Research: Space Physics*, 95(A6):7799–7818.

Basu, S., MacKenzie, E., and Basu, S. (1988). Ionospheric constraints on vhf/uhf communications links during solar maximum and minimum periods. *Radio Science*, 23(03):363–378.

Basu, S., Weber, E. J., Bullett, T. W., Keskinen, M. J., MacKenzie, E., Doherty, P., Sheehan, R., Kuenzler, H., Ning, P., and Bongiolatti, J. (1998). Characteristics of plasma structuring in the cusp/cleft region at svalbard. *Radio Science*, 33(6):1885–1899.

Bekkeng, T. A. (2017). *Development of a miniaturized multi-Needle Langmuir Probe system for in-situ measurements of electron density and spacecraft floating potential*. PhD thesis, University of Oslo.

Bekkeng, T. A., Barjatya, A., Hoppe, U.-P., Pedersen, A., Moen, J. I., Friedrich, M., and Rapp, M. (2013). Payload charging events in the mesosphere and their impact on langmuir type electric probes. *Annales Geophysicae*, 31(2):187–196.

Bekkeng, T. A., Helgeby, E. S., Pedersen, A., Trondsen, E., Lindem, T., and Moen, J. I. (2017). multi-needle langmuir probe system for electron density measurements and active spacecraft potential control on cubesats. Submitted to IEEE Transactions on Aerospace and Electronic Systems.

Bekkeng, T. A., Jacobsen, K. S., Bekkeng, J. K., Pedersen, A., Lindem, T., Lebreton, J.-P., and Moen, J. I. (2010). Design of a multi-needle langmuir probe system. *Measurement Science and Technology*, 21(8):085903.

Bernstein, I. B. and Rabinowitz, I. N. (1959). Theory of electrostatic probes in a low-density plasma. *Physics of Fluids*.

Bilitza, D., Altadill, D., Truhlik, V., Shubin, V., Galkin, I., Reinisch, B., and Huang, X. (2017). International reference ionosphere 2016: From ionospheric climate to real-time weather predictions. *Space Weather*, 15(2):418–429. 2016SW001593.

Bilitza, D., Altadill, D., Zhang, Y., Mertens, C., Truhlik, V., Richards, P., McKinnell, L.-A., and Reinisch, B. (2014). The international reference ionosphere 2012 - a model of international collaboration. *Journal of Space Weather and Space Climate*, 4:A07.

Bilitza, D. and Reinisch, B. (2008). International reference ionosphere 2007: Improvements and new parameters. *Advances in Space Research*, 42(4):599 – 609.

Boggess, R. L., Brace, L. H., and Spencer, N. W. (1959). Langmuir probe measurements in the ionosphere. *Journal of Geophysical Research*, 64(10):1627–1630.

Brace, L. H. (1998). *Langmuir Probe Measurements in the Ionosphere, in Measurement Techniques in Space Plasmas:Particles*. American Geophysical Union.

Brace, L. H., Theis, R. F., and Dalgarno, A. (1973). The cylindrical electrostatic probes for atmosphere explorer -c,-d, and -e. *Radio Science*, 8(4):341–348.

Buchau, J., Reinisch, B. W., Weber, E. J., and Moore, J. G. (1983). Structure and dynamics of the winter polar cap f region. *Radio Science*, 18(06):995–1010.

Chapkunov, S. K., Ivanova, T. N., Petrunova, M. K., and Serafimov, K. B. (1976). Measurement of electron and ion density and temperature on the intercosmos 12 satellite. In *Space research XVI; Proceedings of the Open Meetings of Working Groups on Physical Sciences*, pages 423–425.

Chen, F. F. (2003). Lecture notes on langmuir probe diagnostics. In *EEE-ICOPS Meeting*.

Chiaretta, M. (2011). Numerical modelling of langmuir probe measurements for the swarm spacecraft. Master's thesis, Uppsala University.

Clausen, L. B. N., Moen, J. I., Hosokawa, K., and Holmes, J. M. (2016). Gps scintillations in the high latitudes during periods of dayside and nightside reconnection. *Journal of Geophysical Research: Space Physics*, 121(4):3293–3309. 2015JA022199.

Fahleson, U., Fälthammar, C.-G., and Pedersen, A. (1974). Ionospheric temperature and density measurements by means of spherical double probes. *Planetary and Space Science*, 22(1):41 – 66.

Fisher, L. E., Lynch, K. A., Fernandes, P. A., Bekkeng, T. A., Moen, J., Zettergren, M., Miceli, R. J., Powell, S., Lessard, M. R., and Horak, P. (2016). Including sheath effects in the interpretation of planar retarding potential analyzerś low-energy ion data. *Review of Scientific Instruments*, 87(4):043504.

Gondarenko, N. A. and Guzdar, P. N. (2004a). Density and electric field fluctuations associated with the gradient drift instability in the high-latitude ionosphere. *Geophysical Research Letters*, 31(11):n/a–n/a. L11802.

Gondarenko, N. A. and Guzdar, P. N. (2004b). Plasma patch structuring by the nonlinear evolution of the gradient drift instability in the high-latitude ionosphere. *Journal of Geophysical Research: Space Physics*, 109(A9):n/a–n/a. A09301.

Gondarenko, N. A. and Guzdar, P. N. (2006). Simulations of the scintillation-producing irregularities in high-latitude plasma patches. *Geophysical Research Letters*, 33(22):n/a–n/a. L22107.

Goodwin, L. V., Iserhienrhien, B., Miles, D. M., Patra, S., van der Meeren, C., Buchert, S. C., Burchill, J. K., Clausen, L. B. N., Knudsen, D. J., McWilliams, K. A., and Moen, J. (2015). Swarm in situ observations of f region polar cap patches created by cusp precipitation. *Geophysical Research Letters*, 42(4):996–1003. 2014GL062610.

Hey, J. S., Parsons, S. J., and Phillips, J. W. (1946). Fluctuations in cosmic radiation at radio-frequencies. *Nature*, 158:234–234.

Hilgers, A., Clucas, S., Thiebault, B., Roussel, J. F., Mateo-Velez, J. C., Forest, J., and Rodgers, D. (2008). Modeling of plasma probe interactions with a pic code using an unstructured mesh. *IEEE Transactions on Plasma Science*, 36(5):2319–2323.

Hoang, H. (2018). Commissioning the multi-needle langmuir probe instrument on board norsat-1. Technical report to Norwegian Space Center.

Hoang, H., Røed, K., Bekkeng, T. A., Moen, J. I., Clausen, L. B. N., Trondsen, E., Lybekk, B., Strøm, H., Bang-Hauge, D. M., and Pedersen, A. (2018). The multi-needle langmuir probe instrument for qb50 mission: Case studies of ex-alta 1 and hoopoe satellites. Unpublished paper.

Hoang, H., Røed, K., Bekkeng, T. A., Trondsen, E., Clausen, L. B. N., Miloch, W. J., and Moen, J. I. (2017). High spatial-resolution electron density measurement by langmuir probe for multi-point observations using tiny spacecraft. *Measurement Science and Technology*.

Huba, J. D., Joyce, G., and Krall, J. (2008). Three-dimensional equatorial spread f modeling. *Geophysical Research Letters*, 35(10):n/a–n/a. L10102.

Hysell, D. L., Hedden, R. B., Chau, J. L., Galindo, F. R., Roddy, P. A., and Pfaff, R. F. (2009). Comparing f region ionospheric irregularity observations from c/nofs and jicamarca. *Geophysical Research Letters*, 36(18):n/a–n/a. L00C01.

Hysell, D. L., Milla, M. A., Condori, L., and Vierinen, J. (2015). Data-driven numerical simulations of equatorial spread f in the peruvian sector 3: Solstice. *Journal of Geophysical Research: Space Physics*, 120(12):10,809–10,822. 2015JA021877.

Ivarsen, M. F., Hoang, H., Yang, L., Clausen, L. B. N., Spicher, A., Jin, Y., Trondsen, E., Moen, J. I., Red, K., and Lybekk, B. (2019). Multineedle langmuir probe operation and acute probe current susceptibility to spacecraft potential. *IEEE Transactions on Plasma Science*, 47(8):3816–3823.

Ivarsen, M. F., Hoang, H., Yang, L., Trondsen, E., Clausen, L. B. N., Spicher, A., Lybekk, B., and Moen, J. I. (2018). Multi-needle langmuir probe operation and acute probe current susceptibility to spacecraft potential. In *15th Spacecraft Charging Technology Conference (SCTC)*.

Iwata, M., Khan, A. R., Igawa, H., Toyoda, K., Cho, M., and Fujita, T. (2012). Development of electron-emitting film for spacecraft charging mitigation. *Journal of Spacecraft and Rockets*, 49(3):546–552.

Jacobsen, K. S., Pedersen, A., Moen, J. I., and Bekkeng, T. A. (2010). A new langmuir probe concept for rapid sampling of space plasma electron density. *Measurement Science and Technology*, 21(8):085902.

Jin, Y., Moen, J. I., and Miloch, W. J. (2014). Gps scintillation effects associated with polar cap patches and substorm auroral activity: direct comparison. *Journal of Space Weather Space Climate*, 4.

Jin, Y., Moen, J. I., and Miloch, W. J. (2015). On the collocation of the cusp aurora and the gps phase scintillation: A statistical study. *Journal of Geophysical Research: Space Physics*, 120(10):9176–9191. 2015JA021449.

Jin, Y., Moen, J. I., Miloch, W. J., Clausen, L. B. N., and Oksavik, K. (2016). Statistical study of the gnss phase scintillation associated with two types of auroral blobs. *Journal of Geophysical Research: Space Physics*, 121(5):4679–4697. 2016JA022613.

Kintner, P. M. and Seyler, C. E. (1985). The status of observations and theory of high latitude ionospheric and magnetospheric plasma turbulence. *Space Science Reviews*, 41(1):91–129.

Laframboise, J. G. (1966). Theory of spherical and cylindrical langmuir probes in a collisionless maxwellian plasma at rest. Report no. 100, University of Toronto Institute for Aerospace Studies.

Lebreton, J.-P., Stverak, S., Travnicek, P., Maksimovic, M., Klinge, D., Merikallio, S., Lagoutte, D., Poirier, B., Blelly, P.-L., Kozacek, Z., and Salaquarda, M. (2006). The isl langmuir probe experiment processing onboard demeter: Scientific objectives, description and first results. *Planetary and Space Science*, 54(5):472 – 486. First Results of the DEMETER Micro-Satellite.

Lindahl, G. (2015). New payload module for 4d measurements. In *22nd ESA Symposium on European Rocket and Balloon programmes and related research.*

Lorentzen, D. A., Moen, J., Oksavik, K., Sigernes, F., Saito, Y., and Johnsen, M. G. (2010). In situ measurement of a newly created polar cap patch. *Journal of Geophysical Research: Space Physics*, 115(A12):n/a–n/a. A12323.

Luhmann, J. G. (1995). *Ionospheres*, chapter 7, pages 183–226. Cambridge University Press.

Lynch, K. A., Hampton, D. L., Zettergren, M., Bekkeng, T. A., Conde, M., Fernandes, P. A., Horak, P., Lessard, M., Miceli, R., Michell, R., Moen, J., Nicolls, M., Powell, S. P., and Samara, M. (2015). Mica sounding rocket observations of conductivity-gradient-generated auroral ionospheric responses: Small-scale structure with large-scale drivers. *Journal of Geophysical Research: Space Physics*, 120(11):9661–9682. 2014JA020860.

McEwen, D. J. and Harris, D. P. (1996). Occurrence patterns of f layer patches over the north magnetic pole. *Radio Science*, 31(3):619–628.

Miles, D. M., Bennest, J. R., Mann, I. R., and Millling, D. K. (2013). A radiation hardened digital fluxgate magnetometer for space applications. *Geoscientific Instrumentation, Methods and Data Systems*, 2(2):213–224.

Miles, D. M., Mann, I. R., Ciurzynski, M., Barona, D., Narod, B. B., Bennest, J. R., Pakhotin, I. P., Kale, A., Bruner, B., Nokes, C. D. A., Cupido, C., Haluza-DeLay, T., Elliott, D. G., and Milling, D. K. (2016). A miniature, low-power scientific fluxgate magnetometer: A stepping-stone to cube-satellite constellation missions. *Journal of Geophysical Research: Space Physics*, 121(12):11,839–11,860. 2016JA023147.

Moen, J., Gulbrandsen, N., Lorentzen, D. A., and Carlson, H. C. (2007). On the mlt distribution of f region polar cap patches at night. *Geophysical Research Letters*, 34(14):n/a–n/a. L14113.

Moen, J., Hosokawa, K., Gulbrandsen, N., and Clausen, L. B. N. (2015). On the symmetry of ionospheric polar cap patch exits around magnetic midnight. *Journal of Geophysical Research: Space Physics*, 120(9):7785–7797. 2014JA020914.

Moen, J., Oksavik, K., Abe, T., Lester, M., Saito, Y., Bekkeng, T. A., and Jacobsen, K. S. (2012). First in-situ measurements of hf radar echoing targets. *Geophysical Research Letters*, 39(7):n/a–n/a. L07104.

Moen, J., Oksavik, K., Alfonsi, L., Daabakk, Y., Romano, V., and Spogli, L. (2013). Space weather challenges of the polar cap ionosphere. *Journal of Space Weather and Space Climate*.

Moen, J., Walker, I. K., Kersley, L., and Milan, S. E. (2002). On the generation of cusp hf backscatter irregularities. *Journal of Geophysical Research: Space Physics*, 107(A4):SIA 3–1–SIA 3–5.

Mott-Smith, H. M. and Langmuir, I. (1926). The theory of collectors in gaseous discharges. *Physical Review*, 28:727–763.

Muylaert, J., Reinhard, R., Asma, C., and Danilkin, V. (2009). Qb50, an international network of 50 cubesats for multi-point, in-situ measurements in the lower thermosphere and re-entry research. In *QB50 Workshop*.

Oksavik, K., Barth, V. L., Moen, J., and Lester, M. (2010). On the entry and transit of high-density plasma across the polar cap. *Journal of Geophysical Research: Space Physics*, 115(A12):n/a–n/a. A12308.

Oyama, K. I. (1976). A systematic investigation of several phenomena associated with contaminated langmuir probes. *Planetary and Space Science*, 24(2):183 – 190.

Oyama, K.-I., Lee, C. H., Fang, H. K., and Cheng, C. Z. (2012). Means to remove electrode contamination effect of langmuir probe measurement in space. *Review of Scientific Instruments*, 83(5):055113.

Piel, A., Hirt, M., and Steigies, C. T. (2001). Plasma diagnostics with langmuir probes in the equatorial ionosphere: I. the influence of surface contamination. *Journal of Physics D: Applied Physics*, 34(17):2643.

Rich, F. J. and Basu, S. (1985). *Ionospheric Physics*, chapter 9. Air Force Geophysics Laboratory.

Rino, C. L. (1979). A power law phase screen model for ionospheric scintillation: 1. weak scatter. *Radio Science*, 14(6):1135–1145.

Rodrigues, F. S., Kelley, M. C., Roddy, P. A., Hunton, D. E., Pfaff, R. F., de La Beaujardière, O., and Bust, G. S. (2009). C/nofs observations of intermediate and transitional scale-size equatorial spread f irregularities. *Geophysical Research Letters*, 36(18):n/a–n/a. L00C05.

Roussel, J. F., Rogier, F., Dufour, G., Mateo-Velez, J. C., Forest, J., Hilgers, A., Rodgers, D., Girard, L., and Payan, D. (2008). Spis open-source code: Methods, capabilities, achievements, and prospects. *IEEE Transactions on Plasma Science*, 36(5):2360–2368.

Sanmartin, J. R. and Estes, R. D. (1999). The orbital-motion-limited regime of cylindrical langmuir probes. *Physics of Plasmas*, 6(1):395–405.

Scheiner, B., Baalrud, S. D., Yee, B. T., Hopkins, M. M., and Barnat, E. V. (2015). Theory of the electron sheath and presheath. *Physics of Plasmas*, 22(12):123520.

Schunk, R. W. and Nagy, A. F. (2000). *Ionospheres: Physics, Plasma Physics, and Chemistry*. Cambridge University Press.

Simon, A. (1963). Instability of a partially ionized plasma in crossed electric and magnetic fields. *The Physics of Fluids*, 6(3):382–388.

Spicher, A., Cameron, T., Grono, E. M., Yakymenko, K. N., Buchert, S. C., Clausen, L. B. N., Knudsen, D. J., McWilliams, K. A., and Moen, J. I. (2015). Observation of polar cap patches and calculation of gradient drift instability growth times: A swarm case study. *Geophysical Research Letters*, 42(2):201–206. 2014GL062590.

Spicher, A., Ilyasov, A. A., Miloch, W. J., Chernyshov, A. A., Clausen, L. B. N., Moen, J. I., Abe, T., and Saito, Y. (2016). Reverse flow events and small-scale effects in the cusp ionosphere. *Journal of Geophysical Research: Space Physics*, 121(10):10,466–10,480. 2016JA022999.

Steigies, C. T. and Barjatya, A. (2012). Contamination effects on fixed-bias langmuir probes. *Review of Scientific Instruments*, 83(11):113502.

Suresh, P. (2011). Surface morphology implications on langmuir probe measurements. Master's thesis, Utah State University.

Tsunoda, R. T. (1988). High-latitude f region irregularities: A review and synthesis. *Reviews of Geophysics*, 26(4):719–760.

Walter, B., Levesque, P.-L., Kopp, G., Andersen, B., Beck, I., Finsterle, W., Gyo, M., Heuerman, K., Koller, S., Mingard, N., Oliva, A. R., Pfiffner, D., Soder, R., Spescha, M., Suter, M., and Schmutz, W. (2017). The clara/norsat-1 solar absolute radiometer: instrument design, characterization and calibration. *Metrologia*, 54(5):674.

Weber, E. J., Buchau, J., Moore, J. G., Sharber, J. R., Livingston, R. C., Winningham, J. D., and Reinisch, B. W. (1984). F layer ionization patches in the polar cap. *Journal of Geophysical Research: Space Physics*, 89(A3):1683–1694.

Woodman, R. F. (2009). Spread f - an old equatorial aeronomy problem finally resolved? *Annales Geophysicae*, 27(5):1915–1934.

Woodman, R. F. and La Hoz, C. (1976). Radar observations of f region equatorial irregularities. *Journal of Geophysical Research*, 81(31):5447–5466.

Zhang, Q.-H., Lockwood, M., Foster, J. C., Zhang, S.-R., Zhang, B.-C., McCrea, I. W., Moen, J., Lester, M., and Ruohoniemi, J. M. (2015). Direct observations

of the full dungey convection cycle in the polar ionosphere for southward interplanetary magnetic field conditions. *Journal of Geophysical Research: Space Physics*, 120(6):4519–4530. 2015JA021172.

This dissertation was written using Sharelatex (www.sharelatex.com) and is based on the template by Steve Gunn.

Paper I

The Multi-Needle Langmuir Probe System on Board NorSat-1

H. Hoang, L. B. N. Clausen, K. Røed, T. A. Bekkeng, E. Trondsen, B. Lybekk, H. Strøm, D. M. Bang-Hauge, A. Pedersen, A. Spicher and J. I. Moen

(2018)

Space Science Reviews, *214*(75)

doi: 10.1007/s11214-018-0509-2.

Space Sci Rev (2018) 214:75
https://doi.org/10.1007/s11214-018-0509-2

The Multi-Needle Langmuir Probe System on Board NorSat-1

H. Hoang[1] · L.B.N. Clausen[1] · K. Røed[1] · T.A. Bekkeng[1] · E. Trondsen[1] · B. Lybekk[1] · H. Strøm[1] · D.M. Bang-Hauge[1] · A. Pedersen[1] · A. Spicher[1] · J.I. Moen[1]

Received: 3 November 2017 / Accepted: 27 April 2018

Abstract On July 14th, 2017, the first Norwegian scientific satellite NorSat-1 was launched into a high-inclination (98°), low-Earth orbit (600 km altitude) from Baikonur, Kazakhstan. As part of the payload package, NorSat-1 carries the multi-needle Langmuir probe (m-NLP) instrument which is capable of sampling the electron density at a rate up to 1 kHz, thus offering an unprecedented opportunity to continuously resolve ionospheric plasma density structures down to a few meters. Over the coming years, NorSat-1 will cross the equatorial and polar regions twice every 90 minutes, providing a wealth of data that will help to better understand the mechanisms that dissipate energy input from larger spatial scales by creating small-scale plasma density structures within the ionosphere. In this paper we describe the m-NLP system on board NorSat-1 and present some first results from the instrument commissioning phase. We show that the m-NLP instrument performs as expected and highlight its unique capabilities at resolving small-scale ionospheric plasma density structures.

Keywords Ionospheric plasma density · High resolution · Langmuir probe · Polar orbit

1 Introduction

Due to solar extreme ultraviolet (EUV) radiation the upper terrestrial atmosphere is partly ionized. This part of the atmosphere is called the ionosphere and is, due to energy input from even higher altitudes, often structured across a multitude of spatial scales (e.g. Kintner and Seyler 1985). Generally, ionospheric plasma structuring is poorly understood. At high latitudes the general consensus seems to be that as regions of high-plasma density, so-called polar cap patches which are created near the dayside cusp region, drift across the polar cap driven by ionospheric convection (Buchau et al. 1983; McEwen and Harris 1996; Moen et al. 2007, 2015; Oksavik et al. 2010; Zhang et al. 2015), their trailing edges provides favorable conditions for the growth of a macroscopic plasma instability called the gradient drift instability (GDI) (Simon 1963; Tsunoda 1988). As this instability breaks up the drifting

H. Hoang
huy.hoang@fys.uio.no

1 Department of Physics, University of Oslo, 0316 Oslo, Norway

Published online: 08 May 2018

plasma density gradient associated with the polar cap patch (Weber et al. 1984; Basu et al. 1990; Gondarenko and Guzdar 2004b), it creates plasma density structures on a variety of spatial scales ranging from kilometers down to meters (Gondarenko and Guzdar 2004a, 2006). These plasma density structures can then, if they are large in amplitude, introduce scintillations onto trans-ionospheric radio signals (e.g., Rino 1979). Contrast this knowledge with a large statistical study that finds no evidence for enhanced scintillation levels inside the polar cap at Global Navigation Satellite Systems (GNSS) frequencies, even when there is clear evidence of polar cap patches as shown in Clausen et al. (2016). In the European Arctic sector, enhanced GNSS scintillation levels are attributed to high TEC levels in the auroral oval, at day and night (Jin et al. 2014, 2015, 2016).

Our knowledge about plasma structuring in the equatorial region is slightly better. Equatorial spread F (ESF) (Woodman and La Hoz 1976) is now understood to be a consequence of the generalized Rayleigh-Taylor (GTR) instability acting on the edges of rising "bubbles" of low plasma density. Most of the large-scale ionospheric plasma models for ESF deal with fluid-like or hybrid approaches, where the dynamics of the ionospheric plasma or some of its species are treated as continuum describing macroscopic (bulk) properties of the plasma species (e.g., Huba et al. 2008). Such an approach has recently been successful in describing plasma dynamics and formation of ESF in the low-latitude ionosphere; in fact, with initial parameters from radars, these models can now predict the general evolution of ESF (Hysell et al. 2015). However, these models omit kinetic effects linking the results to the smallest scales that can only be constrained by measurements at meter-scale resolution. There are still important open questions regarding the link across scale sizes, e.g., by what mechanism energy cascades from larger (10–100 kilometer) to smaller (10's of meters) scales and what initiates the instability (Woodman 2009). It is also unclear whether meter-scale irregularities are really just drifting passively with the background plasma as has been commonly assumed (Hysell et al. 2009). Furthermore, we are lacking a comprehensive understanding of the day-to-day variability in the ESF occurrence. Also, the average spatial distribution of the small-scale density irregularities associated with this phenomenon is hitherto largely unknown (Rodrigues et al. 2009).

Essentially all our knowledge about ionospheric plasma density structures with scale sizes of a few tens to hundreds of meters was derived from indirect measurements. It was shown, for example, that electromagnetic signals received on the ground frequently contains fluctuations in amplitude and phase, so-called scintillations (Hey et al. 1946). These are imposed on the signal as the wave travels through an ionosphere that contained plasma density irregularities. These irregularities would locally alter the refractive index and therefore cause minute differences in the travel time for selected parts of the wave front, combining to cause sometimes significant signal distortions. It was hypothesized that plasma density structures at scale sizes around the Fresnel scale, i.e. a few hundred meters for typical frequencies used for GNSS, are most effective in causing signal scintillations.

In the last 50 years, sounding rocket instruments overcame the usual bandwidth limitations of satellites and provided plasma density measurements with sub-km resolution in the polar and equatorial region (e.g. Kelley et al. 1982; LaBelle et al. 1986; Hysell et al. 1994; Spicher et al. 2014, and references herein). However, these studies can only speak to the specific situation during the rocket flight lasting a few minutes, and allow only a limited outlook towards the average picture of ionospheric structuring. Since continuous in situ measurements with sufficient resolution to resolve plasma density irregularities with a size of a few meters were not available, much of our knowledge about small-scale ionospheric structuring is therefore based on the analysis of signals received on the ground. While from a standpoint of applied science such studies give an overview of the spatial distribution of the

regions where signal distortions for different satellite systems can be expected, they provide only limited insight into the physical processes that cause them.

Previous high-resolution in situ exploration of the plasma density at equatorial latitudes has mainly been realized with rockets (Kelley et al. 1982; LaBelle et al. 1986). Since the magnetic field at the equator is horizontal (essentially aligned North-South), a vertical rocket flight cuts through the vertically stratified ionosphere in the same manner as a satellite crossing high-latitude magnetic field lines. The studies mentioned above show that the spectrum of small-scale plasma density fluctuations exhibits a knee towards smaller scale sizes, indicating the presence of energy input at larger scales and energy dissipation at smaller scales; the low-frequency part of the spectrum is often related to the GTR instability, while the steepening is usually attributed to diffusion, drift waves (LaBelle et al. 1986), or wave steepening (Hysell et al. 1994) although this connection is tenuous due to the lack of continuous data.

2 The NorSat-1 Satellite

With one of the aims to open a new era in ionospheric research, the first Norwegian scientific satellite NorSat-1 was launched from Baikonur, Kazakhstan on July 14th, 2017. NorSat-1 is a multi-payload micro-satellite ($\sim$ 16 kg, 23 cm $\times$ 39 cm $\times$ 44 cm) that was commissioned by the Norwegian Space Center (NSC) and built by the University of Toronto, Institute for Aerospace Studies (UTIAS-SFL). Fig. 1 shows a schematic drawing of the NorSat-1 satellite together with the orientation of the X-, Y-, and Z-axis of the spacecraft body coordinate system. The satellite was launched into a polar orbit at approximately 600 km altitude where it is expected to operate for at least three years. While its main objective is to monitor maritime traffic in Norwegian waters using a Automatic Identification System (AIS) receiver made by Kongsberg Seatex, NorSat-1 also carries two scientific instruments: 1) a Compact Lightweight Absolute Radiometer (CLARA) made by Physikalisch-Meteorologisches Observatorium Davos/World Radiation Center (PMOD/WRC) (Walter et al. 2017), intended to observe total solar irradiation and variations over time; and 2) the multi-needle Langmuir probe (m-NLP) developed at the University of Oslo (UiO) (Bekkeng et al. 2010; Jacobsen et al. 2010). The mission is operated from Vardø and Longyearbyen ground stations in Norway.

With the m-NLP on board the NorSat-1 satellite is an ideal candidate to study the high-latitude and low-latitude ionospheric plasma. With its sampling rate of up to 1 kHz, the m-NLP instrument aboard the NorSat-1 satellite provides an unprecedented opportunity to investigate plasma density structures down to a few meters at LEO. Science objectives of the NorSat-1 satellite using the m-NLP instrument are:

- Primary objective:
  - Identify and quantify the mechanisms that cause the generation of small-scale ionospheric plasma density structures.
- Secondary objectives:
  - Map the global spatial characteristics of meter-scale plasma structures in the ionosphere and their dependence on meso- and large-scale ionospheric drivers.
  - Provide physical understanding of ionospheric structuring mechanisms as the foundation for scintillation forecasts.
  - Understand spacecraft/ionosphere interaction and its impact on in situ plasma density measurements

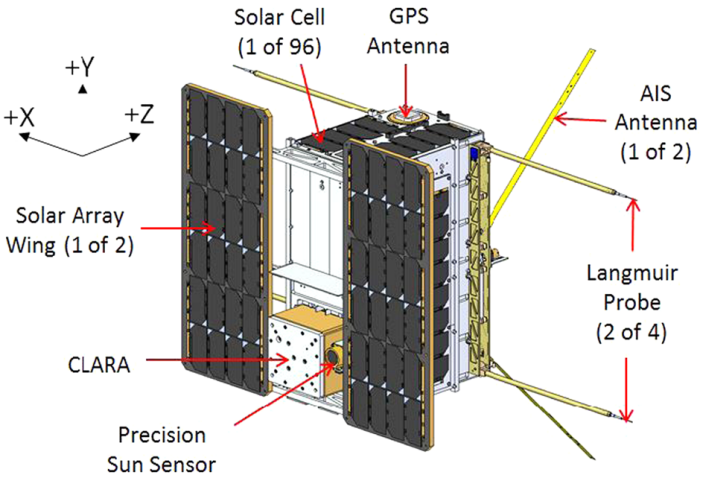

Fig. 1 Schematic drawing of the NorSat-1 satellite. X, Y and Z coordinates represents a satellite body coordinate system. The m-NLP probes are mounted on booms that are deployed after its launch. The NorSat-1 is weighted approximately 16 kg and has dimensions of 23 cm × 39 cm × 44 cm. Image credit: UTIAS-SFL

The m-NLP measurement data will be combined with data from the Super Dual Auroral Radar Network (SuperDARN) and the Defense Meteorological Satellite Program (DMSP) satellites to get the 'big picture' context of the ambient plasma. Over the following years, the satellite will cross the equatorial and polar regions twice every 90 minutes, providing a wealth of data that would be able to help us better understand the mechanisms that dissipate energy input at larger scales by creating small-scale plasma density structures within the ionosphere. In this preliminary paper, no attempt is made to clarify the causes for ionospheric plasma structuring. Instead Sect. 3 presents the m-NLP instrument and its implementation on NorSat-1. In-orbit instrument validation is described in Sect. 4 and examples of the preliminary results from the m-NLP system are shown in Sect. 5. Section 6 concludes the paper.

3 Instrument Description

Since its first flight on board the ICI-2 sounding rocket from Svalbard in December 2008 (Lorentzen et al. 2010; Moen et al. 2012; Oksavik et al. 2012), the m-NLP instrument has been flown on sounding rockets over 10 times (Friedrich et al. 2013; Lynch et al. 2015; Spicher et al. 2016). It is also on board 11 cubesats of the European QB50 constellation (Bekkeng et al. 2017). In this section, the instrument measurement principle and its implementation for the NorSat-1 satellite are presented.

3.1 Measurement Principle

Langmuir probes have been widely used as diagnostic instruments for both laboratory and space plasma (Boggess et al. 1959; Brace et al. 1973; Chapkunov et al. 1976; Brace 1998). A representative current-voltage (I–V) characteristic curve of a Langmuir probe is shown in Fig. 2, where three operational regions of electron saturation, electron retardation and ion saturation are separated by the plasma potential, V_p, and the floating potential, V_f. Mott-Smith and Langmuir (1926) presented the orbital-motion-limited (OML) theory, which deals with collisionless electron and ion trajectories surrounding a spherical or a cylindrical probe. This approach provides a quantitative understanding of the cross-sections for electron and ion collection. Traditional Langmuir probe designs sweep through a range of voltages to obtain the I–V characteristic curve, from which the plasma parameters including ion density,

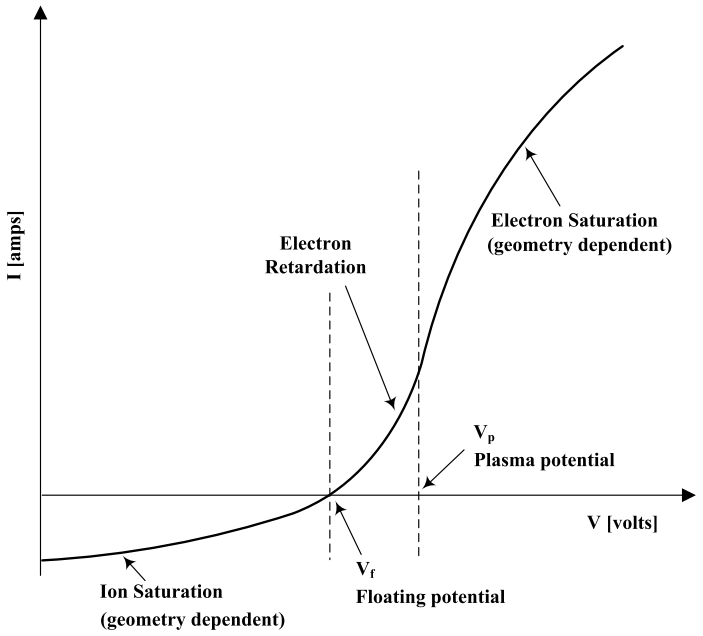

Fig. 2 Representative I–V curve for a Langmuir probe

electron density and electron temperature can be derived. However, sweeping takes time and makes this approach unsuited for high spatial resolution measurements.

The m-NLP design on NorSat-1 uses four cylindrical probes biased at different fixed voltages within the electron saturation region such that the currents to these four probes can be sampled at a much higher rate, resulting in high-resolution plasma density observations. The electron saturation current of a cylindrical probe with a radius much smaller than the Debye shielding distance is in the OML theory given as:

$$I_c = N_e A e \frac{2}{\sqrt{\pi}} \sqrt{\frac{k_B T_e}{2\pi m_e}} \sqrt{1 + \frac{eV}{k_B T_e}} \tag{1}$$

where N_e is the electron density, k_B is the Boltzmann constant, T_e is the electron temperature, e is the electron charge, A is the probe surface area, m_e is the electron mass and V is the probe bias potential, V_b, with respect to the plasma potential, i.e. $V = V_b - V_p$. It is noted that the equation used above is valid under the assumption of a non-drifting, collisionless and non-magnetized plasma. At the altitude of the NorSat-1 orbit all three assumptions are typically fulfilled (Jacobsen et al. 2010) since (1) the thermal speed of the electrons is much larger than the speed of the spacecraft relative to the plasma; (2) the mean free path of the electrons is far greater than both the probe radius and the scale length of the electric potential distribution around the probe; and (3) the Larmor radius is much larger than the probe radius. The current collection expression is a function of the applied bias potential relative to the plasma potential. The probe bias is relative to a common electrical ground, which is connected to the conductive parts of satellite surface so the signal ground is as same as the floating potential of the payload platform. The measurement method of the m-NLP system handles at least two probes biased at two different voltages over the plasma potential to determine the absolute electron density as:

$$N_e = \frac{1}{KA} \sqrt{\frac{\Delta (I_c)^2}{\Delta V_b}} \tag{2}$$

where K is a constant given by $\frac{e^{3/2}}{\pi}\sqrt{\frac{2}{m_e}}$, $\Delta(I_c)^2$ is the difference in the square of collected currents and ΔV_b is the difference in the probe biases (Jacobsen et al. 2010). A key feature of the m-NLP technique is its ability to determine the electron density without the need to know the plasma potential or electron temperature. Under certain conditions, the m-NLP is capable of monitoring the spacecraft potential and its variations as described in Bekkeng et al. (2013, 2017).

As the m-NLP probes collect high-mobility electrons from the surrounding space plasma, the spacecraft will inevitably charge up, and could potentially begin to repel incoming electrons if a sufficient charge is achieved. Furthermore, the bias to the probes, which is relative to the spacecraft potential, might no longer fall within the electron saturation region, thereby compromising the assumptions underlying the m-NLP measurement principle as described above. Thus the NorSat-1 satellite was designed to have as much conductive surface area on the platform as possible.

3.2 Probe and Boom System Design

The NorSat-1 m-NLP instrument consists of four individual probes, each of which has a diameter of 0.5 mm and length of 25 mm. Each probe comes along with a bootstrapped section with 2 mm in diameter and 15 mm in length. The probes were designed to be much smaller than the Debye length of a few to tens of millimeter for common ionospheric plasma conditions. All the probes and bootstraps are carbon coated to provide a uniform material work function for all probes. Each bootstrapped section of the instrument has the same bias as the accompanied probe to mitigate edge effects. Due to the instrument delivery schedule for the spacecraft system integration and a significant delay in the launch, the instrument was exposed to the Earth's atmosphere for about one and a half years, possibly causing probe surface contamination. However, the probes are cleaned by solar heating and ion sputtering over its mission in orbit. Furthermore, the work in Hoang et al. (2017) showed that the m-NLP probes are barely affected by contamination due to water vapor impurities in space. To ensure a good measurement performance against likely impacts of contamination, in-flight probe performance validation by sweeping probe biases is regularly executed.

One of the main design challenges of the m-NLP instrument aboard NorSat-1 was getting the probe tips in an area of undisturbed space plasma. As the spacecraft moves along its orbit, it creates a 'plasma wake' in the opposite direction of travel. Because this 'plasma wake' is poorly understood and hard to predict, the probe tips are desired to be placed on long protruding booms, in an effort to place the tips as far out into the undisturbed plasma as possible.

The NorSat-1 m-NLP probe tips are placed on long deployable booms, whose overall length is limited to the length of the spacecraft itself. Two identical Langmuir probe cassettes are included on NorSat-1, each housing two probes. The cassettes have a total length of 400 mm, base width of 25 mm and height of 23 mm. The booms have a length of 370 mm, including the probes, and are held down by a uniquely designed mechanism. Through spring preloads, the booms are forced to stay stowed. Using a space qualified shape memory alloy pin-puller from TiNi Aerospace Inc., the preloaded spring mechanism can be released in orbit via a ground command, allowing it to perform a half-turn, and consequently pushing both booms out with a large enough force to reach their fully deployed positions. Once fully deployed, each of the booms would lock in place via a locking pin. This cassette design is shown in Fig. 3. While Fig. 3(a) shows the boom system in stowed position, the boom system in deployed position is illustrated in Fig. 3(b). Structural analysis of the boom system has been performed using AutoCAD Inventor and NASTRAN. The analysis results

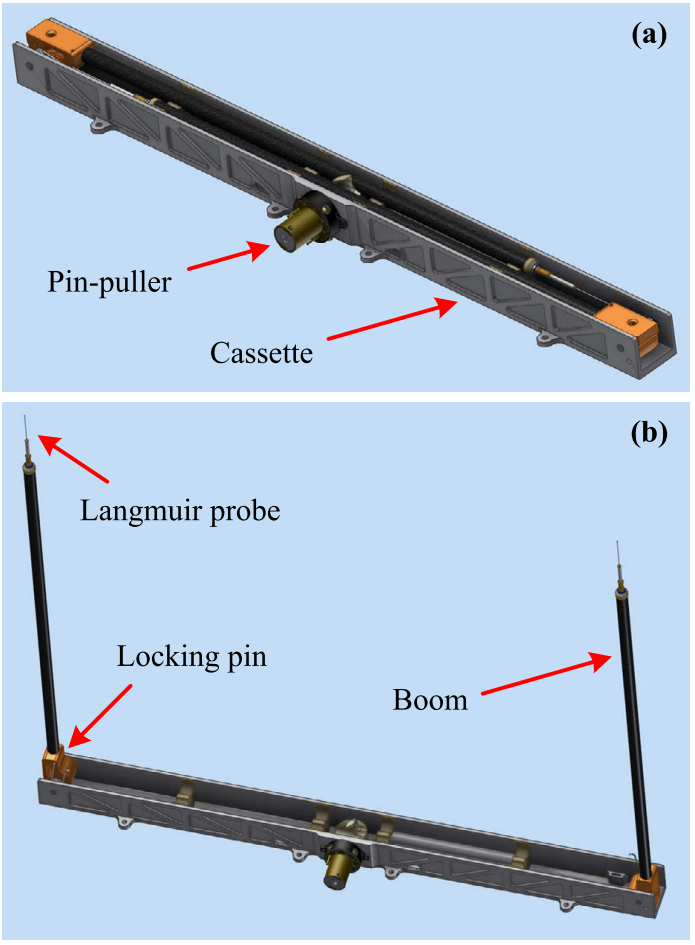

Fig. 3 Probe and boom system design. The cassette has a total length of 400 mm, base width of 25 mm and height of 23 mm. The boom length including a probe is 370 mm. The probe has a diameter of 0.5 mm and length of 15 mm. Bootstrapped section has a diameter of 2 mm and length of 15 mm. (**a**) Stowed position. (**b**) Deployed position

indicate that the first modal frequency of the system is at around 1800 Hz. Within a typical vibration band of 20–2000 Hz, the boom system is regarded as stiff. Experimental vibration tests at Kongsberg Norspace company have validated the analysis. The boom system was tested at 43 Grms maximum out-of-plane without any issues. NorSat-1 deployed the boom system four days after launch, and the recorded boom deployment current for one of the two cassettes is shown in Fig. 4. The m-NLP payload current increased by about 572 mA at 12 V power supply for a short period of less than 90 ms during the deployment. The payload booms and probes after deployment are given a minimum clearance to the spacecraft platform or other payload equipment of about 15 cm.

3.3 Electronics Design

Since the m-NLP probes are very small, the electronics are designed to have a good sensitivity and a low noise floor for very low collected currents. The instrument provides a current measurement resolution of 1 nA and can measure the electron density from 10^8–10^{13} m^{-3}. To get a good signal-to-noise (SNR) at significant lower electron densities, e.g. 5×10^8 m^{-3}, an automatic gain switch control (AGSC) is implemented with a digitally adjustable gain in five discrete steps from 1 to 500. While the m-NLP electronics design for the NorSat-1 satellite is not radiation hardened, a Microsemi ProASIC3L flash-based field-programmable gate array (FPGA) has been used instead of an SRAM-based FPGA for increased radiation tolerance in the LEO environment. The m-NLP electronics block diagram is given in

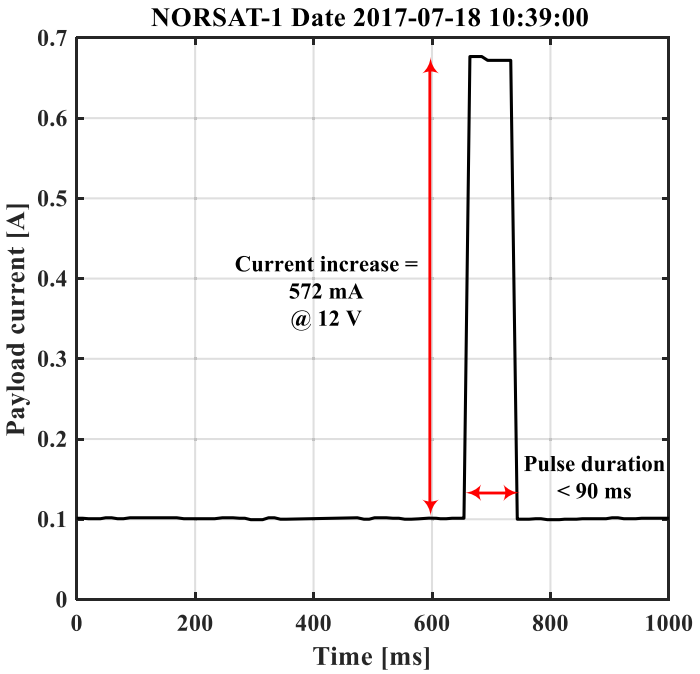

Fig. 4 Boom deployment current recorded on July 18th, 2017

Fig. 5. Due to the highly sensitive AIS receiver onboard NorSat-1, radiated electromagnetic emissions by the m-NLP payload in the 156.0 to 162.5 MHz region are required to be less than −130 dBm. Thus connectors with built-in C-filters are used at both interfaces with the NorSat-1 onboard computer (OBC) and the m-NLP probe. The selected filter connectors have an insertion loss of about −45 dB in the specific region. Currents collected by the probes are converted to voltages and amplified in a pre-amp block. The voltage signals then pass through a low-pass filter to eliminate high frequency noise before going to an Analog-to-Digital converter (ADC). The output digital data are subsequently sent to the OBC through a satellite interface block. By default the data format is 16-bit, but can be adjusted by a ground command. The voltage bias of probe is set by a Digital-to-Analog converter (DAC) controlled by the FPGA. Figure 6(a) depicts the m-NLP electronics system fabricated for NorSat-1. All electronics are fitted on a single printed circuit board, 125 × 94 mm, placed inside an enclosure shown in Fig. 6(b). The enclosure is located inside the spacecraft body. The cassettes, booms and electronics enclosure are all Alodine 1200 coated aluminum 7075 and directly connected to the spacecraft chassis. Inside the electronics enclosure, an electromagnetic interference (EMI) shield is additionally used to cover the digital part, FPGA and memory. The NorSat-1 platform can supply an unregulated voltage from 10–13 V, with a nominal value of 12 V, and a maximum of 1.8 A current continuously to the m-NLP payload. The payload power consumption is verified to be less than 1 W on average throughout the normal operation. During scientifically unfavorable conditions the payload might be switched off to save power and telemetry (TM) resources.

There are two main modes of operation for the m-NLP instrument on NorSat-1, a normal mode and a sweep mode. The normal mode is implemented for high-resolution electron density measurement. In this mode, the m-NLP probes are biased at different fixed voltages, which are expected to lie above the plasma potential in order to make the probes operate in the electron saturation region. Either raw probe current data or onboard computed electron density and spacecraft potential data, can be downloaded depending on the down-link capacity. The second mode is a sweep mode, which is occasionally used for instrument validation.

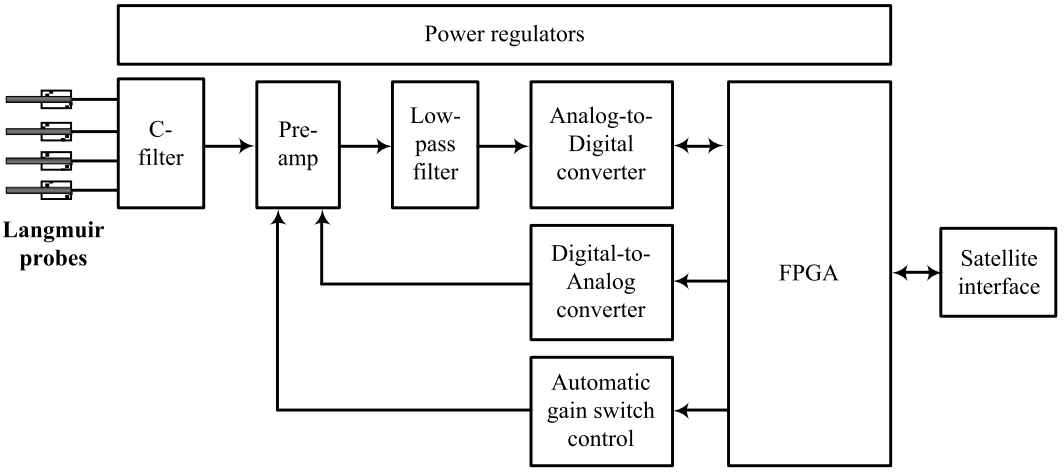

Fig. 5 Electronic block diagram of the m-NLP instrument

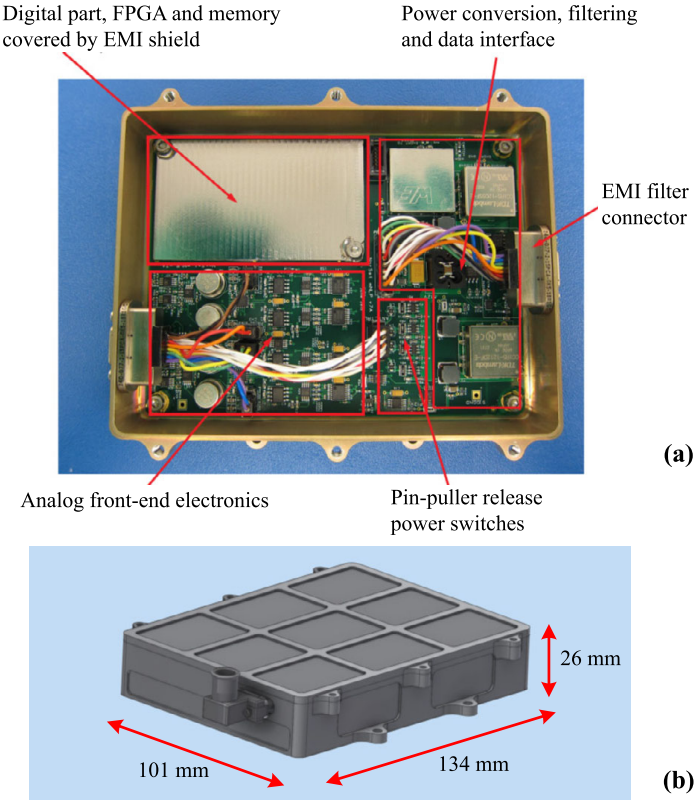

Fig. 6 (**a**) Fabricated m-NLP electronics system. (**b**) Electronics enclosure

In this mode all probes are simultaneously swept from −10 V to +10 V in 128 steps. The step time can be adjusted from 1 ms to 255 ms. Since all probes are swept simultaneously, it is not possible to fully characterize the perturbation of the spacecraft potential during the sweep.

The m-NLP instrument includes a telemetry and command interface to the spacecraft bus. By default at power-up, the baud rate is 230.4 Kbps with an absolute accuracy under all conditions of better than ±50 ppm. The packet structure is compatible with the Nano-satellite Protocol (NSP) which has been developed by UTIAS-SFL (Tuli et al. 2006).

Table 1 Calibration coefficients for each probe of the m-NLP instrument

Probe	Gain = 1		Gain = 5		Gain = 10		Gain = 100		Gain = 500	
	a	*b*	*a*	*b*	*a*	*b*	*a*	*b*	*a*	*b*
Probe 1	1.0166	−17	5.0754	−34	10.164	−47	103.17	−67	516.50	−211
Probe 2	1.0163	−16	5.0722	−28	10.183	−32	103.04	106	506.41	626
Probe 3	1.0171	2	5.0812	−10	10.165	−23	103.43	−71	519.73	−175
Probe 4	1.0175	−4	5.0684	−18	10.215	−25	103.29	−82	513.72	−304

3.4 Instrument Calibration

The complete electronic system was calibrated in the laboratory prior to flight in order to ensure that all biases for each channel were calibrated to zero. Each measurement channel was connected to a Keithley Model 2635 low-current source meter instrument. Input to the instrument is a stepped current ranging from −50 nA to 2 µA, in steps of 10 nA. Compensation of the NorSat-1 data based on the pre-flight calibration is given by:

$$I_{\text{cal}} = \frac{DV - b}{a} \times 0.24068 \text{ [nA]} \tag{3}$$

where I_{cal} is the calibrated current measurement in nA, DV is digital value from the ADC. The coefficients a and b for each probe with different gain settings is given in Table 1.

4 In-orbit Validation

The m-NLP has been validated in orbit by running the sweep mode. The validation was done when NorSat-1 flew over the equatorial region. The sweep mode data are demonstrated in Fig. 7(a) on a linear-scale and in Fig. 7(b) on a logarithmic scale. Since currents measurements at biases lower than −9 V are unreliable, we omitted the data in the plot. It can be seen that while the collected currents of the probe 2, 3 and 4 are relatively similar, the probe 1 current is higher. A possible reason could be variations in the probes' surface due to the long exposure time in the Earth's atmosphere before launch. An alternative reason is that the measurement was done when the probes 2, 3 and 4 were inside the 'plasma wake', whereas the probe 1 was outside. Further runs of the sweep mode are required for better data interpretation. Assuming the ambient plasma is homogeneous during the validation period, we analyzed the I–V curves in Fig. 7 to estimate the electron density and temperature. The value of the floating potential, V_f, is determined by the point where the total collected current goes to zero. The first-order derivative of the electron current with respect to bias voltage is taken to roughly estimate the plasma potential, which locates at the maxima within the derivative. The region limited by the floating potential and plasma potential is the electron retardation region, where the electron temperature, T_e, is calculated. The electron temperature is determined from the slope of the exponential growth of the electron current by least squares fitting of the data as shown in Fig. 7(b). The electron density is determined using Eq. 2. The floating potentials measured by all probes are at around −2.1 V to −1.7 V. While the electron density measured by the probe 1 is 4.90×10^{11} m^{-3}, the other three probes estimate more or less the same electron density of about 3.5×10^{11} m^{-3}. The

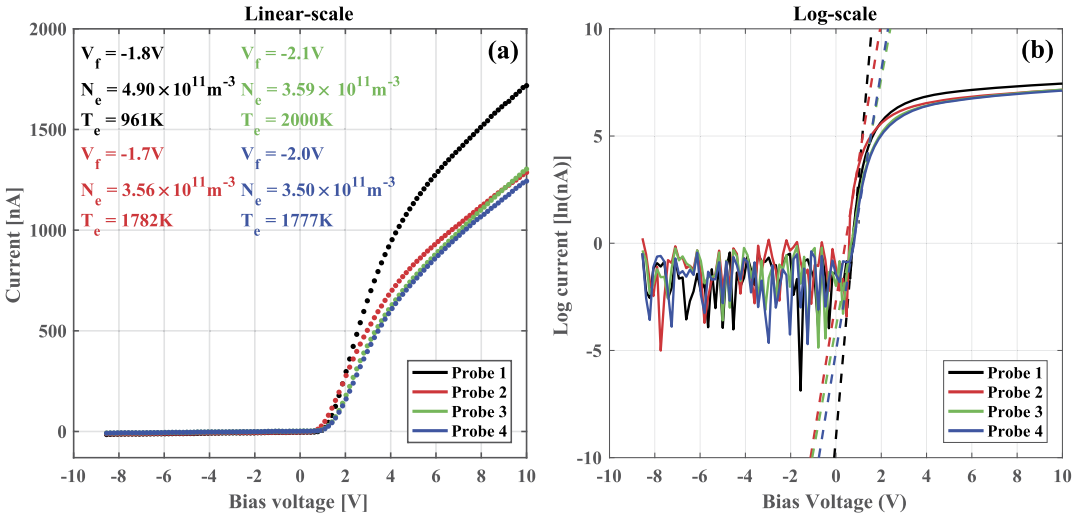

Fig. 7 In-orbit validation of the m-NLP instrument. (**a**) Linear scale. (**b**) Logarithmic scale. In (**b**), *dashed lines* indicate least squares fitted curves in the electron retardation region for the electron temperature estimation

electron temperature is estimated to lie between 961 K and 2000 K. Although some uncertainties still remain, these calculated values lie within the expected range for the equatorial ionosphere, thus showing that the m-NLP is performing as expected.

5 Preliminary Results

The m-NLP does not operate continuously on NorSat-1 since all instruments on the satellite cannot run simultaneously, mainly due to limited bandwidth and power. Data collection on some of the m-NLP operational periods are reported in this paper. Figure 8 shows the data of the m-NLP instrument recorded on August 30th, 2017. The four Langmuir probes were biased at 3 V, 4 V, 5 V and 6 V, and sampled at 400 Hz. Even though the m-NLP instrument has the highest sampling rate of 1 kHz on the NorSat-1 satellite, we have been using 400 Hz during the first stage of the commissioning phase. Collected currents from the four probes and calculated electron density are respectively shown in Fig. 8(a) and (b). The spacecraft floating potential is shown in Fig. 8(c), the spacecraft's geographic latitude and longitude are shown in Fig. 8(d). It can be seen that the data presented in Fig. 8 were collected as the satellite crossed over the northern polar region. The spacecraft attitude is presented in Fig. 8(e), where V_x, V_y, V_z are normalized velocity vectors in X, Y and Z direction of the satellite body coordinate system (see also Fig. 1). It can be seen that during this period the satellite was continuously pointing toward the Sun. Figure 8(a) shows that the collected current from the probe biased at 3 V is negative before 21:00:00 UT, meaning the probe mainly collected positive ions. This is because the spacecraft potential is negatively charged to about −3.5 V as indicated in Fig. 8(c). The vertical dotted line marks the location of the boundary between day- and nightside, i.e., the point at which the satellite passed from sun-lit conditions into darkness. Before entering the Earth's shadow, the NorSat-1 potential fluctuated around −3.5 and −3 V (see Fig. 8(c)). Just after NorSat-1 left the auroral region and entered the eclipse, all probe currents dropped significantly and recovered shortly thereafter. A possible reason for this behavior could be the sudden lack of emission of photoelectrons due to the absence of sunlight. Further investigations into this phenomenon are currently underway.

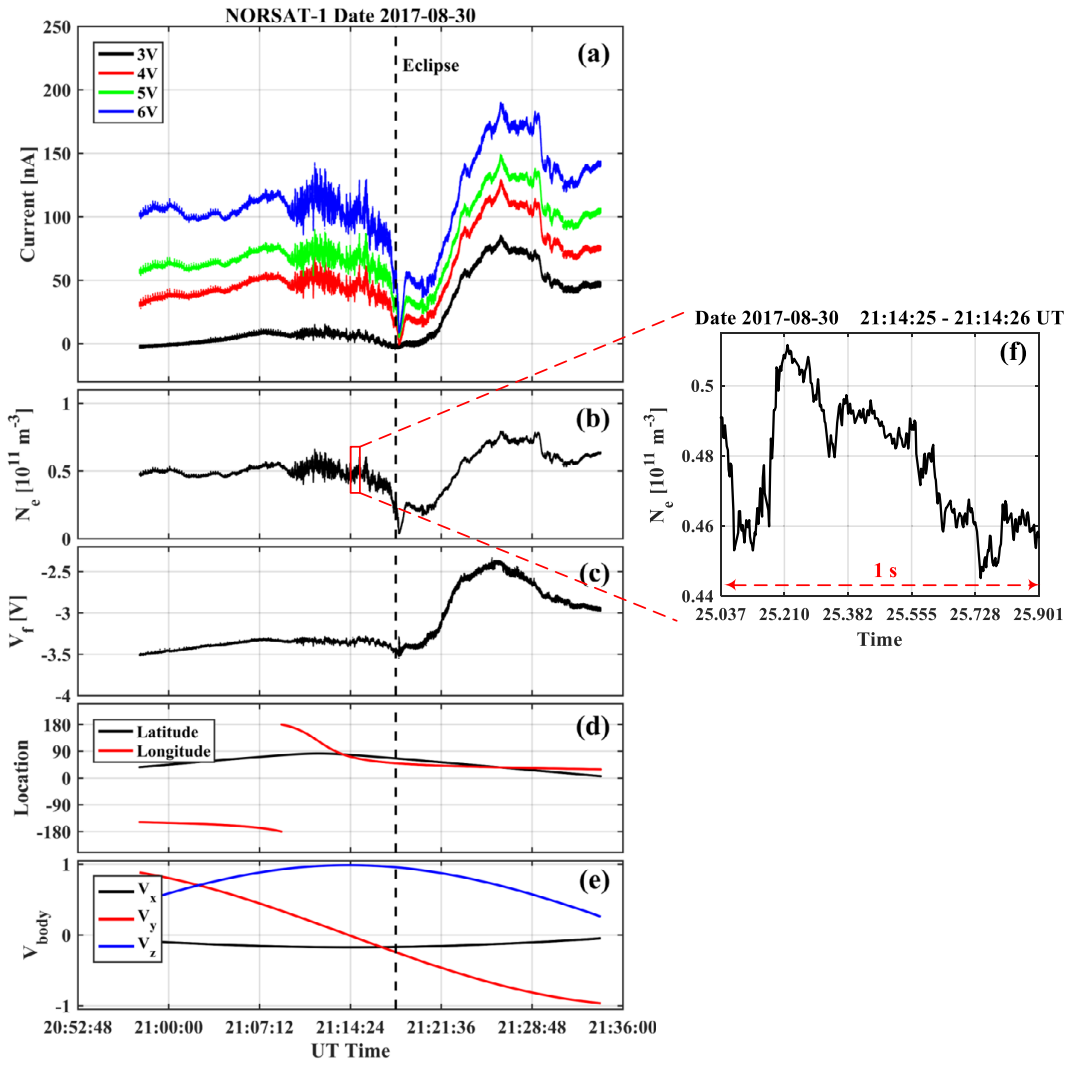

Fig. 8 Measurement data from the m-NLP on August 30th, 2017. *Black dotted line* indicates boundary between day- and night-side. (**a**) Measured currents. (**b**) Electron density N_e. (**c**) Spacecraft potential V_f. (**d**) Latitude and longitude. (**e**) Spacecraft attitude. (**f**) Closer look at electron density measurement for 1 s duration from 21:14:25–21:14:26 UT

Figure 8(b) shows that the electron density fluctuated significantly between 21:10 UT and 21:13 UT—as indicated by the position of the spacecraft, this is likely due to the crossing of the auroral region. A closer look at the electron density measurement for 1 s duration from 21:14:25–21:14:26 UT is shown in Fig. 8(f), where small-scale ionospheric plasma density structures are observed. These structures lie at the heart of the scientific investigation made possible by the m-NLP onboard NorSat-1.

Figure 9 shows a global view of the plasma environment variation along the NorSat-1 orbit on September 15th, 2017. Electron density measured by the m-NLP instrument is compared to that derived from the International Ionosphere Reference (IRI-2016) model, which is an empirical model providing estimates of ionospheric parameters from an altitude of 50 to 2000 km (Bilitza et al. 2014, 2017). Major data sources of the IRI model are the worldwide network of ionosondes, powerful incoherent scatter radars, the ISIS and Alouette topside sounders, and in-situ instruments flown on many satellites and rockets. As can be seen from Fig. 9, there is a quite good agreement between the measurements and the model.

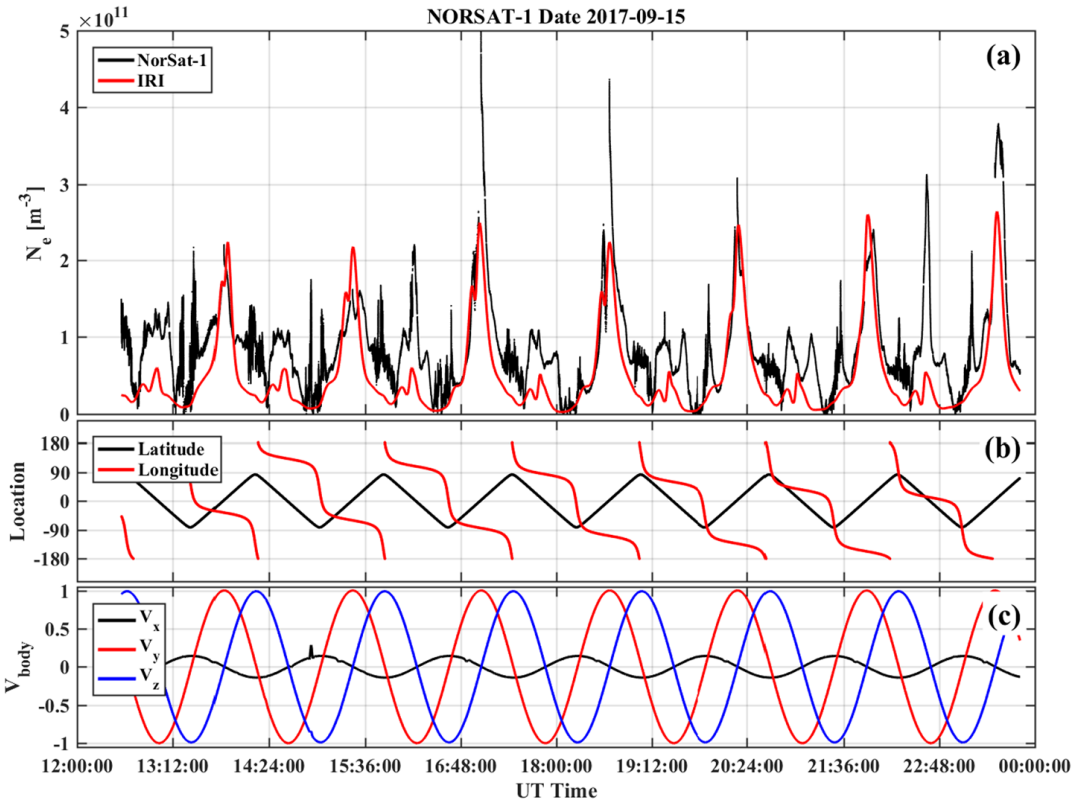

Fig. 9 Global view of plasma variations along NorSat-1 orbit on September 15th, 2017. (**a**) Electron density comparison between NorSat-1 and IRI model. (**b**) Latitude and longitude. (**c**) Spacecraft attitude

There are still discrepancies in other ionospheric regions. In particular, the IRI model possibly underestimates the electron density in the auroral region (Moen et al. 2008). Since ionosondes are an essential data source for the IRI model, the IRI model is known to be less accurate at high and low latitudes, where the ionosonde coverage is lower compared to mid-latitudes (e.g., Bilitza and Reinisch 2008).

6 Conclusion

An overall description of the multi-needle Langmuir probe (m-NLP) instrument aboard the NorSat-1 satellite is presented in this paper. The instrument is capable of measuring the plasma density and spacecraft potential at up to 1 kHz sampling rate, which allows the resolution of plasma density structures at spatial scales of a few tens of meters in low-Earth orbit. Data from the sweep mode shows that plasma parameters calculated from the obtained I–V curves are within the expected range. We plan future in orbit instrument validation by comparing the m-NLP derived plasma density with measurements obtained from the ground by incoherent scatter radars. Overall, the preliminary data presented here indicate a good performance of the m-NLP on board NorSat-1. The electron density measured along the NorSat-1 satellite's orbit was compared with that derived from the IRI-2016 model. While there are still some discrepancies, the comparison results indicate quite good agreement between those two approaches. The IRI model is believed to underestimate the electron density in the polar cap/auroral region.

With its high-inclination orbit of 98°, NorSat-1 carrying the m-NLP system is an excellent candidate to study the high-latitude and low-latitude ionospheric plasma. A complete data set is expected to be acquired over the mission lifetime that will allow addressing the main scientific objectives through statistical studies. It is reasonable to believe that studies using high-resolution NorSat-1 plasma density data will lay the foundations for an operational scintillation forecast, which has a desired long-term goal to predict the quality of trans-ionospheric radio waves, such as those used in Global Navigation Satellite Systems. With such forecasts, the probability of groundings, accidents, and collisions at sea and in the air are reduced, thereby reducing the probability of environmental pollution, injuries, and loss of life, especially in the Arctic region.

Acknowledgements This research has received financial support from Research Council of Norway project 208006, 230996 and ESA PRODEX project 4200090335. We would like to thank the Norwegian Space Center for selecting the m-NLP payload for NorSat-1 and for their financial support of the project. We would like to thank Kongsberg Seatex for providing test facilities for EMI testing of the m-NLP instrument. We would also like to show our gratitude to UTIAS-SFL for their great support during the integration of the instrument in the satellite and to StatSat for putting the instrument into daily operations. The work is also a part of the 4DSpace initiative at the University of Oslo.

References

S. Basu, S. Basu, E. MacKenzie, W.R. Coley, J.R. Sharber, W.R. Hoegy, Plasma structuring by the gradient drift instability at high latitudes and comparison with velocity shear driven processes. J. Geophys. Res. Space Phys. **95**(A6), 7799–7818 (1990). https://doi.org/10.1029/JA095iA06p07799

T.A. Bekkeng, K.S. Jacobsen, J.K. Bekkeng, A. Pedersen, T. Lindem, J.P. Lebreton, J.I. Moen, Design of a multi-needle Langmuir probe system. Meas. Sci. Technol. **085**, 903 (2010). http://stacks.iop.org/0957-0233/21/i=8/a=085903

T.A. Bekkeng, A. Barjatya, U.P. Hoppe, A. Pedersen, J.I. Moen, M. Friedrich, M. Rapp, Payload charging events in the mesosphere and their impact on Langmuir type electric probes. Ann. Geophys. **31**(2), 187–196 (2013). https://doi.org/10.5194/angeo-31-187-2013

T.A. Bekkeng, E.S. Helgeby, A. Pedersen, E. Trondsen, T. Lindem, J.I. Moen, Multi-needle Langmuir probe system for electron density measurements and active spacecraft potential control on cubesats. IEEE Trans. Aerosp. Electron. Syst. (2017 submitted)

D. Bilitza, B. Reinisch, International reference ionosphere 2007: improvements and new parameters. Adv. Space Res. **42**(4), 599–609 (2008). https://doi.org/10.1016/j.asr.2007.07.048

D. Bilitza, D. Altadill, Y. Zhang, C. Mertens, V. Truhlik, P. Richards, L.A. McKinnell, B. Reinisch, The international reference ionosphere 2012—a model of international collaboration. J. Space Weather Space Clim. **4**, A07 (2014). https://doi.org/10.1051/swsc/2014004

D. Bilitza, D. Altadill, V. Truhlik, V. Shubin, I. Galkin, B. Reinisch, X. Huang, International reference ionosphere 2016: from ionospheric climate to real-time weather predictions. Space Weather **15**(2), 418–429 (2017). https://doi.org/10.1002/2016SW001593

R.L. Boggess, L.H. Brace, N.W. Spencer, Langmuir probe measurements in the ionosphere. J. Geophys. Res. **64**(10), 1627–1630 (1959). https://doi.org/10.1029/JZ064i010p01627

L.H. Brace, Langmuir probe measurements in the ionosphere. In: *Measurement Techniques in Space Plasmas: Particles*. Geophysical Monograph Series, vol. 102 (Am. Geophys, Union, Washington, 1998). https://doi.org/10.1029/GM102p0023

L.H. Brace, R.F. Theis, A. Dalgarno, The cylindrical electrostatic probes for Atmosphere Explorer -C, -D, and -E. Radio Sci. **8**(4), 341–348 (1973). https://doi.org/10.1029/RS008i004p00341

J. Buchau, B.W. Reinisch, E.J. Weber, J.G. Moore, Structure and dynamics of the winter polar cap *F* region. Radio Sci. **18**(06), 995–1010 (1983). https://doi.org/10.1029/RS018i006p00995

S.K. Chapkunov, T.N. Ivanova, M.K. Petrunova, K.B. Serafimov, Measurement of electron and ion density and temperature on the Intercosmos 12 satellite, in *Space Research XVI; Proceedings of the Open Meetings of Working Groups on Physical Sciences* (1976), pp. 423–425

L.B.N. Clausen, J.I. Moen, K. Hosokawa, J.M. Holmes, Gps scintillations in the high latitudes during periods of dayside and nightside reconnection. J. Geophys. Res. Space Phys. **121**(4), 3293–3309 (2016). https://doi.org/10.1002/2015JA022199

M. Friedrich, K.M. Torkar, U.P. Hoppe, T.A. Bekkeng, A. Barjatya, M. Rapp, Multi-instrument comparisons of D-region plasma measurements. Ann. Geophys. **31**(1), 135–144 (2013). https://doi.org/10.5194/angeo-31-135-2013

N.A. Gondarenko, P.N. Guzdar, Density and electric field fluctuations associated with the gradient drift instability in the high-latitude ionosphere. Geophys. Res. Lett. **31**(11), L11802 (2004a). https://doi.org/10.1029/2004GL019703

N.A. Gondarenko, P.N. Guzdar, Plasma patch structuring by the nonlinear evolution of the gradient drift instability in the high-latitude ionosphere. J. Geophys. Res. Space Phys. **109**(A9), A09301 (2004b). https://doi.org/10.1029/2004JA010504

N.A. Gondarenko, P.N. Guzdar, Simulations of the scintillation-producing irregularities in high-latitude plasma patches. Geophys. Res. Lett. **33**(22), L22107 (2006). https://doi.org/10.1029/2006GL028033

J.S. Hey, S.J. Parsons, J.W. Phillips, Fluctuations in cosmic radiation at radio-frequencies. Nature **158**, 234 (1946). https://doi.org/10.1038/158234a0

H.M. Hoang, K. Røed, T.A. Bekkeng, E. Trondsen, L.B.N. Clausen, W.J. Miloch, I.J. Moen, High spatial-resolution electron density measurement by Langmuir probe for multi-point observations using tiny spacecraft. Meas. Sci. Technol. (2017). https://doi.org/10.1088/1361-6501/aa87e1

J.D. Huba, G. Joyce, J. Krall, Three-dimensional equatorial spread *F* modeling. Geophys. Res. Lett. **35**(10), L10102 (2008). https://doi.org/10.1029/2008GL033509

D.L. Hysell, M.C. Kelley, W.E. Swartz, R.F. Pfaff, C.M. Swenson, Steepened structures in equatorial spread *F*: 1. New observations. J. Geophys. Res. Space Phys. **99**(A5), 8827–8840 (1994). https://doi.org/10.1029/93JA02961

D.L. Hysell, R.B. Hedden, J.L. Chau, F.R. Galindo, P.A. Roddy, R.F. Pfaff, Comparing *F* region ionospheric irregularity observations from C/NOFS and Jicamarca. Geophys. Res. Lett. **36**(18), L00C01 (2009). https://doi.org/10.1029/2009GL038983

D.L. Hysell, M.A. Milla, L. Condori, J. Vierinen, Data-driven numerical simulations of equatorial spread *F* in the Peruvian sector 3: Solstice. J. Geophys. Res. Space Phys. **120**(12), 10809–10822 (2015). https://doi.org/10.1002/2015JA021877

K.S. Jacobsen, A. Pedersen, J.I. Moen, T.A. Bekkeng, A new Langmuir probe concept for rapid sampling of space plasma electron density. Meas. Sci. Technol. **21**(8), 085902 (2010). https://doi.org/10.1088/0957-0233/21/8/085902

Y. Jin, J.I. Moen, W.J. Miloch, GPS scintillation effects associated with polar cap patches and substorm auroral activity: direct comparison. J. Space Weather Space Clim. **4**, A23 (2014). https://doi.org/10.1051/swsc/2014019

Y. Jin, J.I. Moen, W.J. Miloch, On the collocation of the cusp aurora and the GPS phase scintillation: a statistical study. J. Geophys. Res. Space Phys. **120**(10), 9176–9191 (2015). https://doi.org/10.1002/2015JA021449

Y. Jin, J.I. Moen, W.J. Miloch, L.B.N. Clausen, K. Oksavik, Statistical study of the GNSS phase scintillation associated with two types of auroral blobs. J. Geophys. Res. Space Phys. **121**(5), 4679–4697 (2016). https://doi.org/10.1002/2016JA022613

M.C. Kelley, R. Pfaff, K.D. Baker, J.C. Ulwick, R. Livingston, C. Rino, R. Tsunoda, Simultaneous rocket probe and radar measurements of equatorial spread *F*-transitional and short wavelength results. J. Geophys. Res. Space Phys. **87**(A3), 1575–1588 (1982). https://doi.org/10.1029/JA087iA03p01575

P.M. Kintner, C.E. Seyler, The status of observations and theory of high latitude ionospheric and magnetospheric plasma turbulence. Space Sci. Rev. **41**(1), 91–129 (1985). https://doi.org/10.1007/BF00241347

J. LaBelle, M.C. Kelley, C.E. Seyler, An analysis of the role of drift waves in equatorial spread *F*. J. Geophys. Res. Space Phys. **91**(A5), 5513–5525 (1986). https://doi.org/10.1029/JA091iA05p05513

D.A. Lorentzen, J. Moen, K. Oksavik, F. Sigernes, Y. Saito, M.G. Johnsen, In situ measurement of a newly created polar cap patch. J. Geophys. Res. Space Phys. **115**(A12), A12323 (2010). https://doi.org/10.1029/2010JA015710

K.A. Lynch, D.L. Hampton, M. Zettergren, T.A. Bekkeng, M. Conde, P.A. Fernandes, P. Horak, M. Lessard, R. Miceli, R. Michell, J. Moen, M. Nicolls, S.P. Powell, M. Samara, Mica sounding rocket observations of conductivity-gradient-generated auroral ionospheric responses: small-scale structure with large-scale drivers. J. Geophys. Res. Space Phys. **120**(11), 9661–9682 (2015). https://doi.org/10.1002/2014JA020860

D.J. McEwen, D.P. Harris, Occurrence patterns of *F* layer patches over the north magnetic pole. Radio Sci. **31**(3), 619–628 (1996). https://doi.org/10.1029/96RS00312

J. Moen, N. Gulbrandsen, D.A. Lorentzen, H.C. Carlson, On the MLT distribution of *F* region polar cap patches at night. Geophys. Res. Lett. **34**(14), L14113 (2007). https://doi.org/10.1029/2007GL029632

J. Moen, X.C. Qiu, H.C. Carlson, R. Fujii, I.W. McCrea, On the diurnal variability in F2-region plasma density above the EISCAT Svalbard radar. Ann. Geophys. **26**(8), 2427–2433 (2008). https://doi.org/10.5194/angeo-26-2427-2008

J. Moen, K. Oksavik, T. Abe, M. Lester, Y. Saito, T.A. Bekkeng, K.S. Jacobsen, First in-situ measurements of HF radar echoing targets. Geophys. Res. Lett. **39**(7), L07104 (2012). https://doi.org/10.1029/2012GL051407

J. Moen, K. Hosokawa, N. Gulbrandsen, L.B.N. Clausen, On the symmetry of ionospheric polar cap patch exits around magnetic midnight. J. Geophys. Res. Space Phys. **120**(9), 7785–7797 (2015). https://doi.org/10.1002/2014JA020914

H.M. Mott-Smith, I. Langmuir, The theory of collectors in gaseous discharges. Phys. Rev. **28**, 727–763 (1926). https://doi.org/10.1103/PhysRev.28.727

K. Oksavik, V.L. Barth, J. Moen, M. Lester, On the entry and transit of high-density plasma across the polar cap. J. Geophys. Res. Space Phys. **115**(A12), A12308 (2010). https://doi.org/10.1029/2010JA015817

K. Oksavik, J. Moen, M. Lester, T.A. Bekkeng, J.K. Bekkeng, In situ measurements of plasma irregularity growth in the cusp ionosphere. J. Geophys. Res. Space Phys. **117**(A11), A11301 (2012). https://doi.org/10.1029/2012JA017835

R.F. Woodman, C. La Hoz, Radar observations of f region equatorial irregularities. Journal of Geophysical Research **81**(31), 5447–5466 (1976). https://doi.org/10.1029/JA081i031p05447

C.L. Rino, A power law phase screen model for ionospheric scintillation: 1. Weak scatter. Radio Sci. **14**(6), 1135–1145 (1979). https://doi.org/10.1029/RS014i006p01135

F.S. Rodrigues, M.C. Kelley, P.A. Roddy, D.E. Hunton, R.F. Pfaff, O. de la Beaujardière, G.S. Bust, C/NOFS observations of intermediate and transitional scale-size equatorial spread *F* irregularities. Geophys. Res. Lett. **36**(18), L00C05 (2009). https://doi.org/10.1029/2009GL038905

A. Simon, Instability of a partially ionized plasma in crossed electric and magnetic fields. Phys. Fluids **6**(3), 382–388 (1963). https://doi.org/10.1063/1.1706743

A. Spicher, W.J. Miloch, J.I. Moen, Direct evidence of double-slope power spectra in the high-latitude ionospheric plasma. Geophys. Res. Lett. **41**(5), 1406–1412 (2014). https://doi.org/10.1002/2014GL059214

A. Spicher, A.A. Ilyasov, W.J. Miloch, A.A. Chernyshov, L.B.N. Clausen, J.I. Moen, T. Abe, Y. Saito, Reverse flow events and small-scale effects in the cusp ionosphere. J. Geophys. Res. Space Phys. **121**(10), 10466–10480 (2016). https://doi.org/10.1002/2016JA022999

R.T. Tsunoda, High-latitude *F* region irregularities: a review and synthesis. Rev. Geophys. **26**(4), 719–760 (1988). https://doi.org/10.1029/RG026i004p00719

T.S. Tuli, N.G. Orr, R.E. Zee, Low cost ground station design for nanosatellite missions, in *Proceedings of the AMSAT North American Space Symposium* (2006)

B. Walter et al., The CLARA/NORSAT-1 solar absolute radiometer: instrument design, characterization and calibration, 2017. http://stacks.iop.org/0026-1394/54/i=5/a=674

E.J. Weber, J. Buchau, J.G. Moore, J.R. Sharber, R.C. Livingston, J.D. Winningham, B.W. Reinisch, *F* layer ionization patches in the polar cap. J. Geophys. Res. Space Phys. **89**(A3), 1683–1694 (1984). https://doi.org/10.1029/JA089iA03p01683

R.F. Woodman, Spread F—an old equatorial aeronomy problem finally resolved? Ann. Geophys. **27**(5), 1915–1934 (2009)

Q.H. Zhang, M. Lockwood, J.C. Foster, S.R. Zhang, B.C. Zhang, I.W. McCrea, J. Moen, M. Lester, J.M. Ruohoniemi, Direct observations of the full Dungey convection cycle in the polar ionosphere for southward interplanetary magnetic field conditions. J. Geophys. Res. Space Phys. **120**(6), 4519–4530 (2015). https://doi.org/10.1002/2015JA021172

Paper II

II

The Multi-needle Langmuir Probe Instrument for QB50 Mission: Case Studies of Ex-Alta 1 and Hoopoe Satellites

H. Hoang, K. Røed, T. A. Bekkeng, J. I. Moen, L. B. N. Clausen, E. Trondsen, B. Lybekk, H. Strøm, D. M. Bang-Hauge, A. Pedersen, C. D. A. Nokes, C. Cupido, I. R. Mann, M. Ariel, D. Portnoy, E. Sagi (2019)

Space Science Reviews, *215*(2)
doi: 10.1007/s11214-019-0586-x.

Space Sci Rev (2019) 215:21
https://doi.org/10.1007/s11214-019-0586-x

The Multi-needle Langmuir Probe Instrument for QB50 Mission: Case Studies of Ex-Alta 1 and Hoopoe Satellites

H. Hoang[1] · K. Røed[1] · T.A. Bekkeng[1] · J.I. Moen[1] · L.B.N. Clausen[1] · E. Trondsen[1] · B. Lybekk[1] · H. Strøm[1] · D.M. Bang-Hauge[1] · A. Pedersen[1] · C.D.A. Nokes[2] · C. Cupido[2] · I.R. Mann[2] · M. Ariel[3] · D. Portnoy[3] · E. Sagi[3]

Received: 8 June 2018 / Accepted: 22 January 2019

Abstract The QB50 mission is a satellite constellation designed to carry out measurements at between 200–380 km altitude in the ionosphere. The multi-needle Langmuir probe (m-NLP) instrument has been mounted on board eleven QB50 satellites in order to characterize ambient plasma. The distinct feature of this instrument is its capability of measuring the plasma density at high spatial resolution without the need to know the electron temperature or the spacecraft potential. While the instrument has been deployed on many sounding rockets, the QB50 satellites offer the opportunity to demonstrate the operation of the instrument in low-earth orbit (LEO). This paper provides a brief review of the m-NLP instrument specifically designed for the QB50 mission and the case studies of the instrument's performance on board the Ex-Alta 1 and Hoopoe satellites. The system has also been functionally verified in a plasma chamber at the European Space Research and Technology Center (ESTEC). Although the QB50 mission's scientific goals have not been reached yet and some uncertainties still remain, there are some optimistic in-orbit preliminary results which could be helpful for the system improvement in future campaigns. Particularly, the electron emitter as part of the m-NLP science unit has demonstrated its capability in the plasma chamber and in orbit to mitigate spacecraft charging effects.

Keywords QB50 · Langmuir probe · Electron density · Spacecraft charging

Multi-Point Measurements of the Thermosphere with the QB50 Mission
Edited by David Miles, Robert Wicks and James Burch

H. Hoang
huy.hoang@fys.uio.no

1 Department of Physics, University of Oslo, 0316 Oslo, Norway

2 Department of Physics, University of Alberta, Edmonton, AB, Canada

3 Herzliya Science Center, Hertsliya, Israel

Published online: 18 February 2019

1 Introduction

A CubeSat is a small satellite standard initiated by California Polytechnic State University (Cal Poly) in collaboration with Stanford University's Space System Development Laboratory in 1999. In the CubeSat specification, satellites are described in multiples of 1 U, where 1 U has a volume of 10 cm × 10 cm × 10 cm cube with a maximum weight of 1.33 kg. Typical CubeSats have sizes from 1U to 4U. The project goal was to provide both mechanical and electrical specifications for a standard satellite platform. Additionally, a Poly-PicoSatellite Orbital Deployer (P-POD) was specifically developed to make it easy and secure for a launch provider to include CubeSat satellites aboard a rocket in addition to the rocket's main payload. This kind of standardization makes a CubeSat launch much cheaper than other regular launches of non-standardized satellites, paving the way to scientific investigations and technology demonstrations in low-earth orbit (LEO) in such a way that is cost-effective, timely and relatively easy to accomplish. The use of CubeSats has been increasingly exploited for commercial services and business, e.g. to support the Automatic Identification System (AIS) in the maritime sector (Helleren et al. 2012; Beattie et al. 2013), as well as for military applications (Venturini et al. 2009). The number of universities developing CubeSats has increased over the past decade. The complete set of CubeSat specifications is available online (Program CPSTC 2015).

QB50 is a project within the European Union's Seventh Framework Programme for Research (FP7) that aimed at launching a constellation of 50 CubeSats into the lower thermosphere at approximately 380 km altitude (Muylaert et al. 2009). One of the main purposes of the QB50 project is to achieve sustained and affordable access to space for small scale research space missions and planetary exploration. The QB50 satellites are expected to operate for three up to twelve months before burning up during re-entry. All QB50 satellites can carry their own instruments, but most of the satellites additionally accommodate a set of common science instruments to accomplish atmospheric research in the lower thermosphere. There are three different types of science instruments, each of which is part of the common instrument set. The Ion-Neutral Mass Spectrometer (INMS) is part of set 1. The Flux-Φ-Probe Experiment (FIPEX) is part of set 2 and the multi-needle Langmuir probe (m-NLP) science unit is part of set 3. A surface thermal monitor (STM) is installed in all satellites.

This paper will present the m-NLP science unit which has been built at the University of Oslo (UiO) (Bekkeng et al. 2010; Jacobsen et al. 2010). The main purpose of this paper is to provide a description of the instrument and to present first in-flight results from a system and technology demonstration point of view. The science unit includes four needle Langmuir probes and an electron emitter. The probe system had been deployed on many sounding rockets before the QB50 mission to resolve ionospheric plasma density variations down to the meter scale. In order to adapt to the limited resources in terms of size, power consumption and data-link budget in the QB50 satellites, instrument design adaptations have been made. Until now we have received the m-NLP data from three QB50 satellites including Experimental Albertan satellite number 1 (Ex-Alta 1), Hoopoe and Pegasus. While in this paper the data from the Ex-Alta 1 and Hoopoe satellites are discussed, the data from the Pegasus satellite will be reported in another paper. This paper is organized as follows. Section 2 describes the theoretical background and scientific objectives. A detailed description of the m-NLP science unit is introduced in Sect. 3, which also presents the system verification in a plasma chamber at the European Space Research and Technology Center (ESTEC). Section 4 presents some in-orbit preliminary results with two case studies of the Ex-Alta 1 and Hoopoe satellites, followed by some conclusions in Sect. 5.

2 Background and Scientific Objectives

2.1 Background

Since the initial work by Mott-Smith and Langmuir in the 1920s (Mott-Smith and Langmuir 1926), Langmuir probes have been widely used as diagnostic instruments for both laboratory and space plasma (Boggess et al. 1959; Chen 1965; Brace et al. 1973; Chapkunov et al. 1976; Brace 1998). Traditionally, Langmuir probe operation is based on sweeping the bias voltage of a conductor exposed to a plasma and measuring the collected currents from the conductor. With the general understanding of the processes involved in the plasma, Langmuir probe theory is applied to infer the plasma parameters through the obtained current-voltage (I-V) curve. However, sweeping takes time at least hundreds of ms and makes this approach unsuited for high spatial resolution measurements on space platforms.

Instead of sweeping the bias voltage, the m-NLP design (Jacobsen et al. 2010; Bekkeng et al. 2010) uses several cylindrical probes biased at different fixed voltages within the electron saturation region such that the currents to these probes can be sampled at a much higher rate, resulting in high-resolution plasma density observations. For a probe with its radius much smaller than the Debye length of a non-drifting, unmagnetized, and collisionless plasma, the electron saturation current to the probe can be described by the Orbital-Motion-Limited (OML) theory as follows:

$$I_e = C\, I_{e0}\left(1 + \frac{eV}{k_B T_e}\right)^{\beta} \tag{1}$$

where $C = 2/\sqrt{\pi}$ for a cylindrical geometry and $C = 1$ for planar and spherical geometries of the probes. $I_{e0} = N_e A_e e\sqrt{\frac{k_B T_e}{2\pi m_e}}$, is the electron thermal current to the probe at the plasma potential, N_e is the electron density, k_B is the Boltzmann constant, T_e is the electron temperature, e is the electron charge, A_e is the probe surface area, m_e is the electron mass and V is the probe bias potential V_b with respect to the plasma potential V_p i.e. $V = V_b - V_p$. On space platforms, a probe bias is relative to a common electrical ground, which is connected to the spacecraft chassis so the signal ground is at the same level of the floating potential of the spacecraft chassis. Thus the parameter V in Eq. (1) can be expressed by $V = V_b + V_f$, where the spacecraft floats relative to the plasma at a bias of V_f and V_b is the probe bias with respect to this spacecraft floating potential. The parameter β is equal to 0, 0.5 and 1 for a planar, cylindrical and spherical probe, respectively. The electron density derived by the m-NLP instrument deploying two cylindrical probes is given by:

$$N_e = \frac{1}{K A_e}\sqrt{\frac{\Delta(I_c^2)}{\Delta V_b}} \tag{2}$$

where K is a constant given by $\frac{e^{3/2}}{\pi}\sqrt{\frac{2}{m_e}}$, $\Delta(I_c^2)$ is the difference in the square of collected currents and ΔV_b is the difference in the probe biases (Jacobsen et al. 2010). Under certain conditions, the m-NLP is also capable of monitoring the spacecraft potential and its variations as described in Bekkeng et al. (2013).

Since the β parameter is prone to variations, an alternative data analysis technique is using a method of non-linear least squares when fitting the probe measurement currents with the model shown in Eq. (1) i.e. with β, N_e and T_e being free parameters of the fitting

process. The two approaches of estimating the electron density using Eq. (2) and the non-linear least squares fit have advantages and disadvantages with respect to the current m-NLP implementation, and both can be applied to derive the plasma parameters (Hoang et al. 2018).

2.2 Scientific Objectives

The m-NLP probe system was originally developed for the Investigation of Cusp Irregularities (ICI) program and it was first flown on the ICI-2 sounding rocket in 2008 (Moen et al. 2012; Oksavik et al. 2012; Spicher et al. 2014, 2015b). Our basic research desire is to explore the chain of multiscale physical processes giving rise to ionospheric scintillations (Moen et al. 2013, and references therein). Radio communication and Global Navigation Satellite Systems (GNSS) both suffer from ionospheric scintillations, and the problems are most severe at low and high latitudes (e.g. Basu and Basu 1981; Basu et al. 1988a,b, 1990, 1998). In GNSS ionospheric systems, scintillations can cause rapid variations of the measured phase of a signal, causing degraded positioning accuracy. These problems may take place during the entire solar cycle (Kintner et al. 2007). Prikryl et al. (2010) reported serious GNSS signal degradation in the polar cusp even during solar minimum conditions. Unless ionospheric scintillation forecasts to reliably predict the signal quality become available, users in the affected regions cannot fully rely on communication and navigation services without taking risk. The m-NLP system on a fleet of CubeSats is expected to be the most cost effective approach to monitor the dynamics of the problem regions and hence be valuable to any attempts to regional or global forecast services.

The idea with QB50 was to deploy several spacecraft like pearls on a string, which would be ideal to revisit instability regions and to study growth and decay of instability regions, as was demonstrated during the commissioning of the Swarm mission (Spicher et al. 2015a; Goodwin et al. 2015). In addition to provide plasma density measurements, the main drivers for UiO to get involved with the QB50 mission are:

- Demonstrate the m-NLP system can provide high resolution electron density measurements on board CubeSats.
- Explore temporal evolution of F-region plasma irregularities in the polar caps and in the equatorial region.

3 The m-NLP Science Unit Description and System Verification

3.1 Instrument Design for QB50 Satellites

We have adapted the m-NLP design for being possibly deployed on the QB50 satellites by: (i) lowering the power consumption, (ii) introducing onboard data processing (due to telemetry constraints), and (iii) developing an electron emitter to control the spacecraft potential (Bekkeng et al. 2017).

3.1.1 Probe and Boom System Design

The m-NLP science unit includes four Langmuir probes, which are made from a coaxial cable with bootstrapped sections to mitigate edge effects. Since the spacecraft conductive surface area of CubeSats is much smaller than that of sounding rockets, the probe diameter

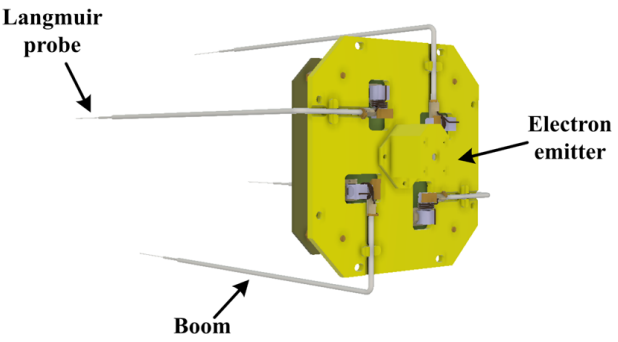

Fig. 1 CAD drawing of the m-NLP science unit, where the booms are in stowed position. The spring-loaded booms are designed to be stowed along the outer surface of the QB50 spacecraft, with a length of about 188 mm including the probe tip and its bootstrapped section

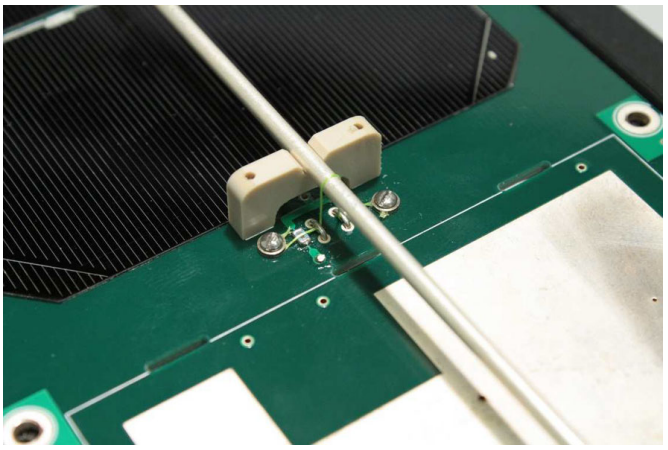

Fig. 2 Boom hold down and release mechanism (HDRM)

was reduced from 0.51 mm for the sounding rocket version to 0.29 mm, to alleviate the effect of spacecraft charging. Each of the m-NLP probes is 25 mm in length and has the bootstrapped section of 1.19 mm in diameter and 15 mm in length. The probe design specification ensures that the probe radius is much smaller the Debye length, which is ranging from a few mm to tens of mm in LEO, for the OML condition fulfillment.

One of the main design challenges of the m-NLP instrument aboard the QB50 satellites was getting the Langmuir probes in an area of undisturbed space plasma. When the spacecraft travels in space, it creates a 'plasma wake' in the opposite direction of travel similar to the disturbed region behind a moving vessel. Because this 'plasma wake' is poorly understood and hard to predict, the probes were placed on long booms, aiming at locating these probes as far out into the undisturbed plasma as possible. Thus the boom system, consisting of four separated booms, was designed to be deployable and mounted on a common Alodine 1200S coated top plate of the m-NLP science unit. The spring-loaded booms are stowed along the outer surface of QB50 spacecraft, with a length of about 188 mm including the probe tip and its bootstrapped section. The boom length is limited to the size of the spacecraft itself. A computer-aided design (CAD) drawing of the m-NLP science unit is shown in Fig. 1, where the booms are in stowed position. Each boom has a diameter of 2.2 mm and is made of aluminium. All the probes, bootstrapped supports and booms are coated by Aerodag G to provide a uniform material work function. Each boom has an individual hold down and release mechanism (HDRM) as shown in Fig. 2. The spring-loaded booms are forced to stay stowed by using burn wires, which are pressed down onto two resistors with good thermal contact. The current needed to burn each of the wires is about 0.5 A at 5.0 V for 3 seconds. The preloaded spring mechanisms can be released on orbit via a ground command, allowing them to perform a 90° turn, and consequently push the probes out to reach their deployed position.

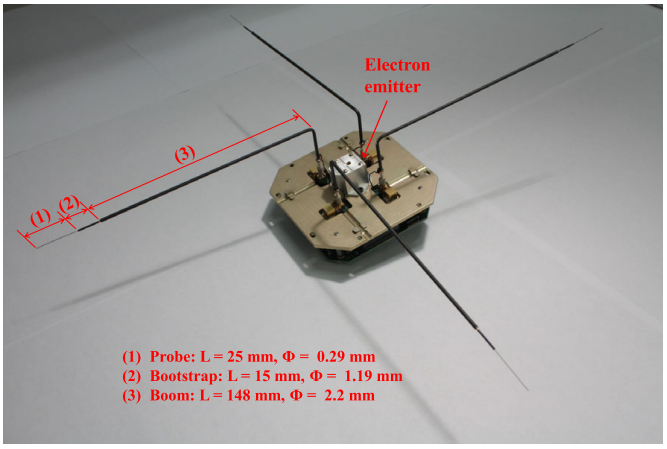

Fig. 3 Fabricated m-NLP science unit for QB50, where the booms are in their deployed position. The probe is 25 mm long with a 0.29 mm diameter. The bootstrapped section has a length of 15 mm and a diameter of 1.19 mm. Figure adapted from Bekkeng (2017)

Table 1 Summary of the QB50 m-NLP instrument

Mass	220 g (including the boom system and the electron emitter)
Current measurement range	1 nA–2.2 μA
Current resolution	1 nA
Electron density range ($V_b = 2$ V and $T_e = 1000$ K)	2×10^9 m^{-3}–4.5×10^{12} m^{-3}
Output data resolution	16-bit raw data (can down-sample to 14-, 12-, 10-bit for more data)
Sampling rate	Up to 255 Hz
Power consumption	∼1.1 W (including the electron emitter and real-time processing power for electron density and spacecraft potential computation)

3.1.2 Electronics Design

All electronics are fitted on two circuit boards, front-end and digital PCBs, placed under the Alodine coated top plate. While the m-NLP electronics design for the QB50 satellites is not radiation hardened, a Microsemi ProASIC3L flash-based Field Programmable Gate Array (FPGA) has been used instead of an SRAM-based FPGA for an improvement of the radiation tolerance in the LEO environment. Details about the system electronics block are given in Bekkeng (2017). The power consumption has reduced from 3 W of the sounding rocket version to about 1 W, which meets the power constraint for the QB50 satellites. The sampling rate can be set to upto 255 Hz, however, the downlink budget of approximately 2 Mbits per day for the QB50 satellites severely limit the rate the amount of measurement time of the m-NLP instrument. The data length is set by default at 16-bit, but can be reduced to 14-, 12- and 10-bit to deal with the limited bandwidth. The fabricated m-NLP science unit is shown in Fig. 3, where the booms are in their deployed position. It is noted that the instrument signal ground is electrically connected to the satellite platform. Table 1 presents a summary of the m-NLP developed for the QB50 mission.

The m-NLP instrument has two main operation modes, a fixed-bias mode and a swept-bias mode. While in the fixed-bias mode the probes are biased at fixed voltages for high-

Table 2 Summary of the electron emitter developed for the QB50 mission

Type	Thermionic emission
Accelerating voltage	38 V
Filament voltage range	0.9–1.2 V
Emitted current range	20 nA–54 μA
Power consumption	Up to 100 mW @ 1.2 V filament voltage

resolution electron density measurement, the probes bias are swept from −10 V to 10 V with 21 evenly spaced voltage steps in the sweep mode. The time between two adjacent voltage steps can be adjusted from 1 ms to 255 ms. The fixed-bias mode is the mode during normal operation. The swept-bias mode can be used for probe performance verification during operations.

3.1.3 Miniaturized Thermionic Electron Emitter (MTEE)

The four probes of the m-NLP instrument by default are positively biased with respect to the spacecraft payload potential, in order to draw electron currents from the ambient plasma that are then used to determine the electron density. Current continuity thus requires a return ion current through conductive surface of the spacecraft bus that are connected to the power ground. Since the ion current density is much smaller than the electron current density, either the spacecraft conductive surface is expected to be sufficiently large to neutralize coming electrons through the probes or the spacecraft platform would charge to highly negative potential values. As many of the QB50 satellite skin parts are not metallic, their conductive surfaces are very limited, for example, the total conductive surface area of Ex-Alta 1 is at most 120 cm^2. In order to address this issue, an electron emitter was developed and encased in the housing mounted on the top plate of the m-NLP science unit as shown in Fig. 3.

Electrons emitted from a heated filament are accelerated by a anode with its positive potential (accelerating voltage). The anode has a rather large aperture of 3 mm, which prevents the majority of the electrons constituting the beam from being collected at the anode. As the electrons will get an outwards velocity when passing through the aperture of the anode, an additional electrode with an aperture of 3.2 mm is placed 1 mm in front of the anode. The purpose of this electrode is to limit the beam angle by collecting the most deflected electrons. The electrode was placed at the same potential as the anode to otherwise not affect the electron beam. More details of the electron emitter development can be found in Bekkeng et al. (2017). Test results of the electron emitter have been obtained, showing that with a limited power consumption of 100 mW, emitted beam currents could reach up to 54 μA for the accelerating voltage of 38 V on the QB50 satellites (Hoang et al. 2017). Electrons emerge from the electron emitter with a kinetic energy of 38 eV, which corresponds to about 3600 km/s with respect to the satellite. Thus the electron recollection probability is expected to be small. Assuming no negative spacecraft charging and ram ion current, an upper limit for the required emitter current can be estimated of the sum of the probe currents. For a 1000 K plasma with density of 10^{10} m^{-3}, and biases of 1 V, 1.5 V, 2 V, and 2.5 V, the upper limit is estimated about 20 nA using Eq. (1). At a density of 10^{12} m^{-3}, the maximum current needed is about 2 μA, presumably well within the capability of the emitter. Table 2 presents a summary of the electron emitter developed for the QB50 mission.

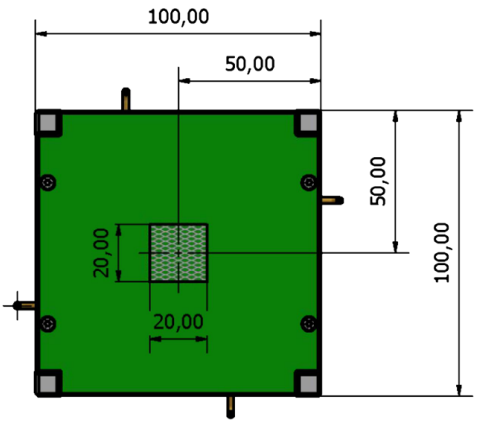

Fig. 4 STM TH0 placement on QB50 spacecraft wake-side panel (+Z face). The four protruding parts are the m-NLP boom system viewed from the +Z face. All dimensions are given in mm

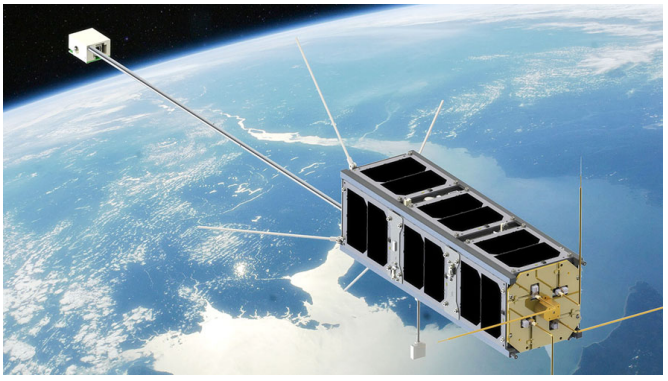

Fig. 5 QB50 Ex Alta-1 satellite

3.1.4 Surface Thermal Monitor (STM)

Besides the electron density and spacecraft charging measurement by the m-NLP science unit, there are six temperature transducers AD590*F, namely TH0 to TH5, to monitor the temperature on the QB50 satellites. The output of each transducer is a twisted pair of wires without shielding. Five of those transducers, TH0 to TH4, are used to keep track of the temperature on different panels of the satellites, i.e. inner side of solar panels, and TH5 examines the temperature inside the m-NLP electronics board. Figure 4 shows placement of TH0 on the +Z face of the QB50 spacecraft. The QB50 spacecraft body coordinate system can be found in Denis (2015). The transducers TH1 to TH4 are located in the −Y, −X, +Y and +X face, respectively. The m-NLP science unit reads the temperature values from the transducers and periodically sends data to the onboard computer (OBC) every 3.5 minutes by default. The sampling rate of the STM experiment can be adjust via a ground command.

3.1.5 Instrument Interfaces to QB50 Spacecraft

The m-NLP science unit has been designed to mechanically interface to commercially available CubeSat structures either through an adapter or through appropriate relocation of mounting holes on the structures. The instrument was accommodated at the −Z face, which is ram velocity direction, of the QB50 spacecraft. Figure 5 illustrates a rendering model of Ex-Alta 1 (Mann et al. 2019, this issue), one of the QB50 satellites, carrying the m-NLP instrument in front. The m-NLP science unit goes 36 mm, including the connector, downwards into the QB50 CubeSat structure, from the bottom side of the science unit top plate. In addition to the m-NLP science unit, the Ex-Alta 1 satellite carries a digital fluxgate

magnetometer (FGM) (Miles et al. 2013, 2016), which is used for high frequency measurements of the Earth's magnetic field. The magnetometer is encased in a box mounted on a long boom behind the satellite.

The QB50 platform supplies regulated voltages 3.3 V and 5.0 V to the m-NLP science unit. The two power rails should achieve stabilized nominal voltage levels within maximum 150 ms after switch-on. A 3.3 V, 9600 bps universal asynchronous receiver-transmitter (UART) serial interface is used to control the science unit from the OBC.

3.1.6 Instrument Script Handling

The OBC can execute scripts to operate the m-NLP instrument. The scripts provide a time-tagged sequence of commands to be run. The m-NLP state transition is quite complicated, for instance, measurement data collection can not be executed until voltages and currents of the power rails are correctly verified and the probe bias is set. There is no broadcast mode on the QB50 m-NLP science unit, hence a data request command is sent whenever the measurement data collection is needed. As a consequence, the script size is relatively large, e.g. a script to turn on the instrument, ask for the housekeeping data including voltages and currents of the system power rails and then turn the instrument off is 42-byte long. A typical script with a common procedure to send a few data request commands would be more than 500-byte long.

It is possible to get either raw data (21 current measurements from each of the 4 probes) or the processed data (81 electron density and 8 spacecraft floating potential values) from the m-NLP science unit for each data request command.

3.2 System Functional Verification in Plasma Chamber

We have functionally verified the m-NLP science unit system in the plasma chamber at the European Space Research and Technology Center (ESTEC). The unit was mounted on a 2U CubeSat, where its solar cells were not installed. The solar panel locations were instead filled with conducting metallic patches. The total conductive surface area of the CubeSat is estimated to be about 450 cm^2, including the Alodine coated top plate. The test setup is shown in Fig. 6, where the m-NLP science unit is located on the ram-facing side of the CubeSat. The CubeSat was hung from the top of the chamber. This chamber is 1 m in diameter and 2 m in length, with a plasma source generating argon ions accelerated to approximately 7 km/s. Electrons in the chamber are generated by a heated filament, and flow down the centerline of the chamber together with the argon ions.

The effect of using the electron emitter is clearly shown in Fig. 7. The m-NLP system operated in the swept-bias mode, where all of the m-NLP probes were swept simultaneously from -10 V to 10 V with 21 steps and back to -10 V with the same number of steps. The probes bias, which was swept with several step durations longer than 180 ms, as a function of time is shown in Fig. 7(a). The filament voltage of the electron emitter is shown in Fig. 7(b) and the CubeSat floating potential, which was measured by a multimeter, is shown in Fig. 7(c). Before 250 s, the electron emitter was off. When the m-NLP probes were not biased, the CubeSat potential was around -0.6 V. At the time the swept-bias mode started, the CubeSat floating potential became more negative and reached around -4 V as long as the biases of the probes were at 10 V. After 250 s, the electron emitter was turned on with the filament voltage of 1.2 V. The CubeSat potential became less negative and relatively stabilize around -0.3 V when the m-NLP probes were not in operation. The CubeSat floated at about -3 V as the probes were biased at 10 V. It is noted that the situation where the

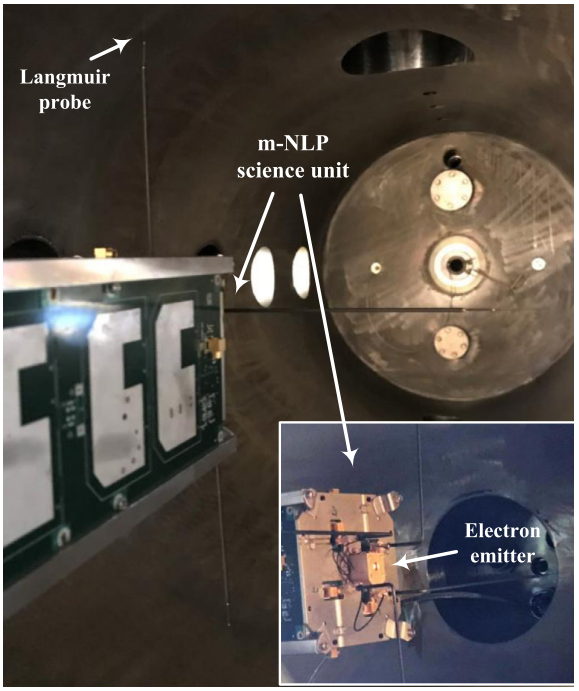

Fig. 6 Verification setup in the ESTEC plasma chamber. The total conductive surface area of the CubeSat is about 450 cm^2, including the Alodine coated top plate. The bottom right conner of the figure shows the m-NLP science unit with the electron emitter being in operation

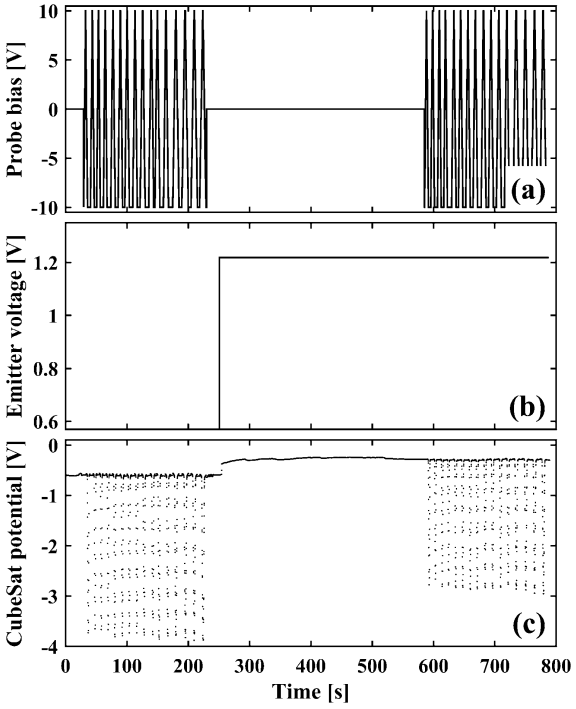

Fig. 7 Spacecraft charging mitigation by the electron emitter. (**a**) All the probes of m-NLP are swept simultaneously from −10 V to 10 V and back to −10 V. (**b**) Filament voltage of the electron emitter. (**c**) CubeSat floating potential

probes are all biased at 10 V is an extreme case. The CubeSat potential could be less negative for the m-NLP probes biased at smaller positive voltages. The CubeSat potential variations are superimposed over one complete period of the probe bias sweep for the two cases: with and without using the electron emitter as shown in Fig. 8. As can be seen, the CubeSat potential started to be affected by the sweeping probes when the biases were higher than 1 V.

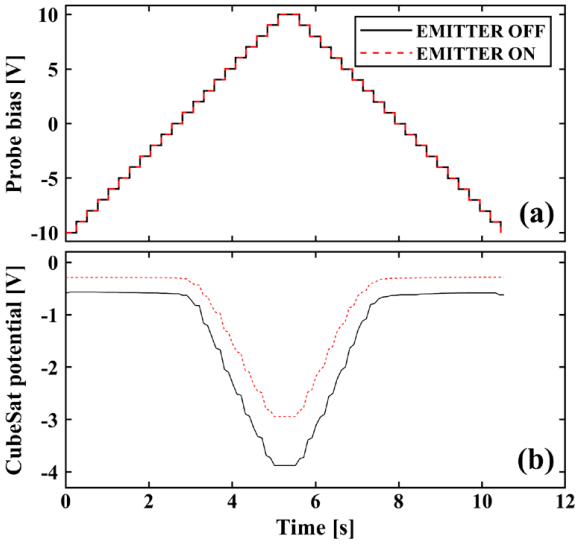

Fig. 8 The CubeSat potential variations shown in Fig. 7 are superimposed over one complete period of the probe bias sweep for the two cases: with and without using the electron emitter. (**a**) Probe bias. (**b**) CubeSat potential

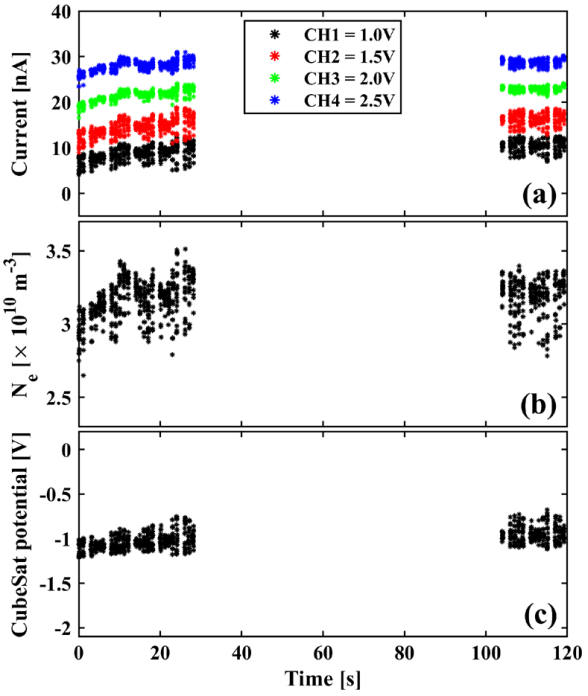

Fig. 9 Measurements in the fixed-bias mode of the m-NLP instrument. (**a**) Currents collected by the m-NLP probes. (**b**) Estimated electron density. (**c**) Estimated CubeSat potential. The electron density was calculated using Eq. (2) (having a linear fit to the square of the probe currents) and the floating potential was calculated using a method described in Bekkeng et al. (2013, 2017)

Figure 9 shows the electron density and CubeSat floating potential estimated by the m-NLP system running in the fixed-bias mode. The probes were biased at different fixed voltages 1.0 V, 1.5 V, 2.0 V and 2.5 V. During the measurement period, the electron emitter was turned on with the filament voltage of 1.2 V. The currents collected by the m-NLP probes are shown in Fig. 9(a). Figures 9(b)–(c) show the calculated electron density and CubeSat floating potential, respectively. The electron density and CubeSat floating potential were roughly estimated to be 3–3.5 $\times$ 10^{10} m^{-3} and to be -1 V, respectively, during the measurement process. The electron density was calculated using Eq. (2) (having a linear fit to the square of the probe currents) and the floating potential was calculated using a method described in Bekkeng et al. (2013, 2017). It is noted that the above values are just coarse estimates since the plasma environment in the chamber at the time of the measurements was

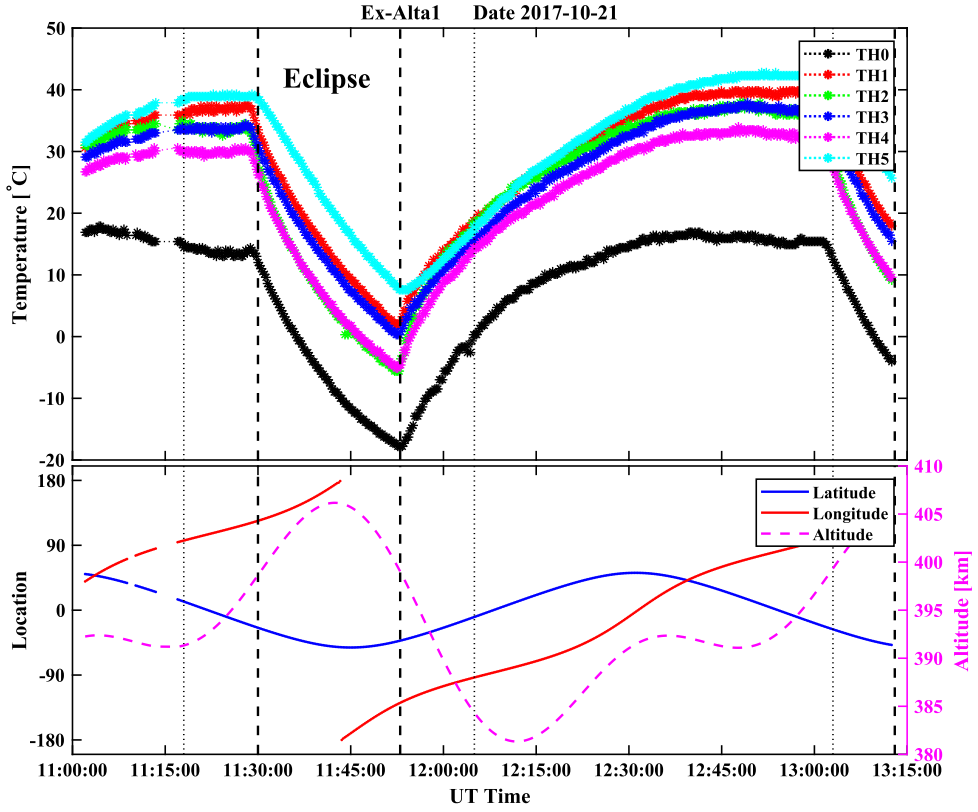

Fig. 10 Measured temperatures by the STM experiment on Ex-Alta 1. While the black dashed lines indicate the boundary of nighttime region, the black dotted lines indicate the boundary of civil twilight. (**a**) Measured temperatures. (**b**) Satellite location (left axis) and altitude above WGS84 (right axis)

believed to be inhomogeneous, meaning that the plasma at the probe locations might differ from each other. As can be seen from Fig. 9, the measurements were only taken before 30 s and after 100 s. Though there are some uncertainties in the plasma parameter estimation, the testing results have validated the m-NLP system operation and the electron emitter, which is capable of mitigating the spacecraft charging issue.

4 First Results and Discussions

Preliminary in-orbit data from two satellites, Ex-Alta 1 and Hoopoe, of the QB50 constellation are reported in this paper. Ex-Alta 1 and Hoopoe are 3U and 2U Cubesats developed by University of Alberta, Canada and Space Laboratory of the Herzliya Science Center, Israel, respectively. They were both launched on May 18, 2017 from the International Space Station (ISS). Due to the low bandwidth and limited power on the two satellites, the m-NLP instrument has been in operation only a few times since its launch into orbit.

4.1 Ex-Alta 1 Case Study

Results of the STM experiment on Ex-Alta 1 recorded on October 21st, 2017 from 11:00–13:15 UT are shown in Fig. 10(a), where temperatures measured by the six transducers, TH0 to Th5, are presented. Figure 10(b) shows the satellite location and altitude. The black

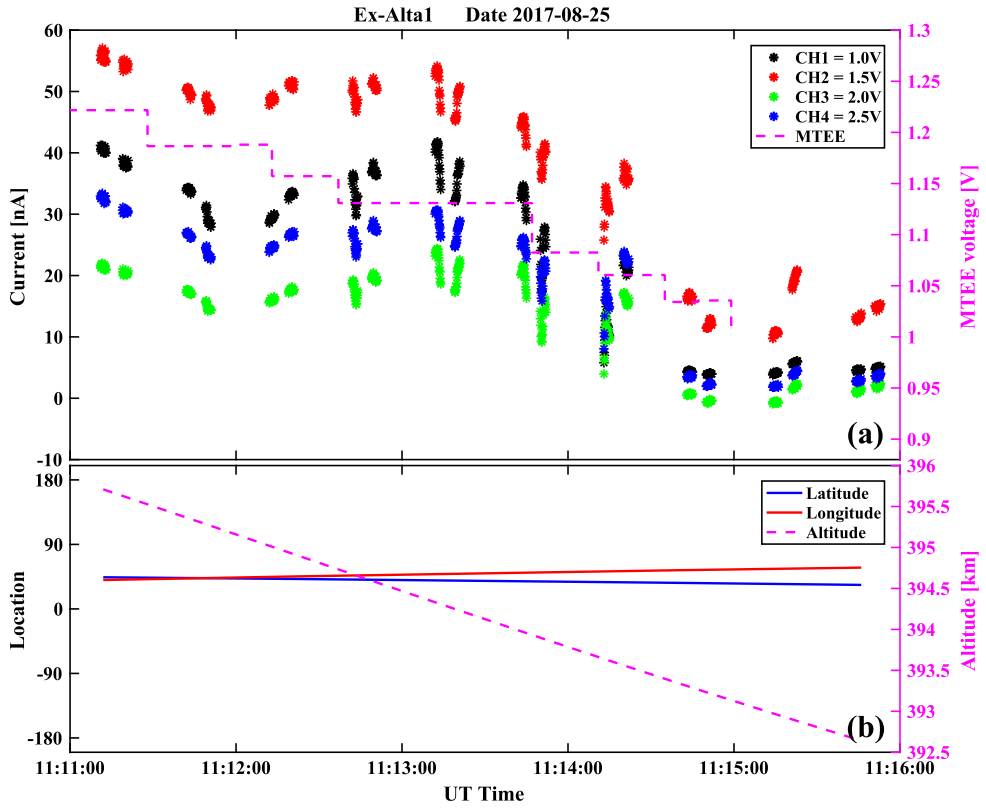

Fig. 11 Measurement data from the m-NLP instrument on Ex-Alta 1 on August 25th, 2017. (**a**) Currents collected by the m-NLP probes (left axis) and MTEE filament voltage (right axis). (**b**) Satellite location (left axis) and altitude above WGS84 (right axis)

dashed lines indicate the boundaries of nighttime region and the black dotted lines indicate the boundaries of civil twilight. As can be seen from Fig. 10(a) all of the temperatures reduced by about 30 °C when the satellite flew from the dayside into the nightside. While the temperature inside the m-NLP electronics board TH5 is the highest of about 40 °C on the dayside, the transducer TH0 located on the bottom panel (+Z face) reports the lowest temperature on the dayside of just about 15 °C. The nightside temperatures of these two transducers are about 9 °C and −19 °C, respectively. The satellite attitude data are currently under calibration. When the calibration process is done, this would help us to know exactly relative position of the spacecraft side panels with respect to the Sun.

During the first commissioning phase of the satellite, the m-NLP probes were biased at 0.8 V, 1.4 V, 1.8 V and 2.2 V without using the electron emitter. This was done on August 15th, 2017 from 11:01–11:15 UT when the satellite was in eclipse. The results indicate almost no electron current collected by the probes probably due to highly negative spacecraft potential. Ten days later, the electron emitter was turned on and the m-NLP recorded data from 11:11 to 11:16 UT as shown in Fig. 11. Even though the m-NLP instrument has the highest sampling rate of 255 Hz on the QB50 satellites, we have been using just 10 Hz on Ex-Alta 1 due to the low bandwidth. Currents from the four m-NLP probes, which were biased at 1.0 V, 1.5 V, 2.0 V and 2.5 V, are shown in Fig. 11(a), where Fig. 11(b) shows the satellite location and altitude. The filament voltage of the electron emitter was set at 1.2 V for 10 min before this measurement process. During the measurement period, the filament voltage reduced from 1.2 V to 1 V by several voltage steps. The pink dashed line in Fig. 11(a) indicates the filament voltage, which are actual measured data stored as housekeeping data

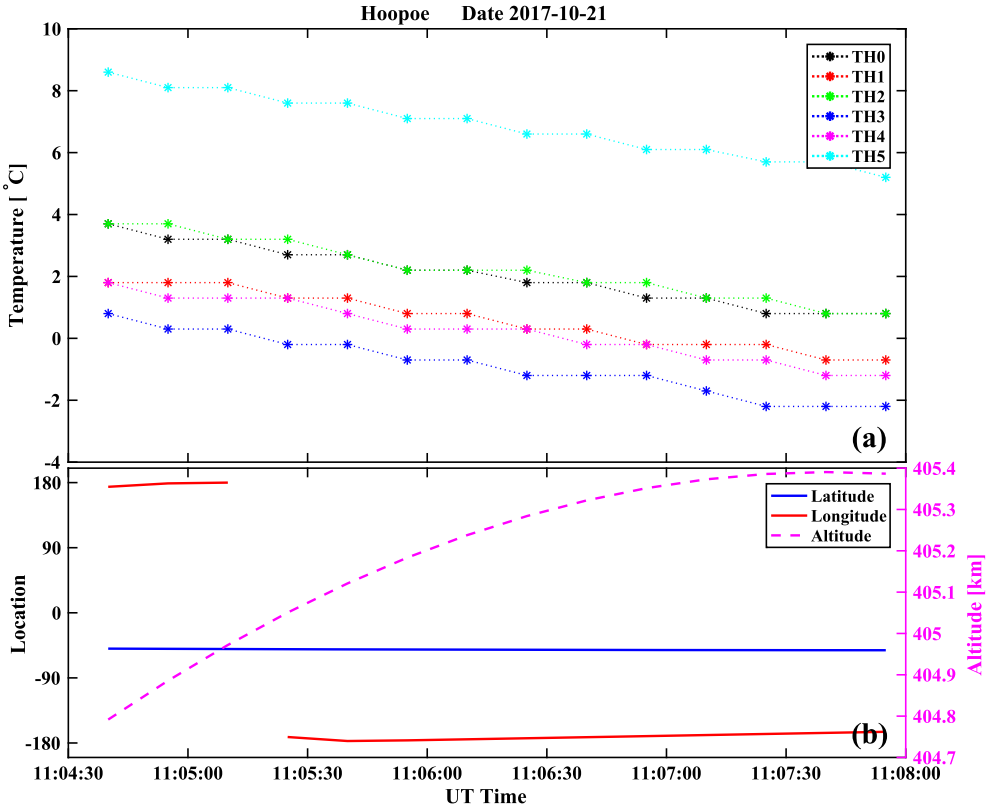

Fig. 12 Measured temperatures by the STM experiment on Hoopoe. The measurements were done when the satellite was in eclipse. (**a**) Measured temperatures. (**b**) Satellite location (left axis) and altitude above WGS84 (right axis)

on the m-NLP system and are periodically transfered to the OBC. The filament voltage were intended to be reduced to 0.95 V at around 11:15:30 UT, however, the housekeeping data after about 11:15:00 UT have not been available.

In looking at Fig. 11, the astute reader is confronted with several anomalies, e.g. the current from the 1.0 V probe is higher than that from the probes with higher bias. Since the attitude data are not available yet, it is difficult to understand what happened to the m-NLP probes. There are three main possibilities: (i) some of probes were possibly damaged during the satellite launch such that the surfaces of the probes are not uniform (ii) the probes were affected by plasma wakes (iii) the probes were not connected to the electronics in the right order. The other possibilities could be due to that photoemission from the four probes may be different and/or electrons emitted from the emitter may be recollected by the probes and contaminate the measurement. It is not possible to estimate the electron density and spacecraft potential with the data anomaly. However, a decrease in the probe current is observed as the MTEE filament voltage is lowered. This is a first in-flight demonstration of the MTEE, showing its capability to help mitigate the negative charging of the platform.

4.2 Hoopoe Case Study

Due to limited onboard memory of the Hoopoe satellite, the m-NLP binary script is limited to up to 2 KB. This not only limits the sampling rate of the m-NLP science unit, but also the measurement time. Results of the STM experiment on Hoopoe recorded on October 21st, 2017 for 4 minutes from 11:04–11:08 UT are shown in Fig. 12, where Fig. 12(a) shows the

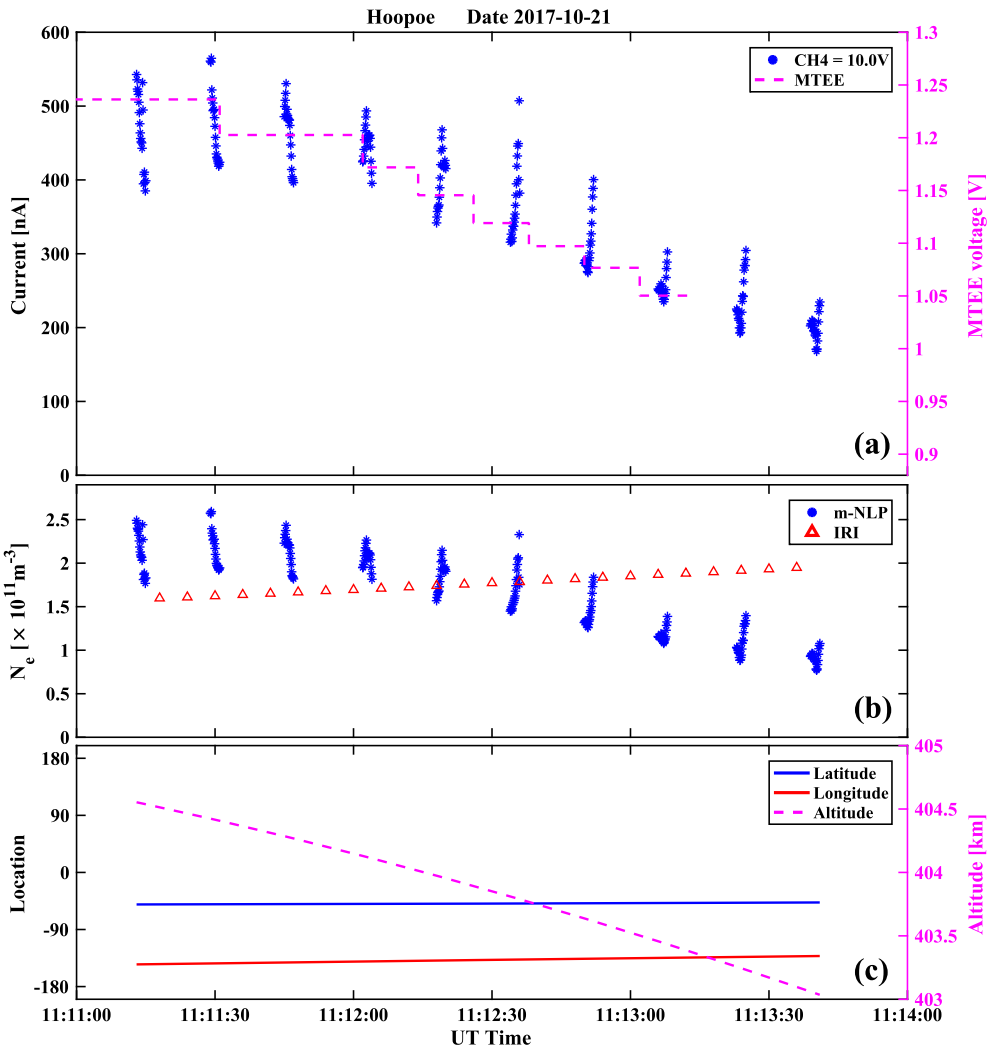

Fig. 13 Measurement data from the m-NLP instrument on Hoopoe on October 21st, 2017. (**a**) Current collected by the 10 V probe (left axis) and MTEE filament voltage (right axis). (**b**) Comparison between the electron density estimated by the 10 V probe and that estimated by the IRI model. (**c**) Satellite location (left axis) and altitude above WGS84 (right axis)

measured temperatures and Fig. 12(b) shows the satellite location and altitude. The experiment was done when the satellite was in eclipse. The m-NLP electronics board temperature is also the highest at about 8 °C. Because of the lack of satellite attitude information, we cannot further interpret the data.

Similar to the Ex-Alta 1 case, the m-NLP probes biased at 0.8 V, 1.4 V, 1.8 V and 2.2 V collected almost no electron current without the electron emitter. The emitter was later used during probe operation. The m-NLP measurement data recorded on October 21st, 2017 are shown in Fig. 13. Because of a likely problem during the boom deployment, only probe 4 has been used in the operation. Thus it is not possible to estimate the spacecraft floating potential. However, the electron density can be roughly estimated as $N_e \simeq \frac{1}{KA_e}\frac{I_e}{\sqrt{V_b}}$, which is an approximation of Eq. (1) for a single probe with high bias. Probe 4 was then biased at 10 V and the sampling rate was set at 10 Hz. The MTEE filament voltage was at 1.2 V for 10 min before this measurement process. During the measurement period, the filament voltage was intended to reduce from 1.2 V to 0.95 V, however, the housekeeping data in-

dicate only a reduction down to 1 V. The housekeeping data after 11:15 UT are missing, thus we are not sure if the MTEE followed the script setting. The electron density can be roughly estimated about 1–2.5 $\times$ 10^{11} m^{-3} as shown in Fig. 13(b), which also shows the electron density derived by the International Reference Ionosphere (IRI-2016) model. The IRI model is an empirical model providing estimates of ionospheric parameters from an altitude of 50 to 2000 km (Bilitza et al. 2014, 2017). It can be seen that, the electron density calculations of the two approaches are similar. The satellite location and altitude are shown in Fig. 13(c). There was also a decrease in the measurement current as the MTEE voltage decreased as shown in Fig. 13(a). The lower the MTEE filament voltages, the more negative the spacecraft floating potential causing the reduction in the electron current. The reader could think that the reduced current could be due to a reduction in the electron density since the satellite traveled over 1000 km during the measurement period. However, at the time the satellite was traveling towards the equator where the electron density was expected to be higher as estimated by IRI as shown in Fig. 13(b). This has further validated the MTEE operation in orbit. It is noted that unlike the m-NLP technique, the electron density estimated by the single probe is dependent on the spacecraft potential, i.e. the more negative spacecraft potential the lower the estimated electron density.

5 Conclusion

The multi-needle Langmuir probe (m-NLP) developed for the QB50 mission has been described in detail. The system functional verification has been successfully performed in the plasma chamber. The in-orbit preliminary data from two of the satellites in the QB50 constellation, Ex-Alta 1 and Hoopoe, have been shown, indicating that even though there were some uncertainties with the m-NLP measurements, some optimistic in-orbit preliminary results, which could be helpful for the system improvement in future campaigns, have been obtained. A first in-flight demonstration of the MTEE has been presented, showing a dependency on the MTEE filament voltage for the probe currents in both case studies. Furthermore, the temperatures on all of the satellite panels were observed, showing nominal values as expected. Work is in progress to resolve remaining uncertainties. Additionally, the spacecraft attitude information on the satellites has not been available, making it hard to interpret collected data, not only for probe behavior analysis but also for physical process study.

There are some remarks to be made about this campaign. First, with their really small diameter, the m-NLP probes are delicate and vulnerable to any vibration or shock during the delivery and launch process, which could possibly affect the probe surface uniformity. Second, while the great advantage of the m-NLP instrument is the ability to resolve plasma density with high resolution, due to the relatively low down-link capacity of the QB50 mission, the m-NLP sampling rate has been set at a very low level. Last but not least, in order to interpret the m-NLP data, accurate spacecraft attitude information is needed and this has not been achieved yet in the mission. Moving forward, spacecraft bus and boom design changes should be considered for the optimal m-NLP science unit deployment. Although the electron emitter is included in the unit, increasing the minimum conductive surface area of the spacecraft to be on the order of 200–300 cm^2 is recommended in order to more effectively operate the electron emitter, which balances the electron current collected by the m-NLP probes. This would also help to reduce the power consumption from the electron emitter. In addition, the boom system design can be adjusted so that the m-NLP probes are similarly oriented with respect to the magnetic field in order to mitigate likely impacts of

a bi-Maxwellian plasma (Jacobsen et al. 2010). It is important to have a detection mechanism in the next version of the m-NLP system to make sure whether the boom deployment is successful. Particle-In-Cell (PIC) simulation is also needed to do modeling the coupling between the m-NLP probes, the spacecraft and the plasma. This would give a better understanding of how the probe current collections are affected by plasma wakes and spacecraft sheath expansion.

The QB50 mission is an excellent opportunity for the involved universities to develop their own space programs and to demonstrate both space instruments and measurement techniques in orbit. The mission has enabled us to develop the electron emitter, which is then used to actively control the spacecraft platform potential. This makes the m-NLP available on many spacecraft for ionospheric density measurements.

Acknowledgements This research has received financial support from Research Council of Norway project 208006, 230996 and ESA PRODEX project 4200090335. The research leading to these results has also received funding from the European Research Council under the European Union's Seventh Framework Programme (FP7/2007-2013)/ERC grant agreement 284427. The work is also a part of the 4DSpace initiative at the University of Oslo. Ex-Alta-1 was carried out with the financial support of donors, two crowd-sourcing campaigns, from the Canadian Space Agency, and from the Canadian Natural Sciences and Engineering Research Council (NSERC) through a Discovery Grant to Ian R. Mann.

References

S. Basu, S. Basu, Equatorial scintillations—a review. J. Atmos. Terr. Phys. **43**(5), 473–489 (1981). https://doi.org/10.1016/0021-9169(81)90110-0. Equatorial Aeronomy—I

S. Basu, S. Basu, E. MacKenzie, P.F. Fougere, W.R. Coley, N.C. Maynard, J.D. Winningham, M. Sugiura, W.B. Hanson, W.R. Hoegy, Simultaneous density and electric field fluctuation spectra associated with velocity shears in the auroral oval. J. Geophys. Res. Space Phys. **93**(A1), 115–136 (1988a). https://doi.org/10.1029/JA093iA01p00115

S. Basu, E. MacKenzie, S. Basu, Ionospheric constraints on VHF/UHF communications links during solar maximum and minimum periods. Radio Sci. **23**(03), 363–378 (1988b). https://doi.org/10.1029/RS023i003p00363

S. Basu, S. Basu, E. MacKenzie, W.R. Coley, J.R. Sharber, W.R. Hoegy, Plasma structuring by the gradient drift instability at high latitudes and comparison with velocity shear driven processes. J. Geophys. Res. Space Phys. **95**(A6), 7799–7818 (1990). https://doi.org/10.1029/JA095iA06p07799

S. Basu, E.J. Weber, T.W. Bullett, M.J. Keskinen, E. MacKenzie, P. Doherty, R. Sheehan, H. Kuenzler, P. Ning, J. Bongiolatti, Characteristics of plasma structuring in the cusp/cleft region at Svalbard. Radio Sci. **33**(6), 1885–1899 (1998). https://doi.org/10.1029/98RS01597

A.M. Beattie, Ø. Helleren, R.E. Zee, In-flight operations of a high-availability nanosatellite constellation for maritime observation, in *Proceedings of the 64th International Astronautical Congress (IAC 2013)* (2013). http://utias-sfl.net/wp-content/uploads/International-Astronautical-Congress-2013-IAC-13B431x16514.pdf

T.A. Bekkeng, Development of a miniaturized multi-needle Langmuir probe system for in-situ measurements of electron density and spacecraft floating potential. PhD thesis, University of Oslo (2017)

T.A. Bekkeng, K.S. Jacobsen, J.K. Bekkeng, A. Pedersen, T. Lindem, J.P. Lebreton, J.I. Moen, Design of a multi-needle Langmuir probe system. Meas. Sci. Technol. **085**, 903 (2010). http://stacks.iop.org/0957-0233/21/i=8/a=085903

T.A. Bekkeng, A. Barjatya, U.P. Hoppe, A. Pedersen, J.I. Moen, M. Friedrich, M. Rapp, Payload charging events in the mesosphere and their impact on Langmuir type electric probes. Ann. Geophys. **31**(2), 187–196 (2013). https://doi.org/10.5194/angeo-31-187-2013

T.A. Bekkeng, E.S. Helgeby, A. Pedersen, E. Trondsen, T. Lindem, J.I. Moen, Multi-needle Langmuir probe system for electron density measurements and active spacecraft potential control on cubesats. IEEE Trans. Aerosp. Electron. Syst. (2017, submitted)

D. Bilitza, D. Altadill, Y. Zhang, C. Mertens, V. Truhlik, P. Richards, L.A. McKinnell, B. Reinisch, The international reference ionosphere 2012—a model of international collaboration. J. Space Weather Space Clim. **4**, A07 (2014). https://doi.org/10.1051/swsc/2014004

D. Bilitza, D. Altadill, V. Truhlik, V. Shubin, I. Galkin, B. Reinisch, X. Huang, International reference ionosphere 2016: from ionospheric climate to real-time weather predictions. Space Weather **15**(2), 418–429 (2017). https://doi.org/10.1002/2016SW001593

R.L. Boggess, L.H. Brace, N.W. Spencer, Langmuir probe measurements in the ionosphere. J. Geophys. Res. **64**(10), 1627–1630 (1959). https://doi.org/10.1029/JZ064i010p01627

L.H. Brace, Langmuir probe measurements in the ionosphere, in *Measurement Techniques in Space Plasmas: Particles* (Am. Geophys. Union, Washington, 1998). https://doi.org/10.1029/GM102p0023

L.H. Brace, R.F. Theis, A. Dalgarno, The cylindrical electrostatic probes for atmosphere explorer -c,-d, and -e. Radio Sci. **8**(4), 341–348 (1973). https://doi.org/10.1029/RS008i004p00341

S.K. Chapkunov, T.N. Ivanova, M.K. Petrunova, K.B. Serafimov, Measurement of electron and ion density and temperature on the intercosmos 12 satellite, in *Space Research XVI; Proceedings of the Open Meetings of Working Groups on Physical Sciences* (1976), pp. 423–425

F.F. Chen, *Electric Probes* (Academic Press, San Diego, 1965), pp. 113–200, Chap. 4

A. Denis, QB50 System Requirements and Recommendations (2015). https://qb50.eu/index.php/tech-docs/category/25-up-to-date-docs?download=89:qb50-docs

L.V. Goodwin, B. Iserhienrhien, D.M. Miles, S. Patra, C. van der Meeren, S.C. Buchert, J.K. Burchill, L.B.N. Clausen, D.J. Knudsen, K.A. McWilliams, J. Moen, Swarm in situ observations of f region polar cap patches created by cusp precipitation. Geophys. Res. Lett. **42**(4), 996–1003 (2015). https://doi.org/10.1002/2014GL062610

Ø. Helleren, Ø. Olsen, B.T. Narheim, A.N. Skauen, R.B. Olsen, Aissat-1—2 years of service, in *European Space Agency Small Satellite Systems and Services Symposium* (2012)

H. Hoang, K. Røed, T.A. Bekkeng, E. Trondsen, L.B.N. Clausen, W.J. Miloch, J.I. Moen, High spatial-resolution electron density measurement by Langmuir probe for multi-point observations using tiny spacecraft. Meas. Sci. Technol. (2017). https://doi.org/10.1088/1361-6501/aa87e1

H. Hoang, K. Røed, T.A. Bekkeng, J.I. Moen, A. Spicher, L.B.N. Clausen, W.J. Miloch, E. Trondsen, A. Pedersen, A study of data analysis techniques for the multi-needle Langmuir probe. Meas. Sci. Technol. **065**, 906 (2018). http://stacks.iop.org/0957-0233/29/i=6/a=065906

K.S. Jacobsen, A. Pedersen, J.I. Moen, T.A. Bekkeng, A new Langmuir probe concept for rapid sampling of space plasma electron density. Meas. Sci. Technol. **085**, 902 (2010). http://stacks.iop.org/0957-0233/21/i=8/a=085902

P.M. Kintner, B.M. Ledvina, E.R. de Paula, GPS and ionospheric scintillations. Space Weather **5**(9), s09003 (2007). https://doi.org/10.1029/2006SW000260

I.R. Mann et al., The ex-alta 1 cubesat mission Space Sci. Rev. (2019, this issue)

D.M. Miles, J.R. Bennest, I.R. Mann, D.K. Millling, A radiation hardened digital fluxgate magnetometer for space applications. Geosci. Instrum. Method. Data Syst. **2**(2), 213–224 (2013). https://doi.org/10.5194/gi-2-213-2013

D.M. Miles, I.R. Mann, M. Ciurzynski, D. Barona, B.B. Narod, J.R. Bennest, I.P. Pakhotin, A. Kale, B. Bruner, C.D.A. Nokes, C. Cupido, T. Haluza-DeLay, D.G. Elliott, D.K. Milling, A miniature, low-power scientific fluxgate magnetometer: a stepping-stone to cube-satellite constellation missions. J. Geophys. Res. Space Phys. **121**(12), 11839–11860 (2016). https://doi.org/10.1002/2016JA023147

J. Moen, K. Oksavik, T. Abe, M. Lester, Y. Saito, T.A. Bekkeng, K.S. Jacobsen, First in-situ measurements of hf radar echoing targets. Geophys. Res. Lett. **39**(7), l07104 (2012). https://doi.org/10.1029/2012GL051407

J. Moen, K. Oksavik, L. Alfonsi, Y. Daabakk, V. Romano, L. Spogli, Space weather challenges of the polar cap ionosphere. J. Space Weather Space Clim. (2013). https://doi.org/10.1051/swsc/2013025

H.M. Mott-Smith, I. Langmuir, The theory of collectors in gaseous discharges. Phys. Rev. **28**, 727–763 (1926). https://doi.org/10.1103/PhysRev.28.727

J. Muylaert, R. Reinhard, C. Asma, V. Danilkin, Qb50, an international network of 50 cubesats for multi-point, in-situ measurements in the lower thermosphere and re-entry research, in *QB50 Workshop* (2009)

K. Oksavik, J. Moen, M. Lester, T.A. Bekkeng, J.K. Bekkeng, In situ measurements of plasma irregularity growth in the cusp ionosphere. J. Geophys. Res. Space Phys. **117**(A11), a11301 (2012). https://doi.org/10.1029/2012JA017835

P. Prikryl, P.T. Jayachandran, S.C. Mushini, D. Pokhotelov, J.W. MacDougall, E. Donovan, E. Spanswick, J.P. St-Maurice, GPS TEC, scintillation and cycle slips observed at high latitudes during solar minimum. Ann. Geophys. **28**(6), 1307–1316 (2010). https://doi.org/10.5194/angeo-28-1307-2010

Program CPSTC, Cubesat design specification (2015)

A. Spicher, W.J. Miloch, J.I. Moen, Direct evidence of double-slope power spectra in the high-latitude ionospheric plasma. Geophys. Res. Lett. **41**(5), 1406–1412 (2014). https://doi.org/10.1002/2014GL059214

A. Spicher, T. Cameron, E.M. Grono, K.N. Yakymenko, S.C. Buchert, L.B.N. Clausen, D.J. Knudsen, K.A. McWilliams, J.I. Moen, Observation of polar cap patches and calculation of gradient drift instability growth times: a swarm case study. Geophys. Res. Lett. **42**(2), 201–206 (2015a). https://doi.org/10.1002/2014GL062590

A. Spicher, W.J. Miloch, L.B.N. Clausen, J.I. Moen, Plasma turbulence and coherent structures in the polar cap observed by the ICI-2 sounding rocket. J. Geophys. Res. Space Phys. **120**(12), 10959–10978 (2015b). https://doi.org/10.1002/2015JA021634

C. Venturini, L. Abramowitz, J. Johansen, J. Gee, W. Floyd, Cubesat developmental programs-working with the community, in *AIAA SPACE 2009 Conference & Exposition, AIAA-6501* (2009). https://doi.org/10.2514/6.2009-6501